Scattering of massless Dirac fermions in modulated graphene junctions and its effect on electron transport

Partha Sarathi Banerjee

Department of Physics

INDIAN INSTITUTE OF TECHNOLOGY DELHI

February 2026

Scattering of massless Dirac fermions in modulated graphene junctions and its effect on electron transport

by

Partha Sarathi Banerjee
Department of Physics

submitted

in fulfilment of the requirements of the degree of

Doctor of Philosophy

to the

INDIAN INSTITUTE OF TECHNOLOGY DELHI
February 2026

Dedicated to

my parents
and
late grandparents

CERTIFICATE

This is to certify that the thesis entitled "**Scattering of massless Dirac fermions in modulated graphene junctions and its effect on electron transport**" submitted by **Partha Sarathi Banerjee**, for the award of the degree of **Doctor of Philosophy** in **Physics** at **Indian Institute of Technology, Delhi**, is a record of original research carried out by him under our supervision. To the best of our knowledge, the matter embodied in this thesis has not been submitted for the award of any other degree or diploma.

Date: February 13,2026
Place: New Delhi

Prof. Rahul Marathe
(Thesis Supervisor)
Department of Physics
IIT Delhi

Prof. Sankalpa Ghosh
(Thesis Supervisor)
Department of Physics
IIT Delhi

ACKNOWLEDGEMENTS

I would like to express my deepest gratitude to my supervisors, Prof. Rahul Marathe and Prof. Sankalpa Ghosh, for their invaluable guidance, constant encouragement, and insightful discussions throughout the course of this work. Their mentorship has been instrumental in shaping both my research and academic growth.

I sincerely acknowledge the contributions of Prof. Sujeet Chaudhary, Prof. Saswata Bhattacharya, and Prof. Nirat Ray, who served as SRC members. Their critical evaluation and constructive suggestions at various stages of this work have greatly contributed to the development of this thesis.

I am also thankful to the faculty members and staff of the Department of Physics, IIT Delhi, for providing a stimulating and supportive research environment. I gratefully acknowledge my colleagues and friends for their encouragement and companionship, which have made my Ph.D. journey an enriching and enjoyable experience.

I would also like to express my gratitude to my teachers, who have inspired me and guided me along the way. I thank my teacher Subhabrata Bandyopadyay for teaching me to approach problems with the perspective of a physicist. I am also grateful to the teachers who inspired me during my school days, especially Krishnendu Lodh, Sudipta Jhampri, and Banibrata Ghosh. During my college days, I would like to thank Prof. Partha Ghosh for his constant encouragement and support, and I also thank Prof. Rahul Marathe again for his guidance during my Master's at IIT Delhi.

I would like to express my heartfelt gratitude to Dr. Inderpreet Kaur, Dr. Poornima Shakya, Dr. Shahrukh Salim, Dr. Rita Majumdar, Dr. Vipul Upadhyay, Dr. Disha Arora, Dr. Deepanshu Aggarwal, Neha, and Komal, who were my labmates during this journey. Their constant support, cheerful company, and willingness to help made the long hours in the lab not only productive but also truly memorable, and I will always cherish the time we spent together.

Finally, I owe my deepest thanks to my parents and my late grandparents for their unconditional love, patience, and encouragement, without which this work would not have been possible.

New Delhi Partha Sarathi Banerjee

ABSTRACT

Graphene, with its low-energy quasiparticles described by massless Dirac fermions (MDFs), provides an unparalleled platform to study and manipulate quantum transport phenomena. In condensed matter physics, the role of external electrostatic, magnetic, and periodic potentials in controlling quasiparticle dynamics and generating emergent transport regimes has been extensively studied and established as a key paradigm. This thesis investigates three such problems, establishing theoretical connections to optics, superconductivity, and quantum Hall physics, while highlighting pathways toward graphene-based device applications.

In the first part, we studied quasiparticle scattering from two-dimensional quantum dot lattices using the Lippmann–Schwinger approach in the first Born approximation. We showed that the differential scattering cross-section is governed by the Fourier transform of the potential, drawing a precise analogy to Fraunhofer diffraction in optics. Angle-resolved resistivity revealed clear signatures of lattice configuration, defects, and moiré patterns, suggesting that electronic transport can serve as a probe of structural features. Importantly, this constitutes the first demonstration of fractional Fourier transform behavior in a condensed matter system, thereby extending the scope of optical analogies to electronic scattering.

In the second part, we analyzed superconducting transport in graphene Josephson junctions incorporating one-dimensional electrostatic and magnetic barriers. Within the Dirac – Bogoliubov – de Gennes formalism, we found that such barriers act as effective refractive-index media for MDFs, tuning the strength of Andreev reflection and modulating the Josephson current. This establishes condensed matter analogues of reflection and refraction phenomena, while providing a mechanism for external control of dissipationless current flow in graphene-based superconducting devices.

In the final part, we examined graphene-based superconductor–quantum Hall–superconductor junctions under external electrostatic modulation. Employing a transfer-matrix framework, we

demonstrated that barrier-induced intermediate chiral edge states supply new current-carrying channels and strongly influence Josephson transport. The analysis further underscored the role of interface scattering and revealed how periodic modulation introduces additional tunability of conductivity, emphasizing the rich interplay between superconductivity and quantum Hall physics.

Taken together, these studies demonstrate that engineered external potentials offer a versatile means of controlling MDF scattering and superconducting transport in graphene systems. By elucidating optical analogues of electronic scattering,tuning the Josephson current in magnetically modulated josephson junctions and the emergence of intermediate chiral edge states in superconductor-quantum Hall-superconductor junctions with electrostatic barrier, this thesis advances a unified perspective on graphene transport with implications for electronic imaging, superconducting device design, and quantum information technologies.

सार

ग्राफीन, अपने निम्न-ऊर्जा क्वासिपार्टिकल्स के साथ, जिनका वर्णन द्रव्यमानहीन डिराक फर्मिऑन (एमडीएफ) द्वारा किया जाता है, क्वांटम परिवहन परिघटनाओं के अध्ययन और संचालन के लिए एक अद्वितीय मंच प्रदान करता है। संघनित पदार्थ भौतिकी में, क्वासिपार्टिकल गतिकी को नियंत्रित करने और आकस्मिक परिवहन व्यवस्थाओं को उत्पन्न करने में बाह्य स्थिरवैद्युत, चुंबकीय और आवर्ती विभवों की भूमिका का व्यापक अध्ययन किया गया है और इसे एक प्रमुख प्रतिमान के रूप में स्थापित किया गया है।

यह शोध ऐसी तीन समस्याओं की जाँच करता है, प्रकाशिकी, अतिचालकता और क्वांटम हॉल भौतिकी के साथ सैद्धांतिक संबंध स्थापित करते हुए, ग्रैफीन आधारित उपकरण अनुप्रयोगों की ओर मार्ग प्रशस्त करता है।

पहले भाग में, हमने प्रथम बोर्न सन्निकटन में लिपमैन-श्विंगर दृष्टिकोण का उपयोग करते हुए द्वि-आयामी क्वांटम बिंदु जालकों से क्वासिपार्टिकल प्रकीर्णन का अध्ययन किया। हमने दिखाया कि विभेदक प्रकीर्णन अनुप्रस्थ काट विभव के फूरियर रूपांतरण द्वारा नियंत्रित होता है, जो प्रकाशिकी में फ्रौनहोफर विवर्तन के साथ एक सटीक सादृश्य प्रस्तुत करता है। कोण-समाधान प्रतिरोधकता ने जालक विन्यास, दोषों और मोइरे पैटर्न के स्पष्ट संकेत प्रकट किए, जिससे पता चलता है कि इलेक्ट्रॉनिक परिवहन संरचनात्मक विशेषताओं की जाँच के रूप में कार्य कर सकता है। महत्वपूर्ण रूप से, यह संघनित पदार्थ तंत्र में आंशिक फूरियर रूपांतरण व्यवहार का पहला प्रदर्शन है, जिससे प्रकाशिक सादृश्यों का दायरा इलेक्ट्रॉनिक प्रकीर्णन तक विस्तृत हो जाता है।

दूसरे भाग में, हमने एक आयामी स्थिरवैद्युत और चुंबकीय अवरोधों को समाहित करते हुए ग्राफीन जोसेफसन जंक्शनों में अतिचालक परिवहन का विश्लेषण किया। डिराक-बोगोलिउबोव-डी गेनेस औपचारिकता के अंतर्गत, हमने पाया कि ऐसे अवरोध एमडीएफ के लिए प्रभावी अपवर्तनांक माध्यम के रूप में कार्य करते हैं, एंड्रीव परावर्तन की प्रबलता को समायोजित करते हैं और जोसेफसन धारा को संशोधित करते हैं। यह परावर्तन और अपवर्तन परिघटनाओं के संघनित पदार्थ अनुरूपों को स्थापित करता है, साथ ही ग्राफीन-आधारित अतिचालक उपकरणों में अपव्यय रहित धारा प्रवाह के बाह्य नियंत्रण के लिए एक तंत्र प्रदान करता है।

अंतिम भाग में, हमने बाह्य स्थिरवैद्युत मॉडुलन के अंतर्गत ग्राफीन-आधारित अतिचालक-क्वांटम हॉल-अतिचालक संधियों का परीक्षण किया। स्थानांतरण-मैट्रिक्स ढाँचे का उपयोग करते हुए, हमने प्रदर्शित किया कि अवरोध-प्रेरित मध्यवर्ती किरल किनारा अवस्थाएँ नए धारा-वाहक चैनल प्रदान करती हैं और जोसेफसन परिवहन को दृढ़ता से प्रभावित करती हैं। विश्लेषण ने इंटरफ़ेस प्रकीर्णन की भूमिका को

और रेखांकित किया और बताया कि कैसे आवर्ती मॉडुलन चालकता की अतिरिक्त ट्यूनेबिलिटी प्रस्तुत करता है, जो अतिचालकता और क्वांटम हॉल भौतिकी के बीच समृद्ध अंतर्संबंध पर बल देता है।

कुल मिलाकर, ये अध्ययन प्रदर्शित करते हैं कि अभियांत्रित बाह्य विभव ग्राफीन प्रणालियों में एमडीएफ प्रकीर्णन और अतिचालक परिवहन को नियंत्रित करने का एक बहुमुखी साधन प्रदान करते हैं। इलेक्ट्रॉनिक प्रकीर्णन के प्रकाशिक अनुरूपों को स्पष्ट करके, चुंबकीय रूप से मॉडुलित जोसेफसन संधियों में जोसेफसन धारा को ट्यून करके और स्थिरवैद्युत अवरोध वाले अतिचालक-क्वांटम हॉल-अतिचालक संधियों में मध्यवर्ती किरल किनारा अवस्थाओं के उद्भव द्वारा, यह शोध प्रबंध ग्राफीन परिवहन पर एक एकीकृत दृष्टिकोण प्रस्तुत करता है जिसके इलेक्ट्रॉनिक इमेजिंग, अतिचालक उपकरण डिज़ाइन और क्वांटम सूचना प्रौद्योगिकियों पर प्रभाव पड़ता है।

TABLE OF CONTENTS

LIST OF FIGURES

LIST OF TABLES

CHAPTER 1

Introduction

1.1 Introduction

The propagation of electron beams can be manupulated using electrostatic and magnetic field[1–6] which works similarly as lenses do in the optical systems. This concept makes it possible to create electrical systems inspired by components of geometrical optics, such as, lenses, mirrors, splitters, prisms etc [4, 7–9]. In optics, transparent interfaces between materials are used to manipulate light beams, such as lenses or prisms. For the case of ballistic electron beams in graphene such is done by creating an interface of two regions with difference in carrier density achieved by using electrical gates [10–12] or doping [13]. This is called a p-n junction in literature. The possibility of manipulating the electron beams in graphene using p-n junctions has led to various milestones in nanoelectronics, such as, Veselago lenses [3, 4, 14], Dirac Fermion microscope [2], electron beam collimation [1, 7], different types of interferometers [15–18], gate tunable beam-splitter of massless Dirac fermions (MDF) [6], Fabry-Pérot resonator in graphene/hBN moiré superlattice [19]. This connection to optics shows graphene's role as a versatile platform for exploring wave phenomena in quantum transport, making graphene an ideal system for bridging the fields of condensed matter physics and quantum optics. Extending this optical analogy, recent studies have explored the scattering of MDFs in graphene using various types of electromagnetic potentials. Most studies have focused on potentials that are constant along one direction [4, 7, 11, 20–22]. New possibilities emerge when the scattering potential varies in two transverse directions. For example, in the well-known Fraunhofer diffraction, when the observation point is significantly distant(z) from the diffracting object dubbed in the literature as the far-field case, the field distribution at the observation plane is the Fourier transform of the aperture function ($A(x', y')$) [23–28]. The diffracting object is positioned at the front focal plane of a lens, resulting in the generation of a Fourier transform of the object at the back focal plane of the lens, thereby satisfying the conditions for the Fraunhofer approximation ($z >> [x'^2 + y'^2]_{\max} / \lambda$).

Another intriguing manifestation of graphene's unique electronic properties is its integration with superconducting systems to form Josephson junctions (JJs). In a graphene-superconductor-graphene (SGS) junction, proximity-induced superconductivity allows for dissipation-less supercurrents, i.e., Josephson currents (JC) [29, 30]. Such devices played a significant role in quantum technologies such as superconducting qubit devices [31–34], sensing small magnetic fields [35, 36], parametric amplifiers [37, 38], single photon detection [39] etc. In mono and bi-layer graphene, the superconducting part is made by putting a superconducting electrode on top of graphene sheet and making use of proximity effect [30, 40, 41]. If two such closely spaced superconducting electrodes are placed on top a graphene sheet, SGS [29, 42, 43] junction is formed. Interface of graphene and superconductor, due to unique property of graphene, gives another interesting difference compared to other conventional materials like two-dimensional electron gas(2DEG), metal etc. While, in other materials there is only one type of *Andreev reflection*, the electron-hole conversion process, dubbed as *retro Andreev reflection*(RAR). In RAR, the reflected hole (electron) traces back the path of incident electron (hole). In graphene, we see another type of Andreev reflection, called *specular Andreev reflection*(SAR).

Motivated by these, in this thesis we present three different case studies of scattering of massless Dirac fermions in graphene in three graphene based structures. Through studying the electron transport we try to analyze the effect of different types of scatterers in three different systems. In the first problem, addressed in the third chapter of this thesis, by using the similarity of scattering of massless Dirac fermions in graphene and Fraunhofer diffraction in optical systems, we study the properties of a electrostatic potential which acts as a scatterer for plane wave of MDFs in graphene by analyzing the dc-resistivity [44]. In the second problem, addressed in the fourth chapter of this thesis, we consider a series of one dimensional electrostatic scalar potential and magnetic vector potential barriers in graphene sandwiched by proximity induced superconducting regions on both sides. We study the effect of these barriers on the Josephson current [45]. In the third problem, addressed in the fifth chapter of this thesis, our aim is to study the effect of electrostatic barriers in the *Andreev reflection* process in strong magnetic fields. In this case we analyze the Josephson conductivity to study the effect of such barriers. We started with non-relativistic two-dimensional superconductor- quantum Hall-superconductor (SQHS) junctions and showed the effect of such barriers as the presence of intermediate chiral edge states (ICES). These ICES show significant modification to the Josephson conductivity. We have also extended our analysis to the graphene based SQHS junctions.

To elaborate, in the first problem, we show that the electronic analogue of the Fraunhofer diffraction in optical systems can be realized in a fully two-dimensional (2D) scattering model, where the scattering of such MDF takes place from a two-dimensional superlattice potential that can be realized by creating an electrostatically defined array of quantum dots (QDs) on the surface of single-layer graphene [46–55]. Using the first Born approximation, we show that the differential scattering cross-section (DSC) of such potentials is proportional to the Fourier transform of the potential profile, analogous to the intensity pattern in the back focal plane in optical Fraunhofer diffraction [27]. However, due to Klein tunnelling and absence of back-scattering, the scattered MDFs are mainly transmitted towards the forward direction only. This is an uniqueness of graphene and studying scattering of graphene electrons interesting. Furthermore, the cardioid-like differential scattering cross-section pattern observed for Gaussian QDs reflects the combined effects of Mie scattering [14] and Klein tunneling [56–58], highlighting graphene's unique scattering properties. We demonstrate that studying the transport of graphene electrons through an experimentally measurable dc-resistivity, which is dependent upon this DSC, enables the detection of properties of the scattering potential, including symmetry, lattice configuration, lattice constant, and the size and location of defects in the scattering potential. However, there is an interesting difference between our case and the optical case. While in optical image processing a second lens is used to reconstruct the image, similar thing is however not possible in our system. To overcome this limitation we have introduced another degree of freedom, rotation angle ϕ which is the angle between the direction of propagation of incident plane wave and the symmetry axis of the two dimensional QD lattice (TDQDL). We show our approach and the analogous optical image processing in FIG. 1.1 We show that by doing Fourier analysis of dc-resistivity in such systems we can extract the properties of the external, extending graphene's applicability to electronic image processing and pattern recognition.

In the second problem, addressed in the fourth chapter of this thesis, we consider both electrostatic and magnetic barriers in graphene sandwiched between two superconducting regions. In this case, to understand the signature of the barriers we study experimentally measurable temperature dependent Josephson current. In our proposed model [45], the magnetic barriers that we are considering are created by highly localized magnetic fields [59–63] by putting a ferromagnetic stripe on top of the surface of the graphene region [64, 65]. In experiments, such metallic stripes have been made by NdFeB [64], Co [65]. They generate a strong mag-

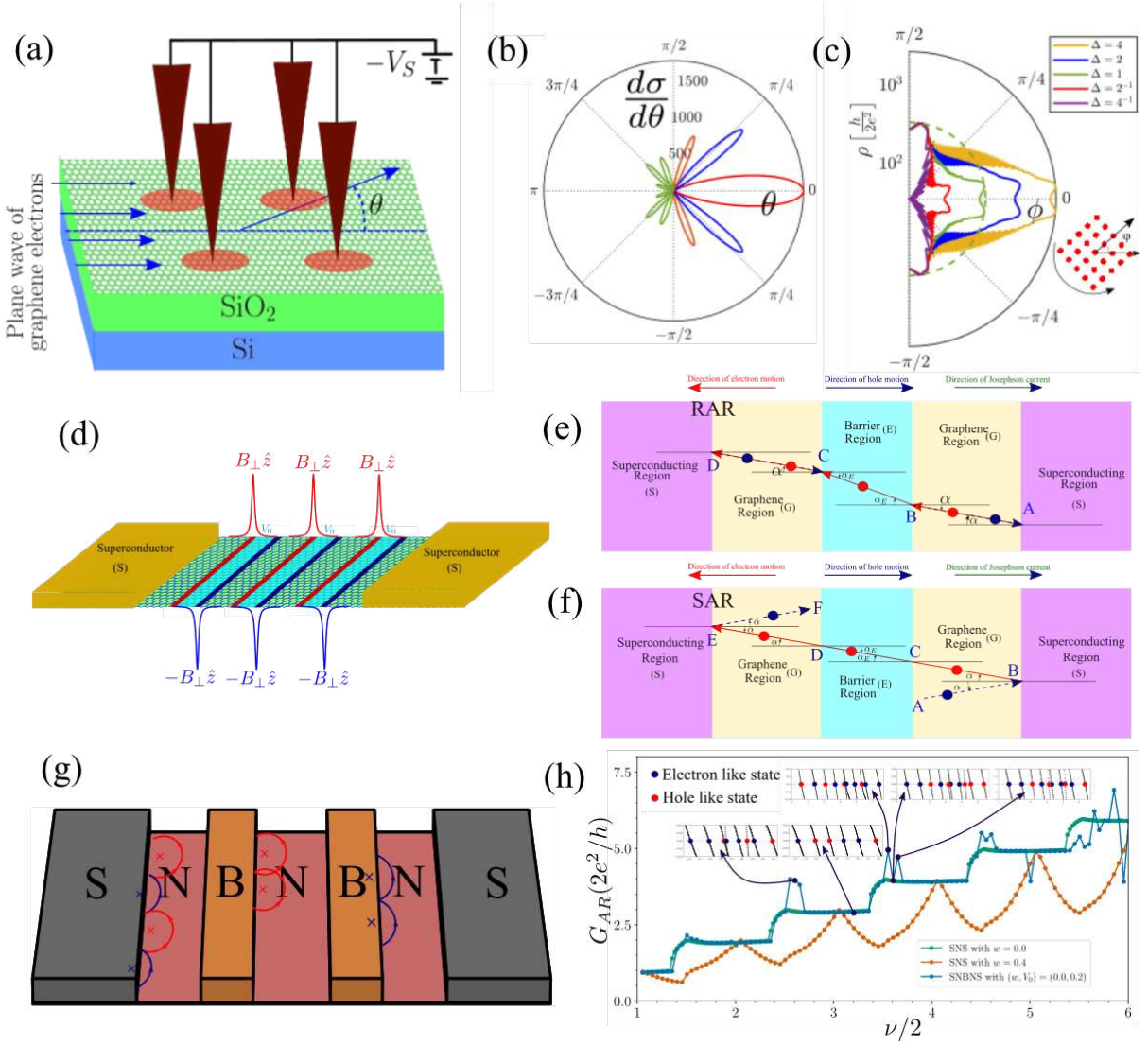

FIG. 1.1: (a) The schematic diagram of a plane wave (direction shown in blue arrows) of MDFs in ballistic graphene, getting scattered by a two-dimensional array of Gaussian quantum dot(QD) potentials. (b) The polar plot of the DSC for a square lattice of QDs. In (c) the angle-resolved dc-resistivity of the system parallel to the direction of propagation of the incoming plane wave of graphene electrons is plotted under this scattering potential rotated at an arbitrary angle. In (d) the schematic depiction of the SGS type JJ with periodic electric and magnetic field in the graphene region is shown. In (e) and (f) we show the propagation of electron and hole for our SGS system where only one barrier is present in RAR and SAR domains respectively. The blue solid circle denotes a hole and an electron is represented by a red solid circle. In (g) we show the schematic diagram of the system we are considering. The red and blue semicircles denote the classical electron and hole orbits. In (h) we show the conductivity of this system, In the inset we provide the intermediate chiral edge states which contribute to the fluctuation in conductivity. Figure (a)-(c) is taken from our published work [44], Figure (d)-(f) is taken from our published work [45].

netic field to create this highly inhomogeneous magnetic field, which explicitly breaks the time reversal symmetry in the graphene region. By employing these stripes, a magnetic vector potential barrier can be created, wherein two such stripes generate strong magnetic fields of similar magnitude but in opposing directions [66], oriented transversely to the plane of the graphene layer. Using a fully scalable photo-lithographic process, Co based ferromagnetic layer has been deposited in graphene based system to make this type of magnetic tunnel junction [67–69]. The electrostatic barriers that we are considering can be created by putting a gate voltage and creating p-n junction in graphene [7, 11, 20, 70–72]. The schematic diagram of the system is shown in FIG. 1.1 (d). We are considering array of these barriers, which can be viewed as a realization of magnetic Kronig-Penny model [62, 73, 74], and their combined effect on the Andreev reflection by studying the Josephson current. Using the Dirac-Bogoloubov-de-Gennes(DBdG) theory we have shown such barriers in the graphene region between two superconducting regions act as a medium of different refractive index as compared to the barrier free region. This electronic analogue of refractive index can be tuned by changing the strength of both electrostatic and magnetic barriers we are considering. By tuning these barriers, the dynamics electrons and holes can be influenced which undergo *Andreev reflection* in two superconductor-graphene interfaces on both sides of graphene regions. We have shown that this gives us another additional control over the Josephson current. The schematic diagram for the propagation of electrons and holes in the system in RAR and SAR regimes is shown in FIG. 1.1 (e) and (f) respectively.

In the third problem, discussed in the fifth chapter of this thesis, we study electron transport in local potential barrier modulated superconductor-quantum Hall-superconductor (SQHS) Josephson junctions. The system is similar to a S-2DEG-S type Josephson junction where the 2DEG is exposed to an uniform magnetic field and a series of electrostatic barriers. The uniform magnetic field[75] creates quantized Landau level states[76]. We use the transfer matrix method to show that the local potentials in the quantum Hall regime can induce current carrying intermediate chiral edge states(ICES) at electrostatic boundaries [77, 78] which impact and alter the Josephson conductivity through such junctions. First, we used the BTK framework [79] to calculate the transfer matrices. Using these transfer matrices, we calculated the dispersion to identify the intermediate chiral edge states(ICES) that appear due to the presence of locally induces electrostatic barriers. Then using the Landauer-Buttiker formula, we calculate the conductivity in the ballistic regime in such junctions and study the effect of barrier potentials through the current carrying ICES. We have further extended our study to a periodically

modulated SQHS JJ where a periodic potential is applied to the 2DEG regions along with the transverse magnetic field.

We shall now provide some basic concepts which will be useful to understand the problems addressed in the thesis and chapter-wise organization of the thesis.

1.2 Summary of the Problems Addressed

This thesis studies three scattering problems in graphene and shows its effect on the transport of massless Dirac fermions(MDF) in graphene. For the first case, we theoretically study the scattering of MDFs from a two-dimensional array of barrier potentials also called two-dimensional quantum dot lattice(TDQDL) created by electric gates. We calculate the differential scattering cross-section using the first Born approximation and Lippmann–Schwinger formalism. We show that the dc-resistivity depends on the rotation angle of the scattering lattice and use this to build and electronic analogue of Fourier optics. In the second case, we study electron transport in graphene in presence of one dimensional electric and magnetic barrier potentials in the middle of two proximity induced superconducting regions. We show that the Josephson current in this case can be modulated as a function of the strength of magnetic barrier and gate potentials. In the third case, we developed a transfer matrix based theoretical framework to study the transport in local potential barriers modulated superconductor-quantum Hall-superconductor (SQHS) Josephson junctions (JJ). We demonstrate the presence of intermediate chiral edge states(ICES) induced by the local potential barriers and calculate its effect on Josephson conductivity in the ballistic regime using the Bogoliubov-de-Gennes (BDG) theory and Büttiker description. This method can be further extended to graphene based SQHS JJs. To summarize,

- We have quantitatively shown the effect of lattice configuration, symmetry, lattice constant, size and location of a defect in a TDQDL when it acts as a scattering potential using the dc-resistivity. We have further extended study to show the electronic analogue of Babinet's principle.
- In case of an SGS junction, we have shown that the Josephson current can be significantly tuned by putting a series of gate defined electrostatic scalar potential and magnetic vector potential barrier and changing their strength.
- We show the effect of intermediate chiral edge states induced by the presence of local electrostatic potential barriers in superconductor- quantum Hall-superconductor JJs on the Josephson conductivity.

1.3 Organization of Thesis

We have divided this thesis into six chapters. The following sections provide a summary of the following five chapters.

In the **Chapter 2** of this thesis we discuss various theoretical methods used to study the systems that will be used in the subsequent chapters of this thesis. We start with the quantum theory of scattering using the Lippmann–Schwinger formalism. We calculate the scattering amplitude for massless Dirac fermions (MDF). Next, we define the transition operator and calculate the differential scattering cross-section for a given potential. These are key concepts that will be highly useful in understanding the third chapter of the thesis. Next, we study the scattering of massless Dirac fermions using partial wave analysis. With the help of that we then derive the optical theorem.

Next to understand the methodology of fourth chapter of this thesis, we have given a brief introduction to the Blonder Tinkham Klapwijk(BTK) formalism and Bogoliubov–de Gennes (BdG) equations. As we are studying the transport in graphene based junctions in the fourth chapter, here we show how the BdG equation is changed for the case of MDFs in graphene. We also discuss the Andreev reflection which is the electron hole conversion process which happens in superconducting junctions.

Later part of this chapter contains the key concepts to understand the third problem addressed in this thesis discussed in the fifth chapter. Here using the BTK formalism we show how the BdG equation is transformed in the presence of a uniform magnetic field. Next, we derive the dispersion and the calculation of small bias conductance for superconductor-2DEG junctions in presence of magnetic field. We also show how this method can be extended to graphene based junctions.

Chapter 3 is based on work reported in [44]. The similarity of movement of electrons or charged particles subjected to electric and magnetic fields and propagation of electromagnetic fields in dielectric medium with varied refractive index is well studied in the field of electron optics. By studying the scattering of MDFs, which are charge carriers in graphene, we show an analogue of Fourier Optics in an electronic system. We use Lippmann–Schwinger formalism in the first Born approximation to show that the obtained differential scattering cross-section is proportional to the Fourier transform of the scattering potential. This is analogous to intensity

in the back focal plane in case of the Fraunhofer diffraction pattern [23, 27]. In the field of optical image processing a second lens is used to create the Fourier transform of the diffraction pattern to reconstruct the image [25, 26]. But this is not possible in electron scattering. To overcome this we have introduced another degree of freedom, rotation angle between the direction of propagation of incident plane wave and the symmetry axis of the two-dimensional QD lattice (TDQDL) and calculate the angle resolved dc-resistivity. We consider three prototypes of TDQDL for our study (i) TDQDL with square and hexagonal lattice structure, (ii) square and hexagonal TDQDL with defect region of different shapes and different locations and (iii) moiré pattern of two square or hexagonal TDQDL. Doing Fourier analysis of the angle resolved dc-resistivity of these structures we show that the spatial frequency associated with the dc-resistivity gets filtered according to the structural changes in the TDQDL.

We discuss about work reported in [45] in **Chapter 4**. In this chapter we show the transport of MDFs in graphene in presence of one dimensional electric and magnetic barrier potentials between two proximity induced superconducting regions. The electric barriers can be created by electrostatic gate potentials in an experimental system. The magnetic barrier that we discuss come from highly localized non-uniform magnetic field. These magnetic barriers are very similar to magnetic tunnel junctions which are made with graphene by exposing the graphene layer to localized pattern of strong magnetic field created by Ferromagnetic materials [67, 68, 80]. The graphene region with electrostatic and magnetic barriers work as the weak link between two proximity induces superconducting regions. We examine how the dissipation-less supercurrent, namely the Josephson current [81, 82], that flows between two superconductors connected by a weak link can be tuned by controlling properties of these barriers. Using the Dirac-Bogoliubov-de-Gennes (DBDG) theory [29, 83–86], we show that the dispersion of the MDFs get significantly altered due to the presence of these barriers in the graphene region. In the retro Andreev reflection regime, we have shown that these barrier regions act as mediums with modulated refrative index, which in an experimental system can be controlled by changing the strength of both the electrostatic and magnetic barrier. These leads to significant modulation of the Josephson current. In this chapter we show the numerically evaluated Josephson current and its dependence on the strength of the magnetic barrier and the gate voltage and discuss the practical applications of such controlling of Josephson currents.

In the **Chapter 5** of this thesis, we study the Andreev reflection in superconductor-quantum Hall-superconductor(SQHS) junctions in presence of local barrier potentials. In presence of

an uniform magnetic field, we observe the cyclotron motion of the quasi-particles [75, 87]. We develoved a transfer matrix based theoretical framework to study the effect of electrostatic barriers in the N region on the Josephson current. Using the Bogoliubov-de-Gennes (BDG) theory [84] we calculated the dispersions of SQHS JJs in presence of potential barriers. The presence of potential barriers give intermediate current carrying edge states. We have also explored the case of an non-ideal interface where a scattering potential is present at the interface between superconductor and 2DES interface. Then, using the Büttiker description [88], we calculate the conductivity and show the effect of these current carrying edge states. We have also extended our formalism to a periodically modulated SQHS JJ where a periodic potential is applied to the N regions along with the transverse magnetic field.

Chapter 6 summarizes the important results which we obtained in this thesis and discussed the applications or future scope of research in this topic.

CHAPTER 2

Theoretical Background

In this chapter, we discuss the theoretical background necessary to understand the next chapters of this thesis where we discuss the results obtained from the three research problems we addressed in this thesis.

We begin by discussing the quantum theory of scattering of massless Dirac fermions(MDF) using the Lippmann-Schwinger formalism in Sec. 2.1 which is key component of our first problem discussed in next chapter. We derive the Green's function in graphene using the non-relativistic Green's function of Helmholtz's equation. Then in Sec. 2.2 we derive the differential scattering cross-section for a given scattering potential using the transition operator and Born approximation. Next, we provide the partial wave analysis and show the phase shift due to the presence of a scattering potential in Sec. 2.3. We further derive the optical theorem in Sec. 2.4. We use these concepts extensively in the first problem discussed in the third chapter of this thesis.

As we discuss the graphene based superconducting junctions in the second problem discussed in the fourth chapter of this thesis, here we start by showing the BTK formalism and BDG equation in Sec. 2.5. In graphene based system we show how the BDG equation is changed in Sec. 2.6. We derive the wavefunctions in graphene and superconductor regions. We also discuss the Andreev reflection and two types of Andreev reflection in graphene.

In the third problem, discussed in the fifth chapter of this thesis, we discuss the superconducting junctions in presence of uniform magnetic field. The junction of quantum Hall systems and superconductor has been studied extensively in two dimensional electron systems in [75] and graphene systems in [86]. In the third problem addressed in this thesis, we study the effect of electrostatic barriers in the quantum Hall systems in graphene quantum Hall junctions. To understand that, in Sec. 2.7, we show the BdG equation in presence of uniform magnetic field. We discuss the breaking of time reversal symmetry for the vector potential in 2DEG system which will be used in fourth chapter and breaking of time reversal symmetry for the vector potential in graphene which will be used in fifth chapter.

2.1 Quantum Theory of Scattering of MDFs

The Lippmann-Schwinger equation [89, 90] is used to calculate the wavefunction in the presence of a scattering potential using the wave-functions of the free Hamiltonian ($\mathbf{H}_0$). The Schrödinger equation in presence of a scattering potential is

$$\left(\hat{\mathbf{H}}_0 + \hat{V}\right)|\Psi_{\mathbf{k}}\rangle = E\,|\Psi_{\mathbf{k}}\rangle \tag{2.1}$$

and the free wavefunctions are solutions of the free Schrödinger equation $\hat{\mathbf{H}}_0\,|\phi_{\mathbf{k}}\rangle = E\,|\phi_{\mathbf{k}}\rangle$. The free particle hamiltonian is given by $\mathbf{H}_0 = v_F\sigma\cdot\mathbf{p} = -i\hbar v_F\sigma\cdot\boldsymbol{\nabla}$ and the free particle wavefunctions are given by

$$\phi^e_{\mathbf{k}}(\vec{r}) = \begin{bmatrix} 1 \\ e^{i\theta_{\mathbf{k}}} \end{bmatrix} e^{i\mathbf{k}\cdot\mathbf{r}} \tag{2.2}$$

for electrons and

$$\phi^h_{\mathbf{k}}(\vec{r}) = \begin{bmatrix} 1 \\ -e^{i\theta_{\mathbf{k}}} \end{bmatrix} e^{i\mathbf{k}\cdot\mathbf{r}} \tag{2.3}$$

for holes with eigenvalues $E = \pm\hbar v_F k$ respectively. Here $\mathbf{k}$ is the wave vector. The desired solution for the scattered wavefunction satisfies Eq. (2.1). It is given by

$$|\Psi^{\eta}_{\mathbf{k}}\rangle = |\phi_{\mathbf{k}}\rangle^{\eta} + \frac{1}{[EI_2 - \hat{\mathbf{H}}_0]}\hat{V}\,|\Psi^{\eta}_{\mathbf{k}}\rangle \tag{2.4}$$

Here, $\eta = e, h$ denotes electron and hole wavefunctions. To calculate the wavefunctions, we make the eigenvalue slightly complex $(E \pm i\epsilon)$ and take the limit where the imaginary part is $\epsilon \to 0$.

This gives us,

$$\left|\Psi^{\eta,\pm}_{\mathbf{k}}\right\rangle = |\phi_{\mathbf{k}}\rangle + \hat{G^{\pm}_0}\hat{V}\left|\Psi^{\eta,\pm}_{\mathbf{k}}\right\rangle \tag{2.5}$$

where,

$$\hat{G^{\pm}_0} = \lim_{\epsilon\to 0}\left[EI_2 - \hat{\mathbf{H}}_0 \pm i\epsilon\right]^{-1}. \tag{2.6}$$

Eq. (2.5) is called the **Lippmann-Schwinger equation** [89, 90], $\hat{G_0^{\pm}}$ is called the Green's function and the plus sign corresponds to the physically relevant outgoing scattered wave and the negative sign corresponds to an incoming wave in asymptomatic region. In position representation eq. (2.5) becomes,

$$\Psi_{\mathbf{k}}^{\eta,\pm}(\mathbf{r}) = \phi_{\mathbf{k}}^{\eta}(\mathbf{r}) + \int d^2\mathbf{r}' G_0^{\pm}(\mathbf{r},\mathbf{r}',E) V(\mathbf{r}') \Psi_{\mathbf{k}}^{\eta,\pm}(\mathbf{r}') \tag{2.7}$$

The Green's function $G_0(\mathbf{r},\mathbf{r}',E)$ of this equation satisfies the matrix equation,

$$\left[EI_2 - \mathbf{H}_0(\mathbf{r})\right] G_0(\mathbf{r},\mathbf{r}',E) = \delta(\mathbf{r}-\mathbf{r}') \tag{2.8}$$

The Green's function is calculated from the Green's function of the Helmholtz's equation in 2-dimension [91]. Using $\mathbf{H}_0 = v_F \sigma \cdot \mathbf{p} = -i\hbar v_F \sigma \cdot \boldsymbol{\nabla}$ can write,

$$\frac{1}{\hbar^2 v_F^2}\left[EI_2 - \mathbf{H}_0(\mathbf{r})\right]\left[EI_2 + \mathbf{H}_0(\mathbf{r})\right] = \left(k^2 + \nabla^2\right) I_2 \tag{2.9}$$

We know the Green's function of the two dimensional Helmholtz's equation as,

$$G_H^{+} = \left(-\frac{i}{4}\right) H_0^{(1)}\left(k|\mathbf{r}-\mathbf{r}'|\right)$$
$$G_H^{-} = \left(-\frac{i}{4}\right) H_0^{(2)}\left(k|\mathbf{r}-\mathbf{r}'|\right)$$

Here, $H_\alpha^{(1)}(z)$ and $H_\alpha^{(2)}(z)$ are Hankel functions of first and second kind of order α. Using these we can write,

$$(k^2 + \nabla^2) I_2 G_H^{\pm}(\vec{r},\vec{r'},E) = \delta(\mathbf{r}-\mathbf{r}') I_2 \tag{2.10}$$

Using Eq. (2.8), (2.9) and (2.10)

$$G_0^{+}(\mathbf{r},\mathbf{r}',E) = \frac{1}{\hbar^2 v_F^2}\left(-\frac{i}{4}\right)\left[EI_2 - i\hbar v_F \sigma \cdot \boldsymbol{\nabla}\right] H_0^{(1)}\left(k|\mathbf{r}-\mathbf{r}'|\right) \tag{2.11}$$
$$G_0^{-}(\mathbf{r},\mathbf{r}',E) = \frac{1}{\hbar^2 v_F^2}\left(-\frac{i}{4}\right)\left[EI_2 - i\hbar v_F \sigma \cdot \boldsymbol{\nabla}\right] H_0^{(2)}\left(k|\mathbf{r}-\mathbf{r}'|\right)$$

If we consider only the physically relevant outgoing scattered wave then,

$$\Psi_{\mathbf{k}}^{\eta,+}(\mathbf{r}) = \phi_{\mathbf{k}}^{\eta}(\mathbf{r}) + \int d^2\mathbf{r}' G_0^{+}(\mathbf{r},\mathbf{r}',E) V(\mathbf{r}') \Psi_{\mathbf{k}}^{\eta,+}(\mathbf{r}') \tag{2.12}$$

Again, if we define an angle θ as, $\theta = \tan^{-1}\left(\frac{y-y'}{x-x'}\right)$ then, using the property [92] of Hankel Function $\partial_x H_0^{(1)}(x) + H_1^{(1)}(x) = 0$ we can write,

$$\sigma \cdot \boldsymbol{\nabla} H_o^{(1)}\left(k|\mathbf{r}-\mathbf{r}'|\right) = -\begin{bmatrix} 0 & e^{-i\theta} \\ e^{i\theta} & 0 \end{bmatrix} k H_1^{(1)}\left(k|\mathbf{r}-\mathbf{r}'|\right) = -\sigma_\theta k H_1^{(1)}\left(k|\mathbf{r}-\mathbf{r}'|\right) \tag{2.13}$$

Here, $\sigma_\theta = \begin{bmatrix} 0 & e^{-i\theta} \\ e^{i\theta} & 0 \end{bmatrix}$

Again, in large distance limit $|\mathbf{r}-\mathbf{r}'| \to$ large,

$$H_0^{(1)}\left(k|\mathbf{r}-\mathbf{r}'|\right) = \sqrt{\frac{2}{\pi k|\mathbf{r}-\mathbf{r}'|}} e^{i\left(k|\mathbf{r}-\mathbf{r}'|-\frac{\pi}{4}\right)} = \sqrt{\frac{2}{i\pi k|\mathbf{r}-\mathbf{r}'|}} e^{i(k|\mathbf{r}-\mathbf{r}'|)} \tag{2.14a}$$

$$H_1^{(1)}\left(k|\mathbf{r}-\mathbf{r}'|\right) = \sqrt{\frac{2}{\pi k|\mathbf{r}-\mathbf{r}'|}} e^{i\left(k|\mathbf{r}-\mathbf{r}'|-\frac{\pi}{2}-\frac{\pi}{4}\right)} = (-i)\sqrt{\frac{2}{i\pi k|\mathbf{r}-\mathbf{r}'|}} e^{i(k|\mathbf{r}-\mathbf{r}'|)} \tag{2.14b}$$

Again, if α is the angle between $\boldsymbol{r}$ and $\boldsymbol{r'}$

$$\begin{aligned} |\boldsymbol{r}-\boldsymbol{r'}| &= \sqrt{r^2 - 2rr'\cos\alpha + r'^2} \\ &= r\left(1 - \frac{2r'}{r}\cos\alpha + \frac{r'^2}{r^2}\right)^{1/2} \\ &\approx r - \hat{\boldsymbol{r}}\cdot\boldsymbol{r'} \text{ as } r \gg r' \end{aligned} \tag{2.15}$$

For the denominator it is sufficient to take $1/|\boldsymbol{r}-\boldsymbol{r'}| = 1/r$. If we take $\eta = e$, then, $E = \hbar v_F k$ and using Eq. (2.11), (2.13), (2.14) and (2.15) the Green's function can be written as [93],

$$G_0^+(\mathbf{r},\mathbf{r}',E) = -\frac{1}{\hbar v_F}\sqrt{\frac{ik}{8\pi r}} e^{ikr} e^{-i\mathbf{k}'\cdot\mathbf{r}'} \begin{bmatrix} 1 & e^{-i\theta} \\ e^{i\theta} & 1 \end{bmatrix} \tag{2.16}$$

Similarly, if we choose $\eta = h$, then, $E = -\hbar v_F k$, the Green's function becomes [93],

$$G_0^+(\mathbf{r},\mathbf{r}',E) = \frac{1}{\hbar v_F}\sqrt{\frac{ik}{8\pi r}} e^{ikr} e^{-i\mathbf{k}'\cdot\mathbf{r}'} \begin{bmatrix} 1 & -e^{-i\theta} \\ -e^{i\theta} & 1 \end{bmatrix}. \tag{2.17}$$

Now the asymptotic scattered wave-function can be written as [93],

$$\Psi_{\mathbf{k}}^{e,+}(\mathbf{r}) = \phi_{\vec{k}}^{e}(\vec{r}) + \frac{1}{\sqrt{2}}\begin{bmatrix}1\\ e^{i\theta}\end{bmatrix}\frac{e^{ikr}}{\sqrt{r}} f_{e-e}(\theta) \tag{2.18}$$

Here,

$$f_{e-e}(\theta) = -\frac{1}{\hbar v_F}\sqrt{\frac{ik}{2\pi}}\int d^2\vec{r'}\frac{1}{\sqrt{2}}\begin{bmatrix}1 & e^{-i\theta}\end{bmatrix} e^{-i\mathbf{k'}\cdot\mathbf{r'}} V(\mathbf{r'})\,\Psi_{\mathbf{k}}^{e,+}(\mathbf{r'}) \tag{2.19}$$

2.2 Transition operator and Differential Scattering Cross Section

The Lippmann-Schwinger equation from Eq. (2.5) can be written as n infinite series as the scattered wavefunction is present in both LHS and RHS of Eq. (2.5). To calculate the wavefunction upto a given order we have use the transition operator [90]. The transition operator is defined as,

$$\hat{V}\left|\Psi_{\mathbf{k}}^{\eta,\pm}\right\rangle = \hat{T}\left|\phi_{\mathbf{k}}\right\rangle. \tag{2.20}$$

Using this definition and Eq. (2.5) we can write,

$$\hat{T} = \hat{V} + \hat{V}\hat{G_0^{\pm}}\hat{V} + \hat{V}\hat{G_0^{\pm}}\hat{V}\hat{G_0^{\pm}}\hat{V} + \ldots \tag{2.21}$$

Now, using this definition, we can write the scattering amplitude as,

$$f_{e-e}(\theta) = -\frac{1}{\hbar v_F}\sqrt{\frac{ik}{2\pi}}\left\langle\phi_{\mathbf{k'}}^{e}\middle|\hat{T}\middle|\phi_{\mathbf{k}}^{e}\right\rangle \tag{2.22}$$

and for the hole part this equation becomes,

$$\Psi_{\mathbf{k}}^{h,+}(\mathbf{r}) = \phi_{\vec{k}}^{h}(\vec{r}) + \frac{1}{\sqrt{2}}\begin{bmatrix}1\\ -e^{i\theta}\end{bmatrix}\frac{e^{ikr}}{\sqrt{r}} f_{h-h}(\theta) \tag{2.23}$$

Where,

$$f_{h-h}(\theta) = \frac{1}{\hbar v_F}\sqrt{\frac{ik}{2\pi}}\left\langle\phi_{\mathbf{k'}}^{h}\middle|\hat{T}\middle|\phi_{\mathbf{k}}^{h}\right\rangle \tag{2.24}$$

For the first order Born approximation we truncate the infinite series at the first term as $\hat{T} = \hat{V}$. The differential scattering cross section from this scattering amplitude is calculated as $\frac{\mathrm{d}\sigma}{\mathrm{d}\theta} = |f(\theta)|^2$. Near Dirac point, $f_{h-h}(\theta) \to 0$ and $f_{e-e}(\theta) \to 0$.

2.3 Partial Wave-Analysis of Massless Dirac Fermions

From the scattering theory the asymptotic wave-function of a particle in presence of a scattering potential is the sum of an incident wave and a spherical wave (in 3 dimensions[94]) or a cirular wave (in 2 dimensions[95, 96]) with a scattering amplitude $f(\theta)$. If a plain wave (with hamiltonian $\mathbf{H}_0 = -\frac{\hbar^2}{2m}\boldsymbol{\nabla}^2$) is scattered by a scattering potential, then the scattered wave-function as large distance can be written as[95, 96]

$$\psi(\mathbf{r}) \approx e^{i\mathbf{k_i}\cdot\mathbf{r}} + \frac{e^{ikr}}{\sqrt{r}} f(\theta) \quad \text{[in 2-d]} \tag{2.25}$$

$$\psi(\mathbf{r}) \approx e^{i\mathbf{k_i}\cdot\mathbf{r}} + \frac{e^{ikr}}{r} f(\theta) \quad \text{[in 3-d]} \tag{2.26}$$

For a relativistic free particle ($\mathbf{H}_0 = \beta mc^2 + c\alpha \cdot \mathbf{p}$) the asymptotic scattered wavefunction takes form [91],

$$\psi(\mathbf{r}) \approx U_s e^{i\mathbf{k}\cdot\mathbf{r}} + \sum_{s'} \frac{e^{ikr}}{r} f^{s',s}(\mathbf{k}', \mathbf{k}) \tag{2.27}$$

Here, c is the speed of light, m is the mass of the particle, $\beta, \alpha_1, \alpha_2, \alpha_3$ are (4×4) matrices, U_s is a four component column vector which depends on the spin and the sign of energy of the incident particle and $f^{s',s}$ is also a four component quantity.

We will be studying Dirac Fermions in graphene systems. In the $\mathbf{K}$ valley of Graphene the hamiltonian of a free particle can be written as $\mathbf{H}_0 = v_F \sigma \cdot \mathbf{p}$ where, $\mathbf{p}$ is the momentum operator and $(\sigma_x, \sigma_y, \sigma_z)$ are the Pauli spin matrices. If we use the cylindrical polar coordinate $(x = r\cos(\theta), y = r\sin(\theta))$, then [97]

$$\mathbf{H}_0 = -i\hbar v_F \begin{bmatrix} 0 & \partial_x - i\partial_y \\ \partial_x + i\partial_y & 0 \end{bmatrix} = -i\hbar v_F \begin{bmatrix} 0 & \hat{L}_- \\ \hat{L}_+ & 0 \end{bmatrix} \tag{2.28}$$

Here, $\hat{L}_\pm = e^{\pm i\theta}\left(\partial_r \pm \frac{i}{r}\partial_\theta\right)$. $\hat{L}_\pm$ operator has properties[97]

$$\hat{L}_\pm \left[e^{im\theta} J_m(kr)\right] = \mp k e^{i(m\pm1)\theta} J_{m\pm1}(kr) \tag{2.29a}$$

$$\hat{L}_\pm \left[e^{im\theta} Y_m(kr)\right] = \mp k e^{i(m\pm1)\theta} Y_{m\pm1}(kr) \tag{2.29b}$$

Using Eq. (2.28) and (2.29), we can show that the eigenvalues of $\mathbf{H}_0$ are [97] ,

$$\psi^{e,(1)}_{m,\mathbf{k}}(r,\theta) = \frac{1}{\sqrt{2}} e^{im\theta} \begin{bmatrix} J_m(kr) \\ ie^{i\theta} J_{m+1}(kr) \end{bmatrix} \tag{2.30}$$

and

$$\psi^{e,(2)}_{m,\mathbf{k}}(r,\theta) = \frac{1}{\sqrt{2}} e^{im\theta} \begin{bmatrix} N_m(kr) \\ ie^{i\theta} N_{m+1}(kr) \end{bmatrix} \tag{2.31}$$

with eigenvalue $\hbar v_F k$ and

$$\psi^{h,(1)}_{m,\mathbf{k}}(r,\theta) = \frac{1}{\sqrt{2}} e^{im\theta} \begin{bmatrix} J_m(kr) \\ -ie^{i\theta} J_{m+1}(kr) \end{bmatrix} \tag{2.32}$$

and

$$\psi^{h,(2)}_{m,\mathbf{k}}(r,\theta) = \frac{1}{\sqrt{2}} e^{im\theta} \begin{bmatrix} N_m(kr) \\ -ie^{i\theta} N_{m+1}(kr) \end{bmatrix} \tag{2.33}$$

with eigenvalue $-\hbar v_F k$.

Where, J_m and N_m are the Bessel and Neumann functions[92]. The positive energy solutions, ($E > 0$, electrons) can be written as,

$$\Psi^e_{\mathbf{k}}(\mathbf{r}) = \sum_{m=-\infty}^{\infty} \psi^e_{m,\mathbf{k}}(r,\theta) \tag{2.34}$$

Here,

$$\psi^{e}_{m,\mathbf{k}}(r,\theta) = C_m \frac{1}{\sqrt{2}} e^{im\theta} \begin{bmatrix} J_m(kr) \\ ie^{i\theta} J_{m+1}(kr) \end{bmatrix} + D_m \frac{1}{\sqrt{2}} e^{im\theta} \begin{bmatrix} N_m(kr) \\ ie^{i\theta} N_{m+1}(kr) \end{bmatrix}$$
$$= \frac{1}{\sqrt{2}} e^{im\theta} \begin{bmatrix} \{C_m J_m(kr) + D_m N_m(kr)\} \\ ie^{i\theta} \{C_m J_{m+1}(kr) + D_m N_{m+1}(kr)\} \end{bmatrix} \tag{2.35}$$

The asymptotic form of Bessel and Neumann functions are [92],

$$J_m(kr) \xrightarrow[r\to\infty]{} \sqrt{\frac{2}{\pi kr}} \cos\Big(kr - \frac{m\pi}{2} - \frac{\pi}{4}\Big) \tag{2.36a}$$

$$N_m(kr) \xrightarrow[r\to\infty]{} \sqrt{\frac{2}{\pi kr}} \sin\Big(kr - \frac{m\pi}{2} - \frac{\pi}{4}\Big) \tag{2.36b}$$

Using Eq. (2.35) and (2.36) the asymptotic form of the scattered wave function for positive energy particles can be written as [97],

$$\Psi^{e}_{\mathbf{k}}(\mathbf{r}) = \sum_{m=-\infty}^{\infty} A_m (kr)^{1/2} \frac{1}{\sqrt{2}} e^{im\theta} \begin{bmatrix} \cos\big(kr - \frac{m\pi}{2} - \frac{\pi}{4} + \delta_m\big) \\ ie^{i\theta} \sin\big(kr - \frac{m\pi}{2} - \frac{\pi}{4} + \delta_m\big) \end{bmatrix} \tag{2.37}$$

Here, δ_m is the phase shift due to scattering. Now, if we choose the incident wave-functions as an electron propagating along the x-axis then the incident wave-function can be expandend in terms of partial waves as,

$$\phi^{e}_{\mathbf{k}} = \frac{1}{\sqrt{2}} \begin{bmatrix} 1 \\ 1 \end{bmatrix} e^{ikx} = \sum_{m=-\infty}^{\infty} \frac{1}{\sqrt{2}} i^m e^{im\theta} \begin{bmatrix} J_m(kr) \\ J_m(kr) \end{bmatrix} \tag{2.38}$$

Similar to eq. (2.25), we can write the scattered wavefuntion for the electrons as,

$$\Psi^{e}_{\mathbf{k}}(\mathbf{r}) \approx \frac{1}{\sqrt{2}} \begin{bmatrix} 1 \\ 1 \end{bmatrix} e^{ikx} + \frac{e^{ikr}}{\sqrt{2r}} f(\theta) \begin{bmatrix} 1 \\ e^{i\theta} \end{bmatrix} \tag{2.39}$$

In TABLE 2.1, we compare the partial wave analysis in the scattering process of three dimensional non relativistic (NR) system [89, 90], two-dimensional non relativistic system [95, 96] and massless Dirac fermions (MDF) in graphene [44, 93, 97, 98].

Table 2.1: Comparison of scattering in three dimensional non relativistic (NR) system [89, 90], two-dimensional non relativistic system [95, 96] and massless Dirac fermions (MDF) in graphene [44, 97]:

3-dimensional NR system	**2-dimensional NR system**	**MDFs in graphene**
Scattered wavefunction $\Psi^e_{\mathbf{k}}(\mathbf{r}) \underset{r\to\infty}{\longrightarrow}$ $e^{ikx} + \frac{e^{ikr}}{r} f(\theta)$	Scattered wavefunction $\Psi^e_{\mathbf{k}}(\mathbf{r}) \underset{r\to\infty}{\longrightarrow}$ $e^{ikx} + \frac{e^{ikr}}{\sqrt{r}} f(\theta)$	Scattered wavefunction $\Psi^e_{\mathbf{k}}(\mathbf{r}) \underset{r\to\infty}{\longrightarrow}$ $\frac{1}{\sqrt{2}} \begin{bmatrix} 1 \\ 1 \end{bmatrix} e^{ikx} + \frac{e^{ikr}}{\sqrt{2r}} f(\theta) \begin{bmatrix} 1 \\ e^{i\theta} \end{bmatrix}$
Scattering amplitude $f(\theta) =$ $\frac{1}{k}\sum_{l=0}^{\infty}(2l+1)e^{i\delta_l}P_l(cos\theta)$	Scattering amplitude $f(\theta) =$ $\sqrt{\frac{2i}{\pi k}} \sum_{m=-\infty}^{\infty} e^{im\theta} e^{i\delta_m} \sin(\delta_m)$	Scattering amplitude $f(\theta) =$ $\sqrt{\frac{2i}{\pi k}} \sum_{m=-\infty}^{\infty} e^{im\theta} e^{i\delta_m} \sin(\delta_m)$
$f(\theta) \propto \frac{1}{k}$	$f(\theta) \propto \frac{1}{\sqrt{k}}$	$f(\theta) \propto \frac{1}{\sqrt{k}}$

Putting Eq. (2.37) and (2.38) on both sides of Eq. (2.39) we obtain [97],

$$A_m = \sqrt{\frac{2}{\pi}} i^m e^{i\delta_m}, \tag{2.40}$$

$$f(\theta) = \sqrt{\frac{2i}{\pi k}} \sum_{m=-\infty}^{\infty} e^{im\theta} e^{i\delta_m} \sin(\delta_m) \tag{2.41}$$

If we choose our incident particle as a hole propagating along the x axis, then the partial wave expansion of the incident wave and asymptotic scattered wave-function are,

$$\phi^h_{\mathbf{k}} = \frac{1}{\sqrt{2}} \begin{bmatrix} 1 \\ -1 \end{bmatrix} e^{ikx} = \sum_{m=-\infty}^{\infty} \frac{1}{\sqrt{2}} i^m e^{im\theta} \begin{bmatrix} J_m(kr) \\ -J_m(kr) \end{bmatrix} \tag{2.42}$$

$$\Psi^h_{\mathbf{k}}(\mathbf{r}) = \sum_{m=-\infty}^{\infty} A_m (kr)^{1/2} \frac{1}{\sqrt{2}} e^{im\theta} \begin{bmatrix} \cos\left(kr - \frac{m\pi}{2} - \frac{\pi}{4} + \delta_m\right) \\ -ie^{i\theta} \sin\left(kr - \frac{m\pi}{2} - \frac{\pi}{4} + \delta_m\right) \end{bmatrix} \tag{2.43}$$

In terms of the scattering amplitude, the scattered wave-function for a hole is,

$$\Psi^h_{\mathbf{k}}(\mathbf{r}) \approx \frac{1}{\sqrt{2}} \begin{bmatrix} 1 \\ -1 \end{bmatrix} e^{ikx} + \frac{e^{ikr}}{\sqrt{2r}} f(\theta) \begin{bmatrix} 1 \\ -e^{i\theta} \end{bmatrix}. \tag{2.44}$$

The scattering amplitude is same as the scattering of an electron. Here, we have determined the scattered wave-functions in terms of scattering phase shift. This phase shift depends on the scattering potential.

2.4 Optical Theorem

The optical theorem for non-relativistic case is shown in [90] and non-relativistic two dimensional cases in [95, 96]. In the first problem discussed in the third chapter of this thesis we discuss scattering of massless Dirac fermions. In this section, we will derive the optical theorem for the mass-less Dirac fermions in Graphene. The probability current operator in the Direction $\hat{r}$ is $\hat{J} = \hat{r}.\vec{\sigma} = \begin{bmatrix} 0 & e^{-i\theta} \\ e^{i\theta} & 0 \end{bmatrix}$

The probability current density of the scattered electrons at large distance in the direction $\hat{r}$ is

$$J_{scat} = \frac{e^{-ikr}}{\sqrt{2r}} f^*(\theta) \begin{bmatrix} 1 & e^{-i\theta} \end{bmatrix} \begin{bmatrix} 0 & e^{-i\theta} \\ e^{i\theta} & 0 \end{bmatrix} \times \frac{e^{ikr}}{\sqrt{2r}} f(\theta) \begin{bmatrix} 1 \\ e^{i\theta} \end{bmatrix} = \frac{1}{r}|f(\theta)|^2 \tag{2.45}$$

For the incident electron the probability current density in the incident direction $\hat{x}$ is,

$$J_{inc} = \frac{1}{\sqrt{2}} \begin{bmatrix} 1 & 1 \end{bmatrix} e^{-ikx} \begin{bmatrix} 0 & 1 \\ 1 & 1 \end{bmatrix} \frac{1}{\sqrt{2}} \begin{bmatrix} 1 \\ 1 \end{bmatrix} e^{ikx} = 1 \tag{2.46}$$

The differential scattering cross section can be calculated as,

$$\frac{d\sigma}{d\theta}d\theta = \frac{|J_{scat}|rd\theta}{|J_{inc}|} = |f(\theta)|^2 d\theta \tag{2.47}$$

So the differential scattering cross section is $\lambda(\theta) = \frac{d\sigma}{d\theta} = |f(\theta)|^2$

Using Eq. (2.40), the total cross section can be calculated as,

$$\lambda = \int_0^{2\pi} \lambda(\theta)d\theta = \frac{4}{k}\sum_{n=-\infty}^{\infty} \sin^2(\delta_n) \tag{2.48}$$

Using Eq. (2.40) and (2.48) we get the optical theorem,

$$\lambda = -2\left(\frac{\pi}{k}\right)^{1/2}[Ref_k(0) - Imf_k(0)] \tag{2.49}$$

2.5 BTK formalism and BDG Equation

The dynamics of charge carriers in a junction involving proximity induced superconductor(S) and other materials such as normal metal(N) or graphene(G) is given by the Bogoliubov-de-Gennes equation [29, 83–86, 99]. This equation will be helpful to understand the second and third problem addressed in this thesis and discussed in the fourth and fifth chapter of this thesis. the equation is given by

$$\begin{bmatrix} \mathcal{H} - \mu & \Delta(T) \\ \Delta^*(T) & \mu - \mathcal{T}\mathcal{H}\mathcal{T}^{-1} \end{bmatrix} \begin{bmatrix} \Psi_e \\ \Psi_h \end{bmatrix} = \varepsilon \begin{bmatrix} \Psi_e \\ \Psi_h \end{bmatrix} \tag{2.50}$$

Here $\mathcal{H}$ is Hamiltonian for the charge carriers in the given material, μ is the fermi energy, $\Delta(T)$ is the temperature dependent superconducting pair potential which couples the time reversed electron and hole states, ε is the excitation energy, Ψ_e and Ψ_h represent the electron and hole excitations and $\mathcal{T}$ is the time reversal operator. For 2DEG, the time reversal symmetry operator takes form $\mathcal{T} = \mathcal{C}$. For graphene, the time reversal operator becomes, [100],

$$\mathcal{T} = \begin{bmatrix} 0 & \sigma_z \\ \sigma_z & 0 \end{bmatrix} \mathcal{C}. \tag{2.51}$$

2.6 BdG Equation in Graphene Based Supersonducting Junctions

The superconducting junctions are made with a graphene sheet using proximity induced superconductivity. Some part of the graphene sheet is covered by superconducting electrodes. In such junctions, the charge carriers follow Dirac equation, $\mathcal{H} = \boldsymbol{p}\cdot\boldsymbol{\sigma} = -i\hbar c(\sigma_x\partial_x + \sigma_y\partial_y)$. Here, $c = \frac{1}{300}\times$ speed of light. The time reversal operator becomes [100],

$$\mathcal{T} = \begin{bmatrix} 0 & \sigma_z \\ \sigma_z & 0 \end{bmatrix} \mathcal{C}. \tag{2.52}$$

C is the operator of complex conjugation. In the absence of magnetic field, the Hamiltonian is time reversal invariant, $\mathbf{T}\mathcal{H}\mathcal{T}^{-1} = \mathcal{H}$ This makes the BdG equations[83],

$$\begin{bmatrix} \boldsymbol{p}\cdot\boldsymbol{\sigma} - \mu & \Delta(T) \\ \Delta^*(T) & \mu - \boldsymbol{p}\cdot\boldsymbol{\sigma} \end{bmatrix} \begin{bmatrix} \Psi_e \\ \Psi_h \end{bmatrix} = \varepsilon \begin{bmatrix} \Psi_e \\ \Psi_h \end{bmatrix} \tag{2.53}$$

2.6.1 Solutions in graphene

In the graphene region of the junction the DBdG equation Eq. (2.53) becomes,

$$\begin{bmatrix} \mathbf{p}.\sigma - \mu & 0 \\ 0 & \mu - \mathbf{p}.\sigma \end{bmatrix} \begin{bmatrix} \Psi_e \\ \Psi_h \end{bmatrix} = \varepsilon \begin{bmatrix} \Psi_e \\ \Psi_h \end{bmatrix}, \tag{2.54}$$

If we take the electron part of the wavefunction , $\Psi_e = \begin{bmatrix} u_1 & u_2 \end{bmatrix}^T$ and hole part of the wavefunction $\Psi_h = \begin{bmatrix} v_1 & v_2 \end{bmatrix}^T$, then this becomes,

$$\begin{bmatrix} -\mu & -i\hbar c(\partial_x - i\partial_y) & 0 & 0 \\ -i\hbar c(\partial_x + i\partial_y) & -\mu & 0 & 0 \\ 0 & 0 & \mu & i\hbar c(\partial_x - i\partial_y) \\ 0 & 0 & i\hbar c(\partial_x + i\partial_y) & \mu \end{bmatrix} \begin{bmatrix} u_1 \\ u_2 \\ v_1 \\ v_2 \end{bmatrix} = \varepsilon \begin{bmatrix} u_1 \\ u_2 \\ v_1 \\ v_2 \end{bmatrix}, \tag{2.55}$$

We can separate the electron part of the wavefunction Ψ_e and hole part of the wavefunction

Ψ_h in Eq. (4.30). The solutions are,

$$u_{1,2} = e^{iqy+ik_x x} \times \text{constant} \tag{2.56a}$$

$$v_{1,2} = e^{iqy+ik_x x} \times \text{constant} \tag{2.56b}$$

where q is transverse and $k_x = \pm k$ is longitudinal wave vector.

$$k = \left[\frac{\varepsilon + \mu}{\hbar c}\right] \sqrt{1 - \left(\frac{\hbar c q}{\varepsilon + \mu}\right)^2} \tag{2.57}$$

Using this we have four solutions of the wavefunctions in the graphene region.

$$\psi_{\mathbf{e}}^{+} = \frac{e^{iqy+ikx}}{\sqrt{\cos\alpha}} \begin{pmatrix} e^{-\frac{i\alpha}{2}} \\ e^{\frac{i\alpha}{2}} \\ 0 \\ 0 \end{pmatrix}, \tag{2.58}$$

$$\psi_{\mathbf{e}}^{-} = \frac{e^{iqy-ikx}}{\sqrt{\cos\alpha}} \begin{pmatrix} e^{\frac{i\alpha}{2}} \\ -e^{-\frac{i\alpha}{2}} \\ 0 \\ 0 \end{pmatrix}, \tag{2.59}$$

$$\psi_{\mathbf{h}}^{+} = \frac{e^{iqy+ik'x}}{\sqrt{\cos\alpha'}} \begin{pmatrix} 0 \\ 0 \\ e^{-\frac{i\alpha'}{2}} \\ -e^{\frac{i\alpha'}{2}} \end{pmatrix}, \tag{2.60}$$

$$\psi_{\mathbf{h}}^{-} = \frac{e^{iqy-ik'x}}{\sqrt{\cos\alpha'}} \begin{pmatrix} 0 \\ 0 \\ e^{\frac{i\alpha'}{2}} \\ e^{-\frac{i\alpha'}{2}} \end{pmatrix}. \tag{2.61}$$

Where,

$$\alpha = \text{angle of incidence of electron} = \sin^{-1}\left(\frac{\hbar c q}{\varepsilon + \mu}\right), \tag{2.62a}$$

$$\alpha' = \text{angle of reflection of hole} = \sin^{-1}\left(\frac{\hbar c q}{\varepsilon - \mu}\right), \tag{2.62b}$$

$$q = \text{transverse wave vector}, \tag{2.62c}$$

$$k = \text{longitudinal wave vector of electron} = \frac{\varepsilon + \mu}{\hbar c}\cos\alpha, \tag{2.62d}$$

$$k' = \text{longitudinal wave vector of hole} = \frac{\varepsilon - \mu}{\hbar c}\cos\alpha'. \tag{2.62e}$$

The factors $\frac{1}{\sqrt{\cos\alpha}}$ and $\frac{1}{\sqrt{\cos\alpha'}}$ ensure that all these four states carry same current. The current operator is $\hat{J} = \frac{\hbar}{2mi}\left(\Psi^\dagger \frac{\partial \Psi}{\partial x} - \Psi \frac{\partial \Psi^\dagger}{\partial x}\right)$.

2.6.2 Solutions in Superconductor

In the superconducting region(S) DBdG equation Eq. (2.53) becomes,

$$\begin{bmatrix} \mathbf{p}.\sigma - U_o - \mu & \Delta_o e^{i\phi} \\ \Delta_o e^{-i\phi} & U_o + \mu - \mathbf{p}.\sigma \end{bmatrix} \begin{bmatrix} \Psi_e \\ \Psi_h \end{bmatrix} = \varepsilon \begin{bmatrix} \Psi_e \\ \Psi_h \end{bmatrix}, \tag{2.63}$$

Here, U_0 is an electrostatic potential applied in the S region. This can be adjusted by gate voltage or doping and ϕ is the superconducting phase. The four solutions of this equation for a given energy ε and transverse wave vector q are

$$\psi_1 = e^{iqy + ik_o x - k_i x} \begin{pmatrix} e^{i\beta} \\ e^{i\beta + i\gamma} \\ e^{-i\phi} \\ e^{-i\phi + i\gamma} \end{pmatrix}, \tag{2.64}$$

$$\psi_2 = e^{iqy + ik_o x + k_i x} \begin{pmatrix} e^{-i\beta} \\ e^{-i\beta + i\gamma} \\ e^{-i\phi} \\ e^{-i\phi + i\gamma} \end{pmatrix}, \tag{2.65}$$

$$\psi_3 = e^{iqy-ik_o x-k_i x}\begin{pmatrix} e^{-i\beta} \\ -e^{-i\beta-i\gamma} \\ e^{-i\phi} \\ -e^{-i\phi-i\gamma} \end{pmatrix}, \tag{2.66}$$

$$\psi_4 = e^{iqy-ik_o x+k_i x}\begin{pmatrix} e^{i\beta} \\ -e^{i\beta-i\gamma} \\ e^{-i\phi} \\ -e^{-i\phi-i\gamma} \end{pmatrix}, \tag{2.67}$$

Here,

$$\beta = \begin{cases} \cos^{-1}\left(\frac{\varepsilon}{\Delta_o}\right) & \text{if } \varepsilon < \Delta_o \\ -i\cosh^{-1}\left(\frac{\varepsilon}{\Delta_o}\right) & \text{if } \varepsilon > \Delta_o \end{cases} \tag{2.68}$$

$$\gamma = \sin^{-1}\left[\frac{\hbar cq}{U_o+\mu}\right] \tag{2.69}$$

$$k_o = \sqrt{\left(\frac{U_o+\mu}{\hbar c}\right)^2 - q^2} \tag{2.70}$$

$$k_i = \frac{(U_o+\mu)\Delta_o}{\hbar^2 c^2 k_o}\sin\beta \tag{2.71}$$

Now as we always have $|q| \leq \frac{\mu}{\hbar c}$ and if we assume $U_o \gg \mu, \varepsilon$ then, $\gamma \to 0$, $k_o \to \frac{U_o}{\hbar c}$ and $k_i \to \frac{\Delta_o}{\hbar c}\sin\beta$. In these limit the four basis states[83] in S becomes

$$\psi_1 = e^{iqy+ik_o x-k_i x}\begin{pmatrix} e^{i\beta} \\ e^{i\beta} \\ e^{-i\phi} \\ e^{-i\phi} \end{pmatrix}, \tag{2.72}$$

$$\psi_2 = e^{iqy+ik_o x+k_i x}\begin{pmatrix} e^{-i\beta} \\ e^{-i\beta} \\ e^{-i\phi} \\ e^{-i\phi} \end{pmatrix}, \tag{2.73}$$

$$\psi_3 = e^{iqy-ik_o x-k_i x}\begin{pmatrix} e^{-i\beta} \\ -e^{-i\beta} \\ e^{-i\phi} \\ -e^{-i\phi} \end{pmatrix}, \tag{2.74}$$

$$\psi_4 = e^{iqy-ik_o x+k_i x}\begin{pmatrix} e^{i\beta} \\ -e^{i\beta} \\ e^{-i\phi} \\ -e^{-i\phi} \end{pmatrix}, \tag{2.75}$$

2.6.3 Andreev Reflection

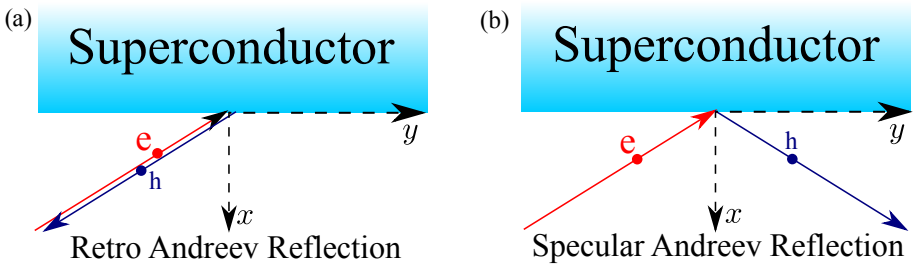

FIG. 2.1: Schematic diagram of (a) retro Andreev reflection and (b) specular Andreev reflection. The arrows denote the direction of velocity. The red circle denotes negatively charged electron and blue circle denotes positively charged hole.

Andreev reflection is a process at a normal metal–superconductor interface in which an incoming electron from the normal side is retroreflected as a hole, while a Cooper pair is transmitted into the superconductor[101]. This mechanism ensures charge and momentum conservation at the boundary and plays a central role in transport phenomena in hybrid superconducting systems. In conventional metals, Andreev reflection is called retro Andreev reflection(RAR), where the reflected hole retraces the path of the incoming electron. In graphene, however, the linear Dirac-like dispersion allows the reflected hole to occupy the valence band instead of the conduction band. This leads to specular Andreev reflection(SAR), where the hole is reflected at a positive angle, symmetric to the incident electron with respect to the interface normal, rather than retracing its trajectory[83]. The coexistence of retro and specular Andreev reflection makes graphene-based junctions fundamentally different from normal metals, enabling richer transport behavior and unique quantum interference effects. The incident and reflected angles α and α' are defined in Eq. (2.62a) and (2.62b). In the range $\mu \ll \varepsilon$, we have $\alpha = \alpha'$. SAR dominates in

this regime. Again in the range $\mu \gg \varepsilon$, we have $\alpha = -\alpha'$. RAR dominates in this regime.

2.7 Time Reversal Symmetry Breaking of BdG Equation in Presence of Uniform Magnetic Field

2.7.1 Bogoliubov-de-Gennes Equation for S-2DEG

In Josephson junctions made in the non-relativistic system, the Bogoliubov-de Gennes equation becomes[79, 84, 102, 103],

$$\begin{bmatrix} H_0 - \mu & \Delta \\ \Delta^* & \mu - H_0^* \end{bmatrix} \begin{bmatrix} \Psi_e \\ \Psi_h \end{bmatrix} = E \begin{bmatrix} \Psi_e \\ \Psi_h \end{bmatrix} \tag{2.76}$$

Here, H_0 is the single electron Hamiltonian, Δ is the pair potential, and μ is the Fermi energy. In the presence of magnetic field $\mathbf{B}$ with vector potential $\mathbf{A}$ and external potential $V(x)$ the single electron hamiltonian becomes,

$$\begin{aligned} H_0 &= \frac{1}{2m}\left(\mathbf{p} - e\mathbf{A}\right)^2 + V(x) \\ &= \frac{1}{2m}\left(-i\hbar\nabla - e\mathbf{A}\right)^2 + V(x) \end{aligned}$$

Now,

$$\begin{aligned} H_0^* &= \frac{1}{2m}\left(i\hbar\nabla - e\mathbf{A}\right)^2 + V(x) \\ &= \frac{1}{2m}\left(-i\hbar\nabla + e\mathbf{A}\right)^2 + V(x) \\ &= \frac{1}{2m}\left(\mathbf{p} + e\mathbf{A}\right)^2 + V(x) \end{aligned}$$

This makes the BdG equation [75, 87] in NS junction as,

$$\begin{bmatrix} \frac{1}{2m}\left(\mathbf{p} - e\mathbf{A}\right)^2 + V(x) - \mu & \Delta \\ \Delta^* & \mu - \frac{1}{2m}\left(\mathbf{p} + e\mathbf{A}\right)^2 - V(x) \end{bmatrix} \begin{bmatrix} \Psi_e \\ \Psi_h \end{bmatrix} = E \begin{bmatrix} \Psi_e \\ \Psi_h \end{bmatrix} \tag{2.77}$$

Now, seeing (2.77), we can understand that the external potential does not change sign with respect to the momentum but the magnetic vector potential changes sign with respect to momentum in electron and hole part of the hamiltonians. This happens since the magnetic vector potential changes sign under the time reversal[90].

2.7.2 Time Reversal Symmetry Breaking in Graphene- Superconductor Junctions

The single particle hamiltonian graphene in the presence of an external potential $V(x)$ is

$$\mathcal{H} = \begin{bmatrix} H_+ & 0 \\ 0 & H_- \end{bmatrix} \tag{2.78}$$

where, $H_\pm = -i\hbar v_F(\sigma_x\partial_x \pm \sigma_y\partial_y) + V(x)$. The time reversal operator for this Hamiltonian is

$$\mathcal{T} = \begin{bmatrix} 0 & \sigma_z \\ \sigma_z & 0 \end{bmatrix} C = \mathcal{T}^{-1} \tag{2.79}$$

Here C is the complex conjugation operator and it satisfies the equation $\mathcal{T}\mathcal{H}\mathcal{T}^{-1} = \mathcal{H}$.

In the presence of a magnetic field, the Hamiltonian from (2.78) is written in valley isotropic basis[86] by making a unitary transformation, $H = U\mathcal{H}U^\dagger$ and $T = U\mathcal{T}U^\dagger$. Where, $U = \frac{1}{2}(\tau_0 + \tau_z) \otimes \sigma_0 + \frac{1}{2}(\tau_0 - \tau_z) \otimes \sigma_x$

Using this U becomes,

$$U = \begin{bmatrix} 1 & 0 & 0 & 0 \\ 0 & 1 & 0 & 0 \\ 0 & 0 & 0 & 1 \\ 0 & 0 & 1 & 0 \end{bmatrix} \tag{2.80}$$

This matrix satisfies $U^\dagger U = I_4$. After the unitary transformation, the Hamiltonian be-

comes,

$$
\begin{aligned}
H &= U\mathcal{H}U^{\dagger} \\
&= \begin{bmatrix} 1 & 0 & 0 & 0 \\ 0 & 1 & 0 & 0 \\ 0 & 0 & 0 & 1 \\ 0 & 0 & 1 & 0 \end{bmatrix} \begin{bmatrix} V(x) & v_F(p_x - ip_y) & 0 & 0 \\ v_F(p_x + ip_y) & V(x) & 0 & 0 \\ 0 & 0 & V(x) & v_F(p_x + ip_y) \\ 0 & 0 & v_F(p_x + ip_y) & V(x) \end{bmatrix} \begin{bmatrix} 1 & 0 & 0 & 0 \\ 0 & 1 & 0 & 0 \\ 0 & 0 & 0 & 1 \\ 0 & 0 & 1 & 0 \end{bmatrix} \\
&= \begin{bmatrix} V(x) & v_F(p_x - ip_y) & 0 & 0 \\ v_F(p_x + ip_y) & V(x) & 0 & 0 \\ 0 & 0 & V(x) & v_F(p_x - ip_y) \\ 0 & 0 & v_F(p_x + ip_y) & V(x) \end{bmatrix} \\
&= v_F\, \tau_0 \otimes (\mathbf{p} \cdot \boldsymbol{\sigma} + V(x))
\end{aligned}
$$

In the presence of a magnetic field this Hamiltonian is transformed to,

$$H = v_F \tau_0 \otimes [(\mathbf{p} + e\mathbf{A}) \cdot \sigma + V(x)] \tag{2.81}$$

The time reversal operator becomes,

$$T = U\mathcal{T}U^{\dagger} = \begin{bmatrix} 0 & 0 & 0 & 1 \\ 0 & 0 & -1 & 0 \\ 0 & -1 & 0 & 0 \\ 1 & 0 & 0 & 0 \end{bmatrix} C = \begin{bmatrix} 0 & i\sigma_y \\ -i\sigma_y & 0 \end{bmatrix} C = -(\tau_y \otimes \sigma_y)C \tag{2.82}$$

We can also observe that this time reversal operator also satisfies $TT^{-1} = I_4$. This is only a transformation. The wavefunctions obtained from the Eq. (2.81) can be transformed to older hamiltonian with the reverse tranformation, although the eigenvalues remain same. We shall now use Eq. (2.81) and Eq. (2.82) to calculate the DBdG equation of dimension (8×8) from

Eq. (2.76),

$$
\begin{aligned}
H-\mu &= \begin{bmatrix} v_F\left[(\mathbf{p}+e\mathbf{A})\cdot\sigma+V(x)-\mu\right] & 0 \\ 0 & v_F\left[(\mathbf{p}+e\mathbf{A})\cdot\sigma+V(x)-\mu\right] \end{bmatrix} \\
&= \begin{bmatrix} v_F\left[\pi\cdot\sigma+V(x)-\mu\right] & 0 \\ 0 & v_F\left[\pi\cdot\sigma+V(x)-\mu\right] \end{bmatrix} \\
&= \begin{bmatrix} V(x)-\mu & v_F(\pi_x-i\pi_y) & 0 & 0 \\ v_F(\pi_x+i\pi_y) & V(x)-\mu & 0 & 0 \\ 0 & 0 & V(x)-\mu & v_F(\pi_x-i\pi_y) \\ 0 & 0 & v_F(\pi_x+i\pi_y) & V(x)-\mu \end{bmatrix}
\end{aligned} \tag{2.83}
$$

$$
\begin{aligned}
THT^{-1} = \begin{bmatrix} 0 & 0 & 0 & 1 \\ 0 & 0 & -1 & 0 \\ 0 & -1 & 0 & 0 \\ 1 & 0 & 0 & 0 \end{bmatrix} C \begin{bmatrix} V(x) & v_F(\pi_x-i\pi_y) & 0 & 0 \\ v_F(\pi_x+i\pi_y) & V(x) & 0 & 0 \\ 0 & 0 & V(x) & v_F(\pi_x-i\pi_y) \\ 0 & 0 & v_F(\pi_x+i\pi_y) & V(x) \end{bmatrix} \\
\times \begin{bmatrix} 0 & 0 & 0 & 1 \\ 0 & 0 & -1 & 0 \\ 0 & -1 & 0 & 0 \\ 1 & 0 & 0 & 0 \end{bmatrix} C
\end{aligned} \tag{2.84}
$$

Here, $\boldsymbol{\pi} = \mathbf{p} + e\mathbf{A}$

$$
\begin{aligned}
THT^{-1} = & \begin{bmatrix} 0 & 0 & 0 & 1 \\ 0 & 0 & -1 & 0 \\ 0 & -1 & 0 & 0 \\ 1 & 0 & 0 & 0 \end{bmatrix} C \\
& \times \begin{bmatrix} 0 & \hbar v_F(-i\partial_x - \partial_y) & 0 & 0 \\ \hbar v_F(-i\partial_x + \partial_y) & 0 & 0 & 0 \\ 0 & 0 & 0 & \hbar v_F(-i\partial_x - \partial_y) \\ 0 & 0 & \hbar v_F(-i\partial_x + \partial_y) & 0 \end{bmatrix} \\
& \times \begin{bmatrix} 0 & 0 & 0 & 1 \\ 0 & 0 & -1 & 0 \\ 0 & -1 & 0 & 0 \\ 1 & 0 & 0 & 0 \end{bmatrix} C \\
& + \begin{bmatrix} 0 & 0 & 0 & 1 \\ 0 & 0 & -1 & 0 \\ 0 & -1 & 0 & 0 \\ 1 & 0 & 0 & 0 \end{bmatrix} C \begin{bmatrix} V(x) & ev_F(A_x - iA_y) & 0 & 0 \\ ev_F(A_x + iA_y) & V(x) & 0 & 0 \\ 0 & 0 & V(x) & ev_F(A_x - iA_y) \\ 0 & 0 & ev_F(A_x + iA_y) & V(x) \end{bmatrix} \\
& \times \begin{bmatrix} 0 & 0 & 0 & 1 \\ 0 & 0 & -1 & 0 \\ 0 & -1 & 0 & 0 \\ 1 & 0 & 0 & 0 \end{bmatrix} C \\
= & \begin{bmatrix} 0 & 0 & 0 & 1 \\ 0 & 0 & -1 & 0 \\ 0 & -1 & 0 & 0 \\ 1 & 0 & 0 & 0 \end{bmatrix} \begin{bmatrix} 0 & \hbar v_F(i\partial_x - \partial_y) & 0 & 0 \\ \hbar v_F(i\partial_x + \partial_y) & 0 & 0 & 0 \\ 0 & 0 & 0 & \hbar v_F(i\partial_x - \partial_y) \\ 0 & 0 & \hbar v_F(i\partial_x + \partial_y) & 0 \end{bmatrix} \begin{bmatrix} 0 & 0 & 0 & 1 \\ 0 & 0 & -1 & 0 \\ 0 & -1 & 0 & 0 \\ 1 & 0 & 0 & 0 \end{bmatrix} \\
& + \begin{bmatrix} V(x) & -ev_F(A_x - iA_y) & 0 & 0 \\ -ev_F(A_x + iA_y) & V(x) & 0 & 0 \\ 0 & 0 & V(x) & -ev_F(A_x - iA_y) \\ 0 & 0 & -ev_F(A_x + iA_y) & V(x) \end{bmatrix}
\end{aligned}
$$

$$
\begin{aligned}
&= \begin{bmatrix} 0 & \hbar v_F(p_x - ip_y) & 0 & 0 \\ \hbar v_F(p_x + ip_y) & 0 & 0 & 0 \\ 0 & 0 & 0 & \hbar v_F(p_x - ip_y) \\ 0 & 0 & \hbar v_F(p_x + ip_y) & 0 \end{bmatrix} \\
&\quad + \begin{bmatrix} V(x) & -ev_F(A_x - iA_y) & 0 & 0 \\ -ev_F(A_x + iA_y) & V(x) & 0 & 0 \\ 0 & 0 & V(x) & -ev_F(A_x - iA_y) \\ 0 & 0 & -ev_F(A_x + iA_y) & V(x) \end{bmatrix} \\
&= \begin{bmatrix} V(x) & v_F(\bar{\pi}_x - i\bar{\pi}_y) & 0 & 0 \\ v_F(\bar{\pi}_x + i\bar{\pi}_y) & V(x) & 0 & 0 \\ 0 & 0 & V(x) & v_F(\bar{\pi}_x - i\bar{\pi}_y) \\ 0 & 0 & v_F(\bar{\pi}_x + i\bar{\pi}_y) & V(x) \end{bmatrix}
\end{aligned} \tag{2.85}
$$

Here, $\bar{\boldsymbol{\pi}} = \mathbf{p} - e\mathbf{A}$.

$$
\begin{aligned}
THT^{-1} &= \begin{bmatrix} v_F\left[(\mathbf{p} - e\mathbf{A}) \cdot \sigma + V(x)\right] & 0 \\ 0 & v_F\left[(\mathbf{p} - e\mathbf{A}) \cdot \sigma + V(x)\right] \end{bmatrix} \\
&= v_F \tau_0 \otimes \left[(\mathbf{p} - e\mathbf{A}) \cdot \sigma\right] + V(x)
\end{aligned} \tag{2.86}
$$

We can observe that the scalar potential $V(x)$ does not invert sign but the magnetic vector potential $\mathbf{A}$ change sign under the time reversal operation[90].

This makes the DBdG equation in presence of external potential $V(x)$ and magnatic vector potential $\mathbf{A}(x)$ as,

$$
\begin{bmatrix} v_F\tau_0 \otimes (\mathbf{p} + e\mathbf{A}) \cdot \sigma + V(x) - \mu & \Delta \\ \Delta^* & \mu - v_F\tau_0 \otimes (\mathbf{p} - e\mathbf{A}) \cdot \sigma - V(x) \end{bmatrix} \begin{bmatrix} \Psi_e \\ \Psi_h \end{bmatrix} = \varepsilon \begin{bmatrix} \Psi_e \\ \Psi_h \end{bmatrix} \tag{2.87}
$$

CHAPTER 3

Scattering of Massless Dirac Fermions from a Two Dimensional Quantum Dot Lattice

This chapter is based on the published work - "*Electronic analogue of Fourier optics with massless Dirac fermions scattered by quantum dot lattice*", Partha Sarathi Banerjee, Rahul Marathe and Sankalpa Ghosh, *J. Opt.*, **26**, 095602.

The unique transmission properties of massless Dirac fermions (MDF) in graphene through potential landscapes created by a variety of electromagnetic (EM) fields, particularly in the ballistic regime [4, 11, 20, 56, 71, 104], and its similarity with the light transmission through an optical medium with unconventional dielectric properties such as metamaterials [105, 106] make graphene an excellent material to realize electron optics-based devices in a solid state system. The realisation of negative refraction [12], chiral Veselago lensing of MDF in two [3] and three dimensions [5], tunable Veselago interference in a bipolar graphene microcavity [107], creation of a Dirac fermion microscope [2], collimation [1, 7, 108], and different type of interferometers [15–18], gate tunable beam-splitter of such MDF [6], Fabry-pérot resonator in graphene/hBN moiré super-lattice [19], gradient index electron optics in graphene p-n junction [109], Mie scattering in graphene, [14] are few milestones in this direction. Most of these experimental and theoretical studies are based on theoretical modelling of Dirac fermions scattered by the potential, which are constant in one direction [4, 7, 11, 20–22, 54, 56, 63, 71, 104, 110, 111], and hence limit the range of applications in this fast-growing field.

New possibilities can emerge if the EM potential that can scatter such MDF can vary along both transverse directions. For example, in the well-known Fraunhofer diffraction, when the observation point is significantly distant(z) from the diffracting object dubbed as the far-field case, the field distribution at the observation plane is the Fourier transform of the aperture function($A(x', y')$) [25–28, 112–114]. The diffracting object is positioned at the front focal plane of a lens, resulting in the generation of a Fourier transform of the object at the back focal plane of the lens, thereby satisfying the conditions for the Fraunhofer approximation($z >> [x'^2 + y'^2]_{\text{max}}/\lambda$)

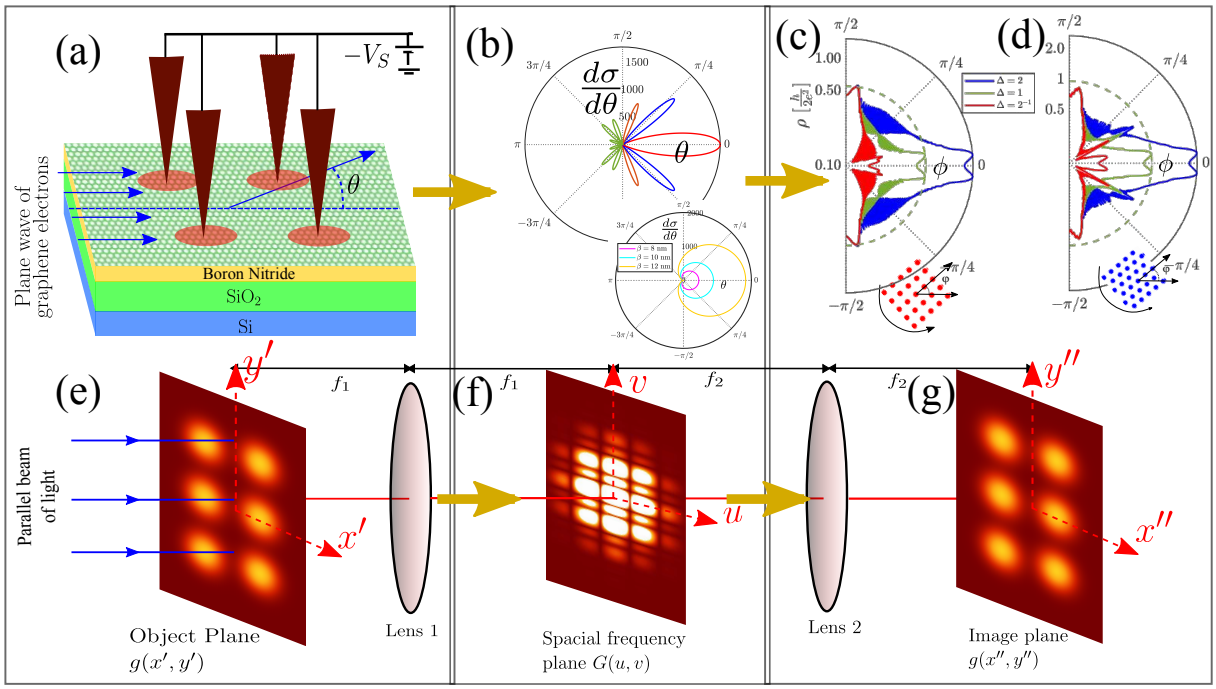

FIG. 3.1: (a) The schematic diagram of a plane wave (direction shown in blue arrows) of charge carriers in ballistic graphene that are modelled as MDF under ambient conditions, getting scattered by a two-dimensional array of Gaussian quantum dot(QD) potentials created by STM tips. (b) The polar plot of the DSC for a square lattice of QDs as given by Eq. (3.3a), of dimension $N_1 = 10$,$N_2 = 0$ and orientation $\phi = 0$. The central maxima at $\theta = 0$ is multiplied with 1.6×10^{-3} for better visibility. The first maxima on both sides are multiplied by 0.8×10^{-2}. The second ones are multiplied by 0.32 for better visibility with respect to the other smaller peaks. In the inset we have shown the differential scattering cross section for a single QD for differential values of β. In (c) and (d) the angle-resolved dc-resistivity of the system parallel to the direction of propagation of the incoming plane wave of graphene electrons is plotted under this scattering potential rotated at an arbitrary angle. The resistivity pattern for square and hexagonal lattices of QDs is shown in (c) and (d) for $N_2 = 100$. The resistivity at $\phi = 0°$ and $90°$ is the same for the square lattice but not in the case of the hexagonal lattice. In Figs. (e)-(g) we compare the process described in (a)-(d) with the two-dimensional optical spatial frequency processor, whereas a short thesaurus listing various analogue quantities in these two systems is given in TABLE 3.1. In (e) we show that the object is positioned in the front focal plane of lens 1. The Fourier transform of the object distribution is found in the back focal plane of lens 1 as shown in (f). This plane is called spatial frequency plane [25, 26]. At the image plane in (g) the object distribution is recovered. This figure is taken from our published work [44].

as depicted in FIG. 3.1 and described in TABLE 3.1. The framework of Fourier optics was introduced in a seminal work by P. M. Duffieux [112] and later elucidated in detail in the classic textbook of Born and Wolf [27]. In this work we show that an electronic analogue of this situation can be realized in a fully two-dimensional (2D) scattering model, where the scattering of such MDF takes place from a two-dimensional superlattice potential that can be realised by creating an electrostatically defined array of quantum dots (QDs) on the surface of single-layer graphene[51, 53, 55, 115–120]

The scattering of electrons by gate-defined QDs with sharp p-n junction has been theoretically studied using the Mie scattering [14] and multiple scattering theory [51, 55, 120]. In comparison to those approaches, in this paper using first Born approximation, we show that, the differential scattering cross-section (DSC) of a scattering potential is proportional to the Fourier transform of the potential profile. This is analogous to intensity in the back focal plane in the case of Fraunhofer diffraction pattern [27, 112]. However, due to Klein tunneling and absence of back-scattering, the MDFs in graphene are mainly transmitted towards the forward region which makes graphene scattering interesting. Particularly in the inset of FIG. 3.1 (b) we show the differential scattering cross-section from a single QD forms a cardioid like pattern which combine the effects of Mie scattering and Klein tunneling for the gaussian QD we are considering. In this framework we showed how using dc-resistivity, an experimentally measurable quantity which is dependent on this DSC, we can analyze the properties of the scattering potential in a way that is reminiscent of optical image processing. While in optical image processing a second lens is used to reconstruct the image (depicted in FIG. 3.1), similar thing is however not possible in our system. To overcome this limitation we have introduced another degree of freedom, rotation angle ϕ, which is the angle between the direction of propagation of incident plane wave and the symmetry axis of the two dimensional QD lattice (TDQDL). By doing Fourier analysis of this dc resistivity we can get information about the symmetry and lattice configuration, lattice constant, size and location of defect of the scattering lattice. In a moiré pattern of two TDQDL, we have shown that the Fourier analysis can give us the information about the symmetries (moiré pattern of two hexagonal/square lattices) and commensurate conditions.

Particularly in the ballistic regime, with the Fermi velocity $v_F \sim 10^6$ m s^{-1}, the mean free path of the charge carriers in graphene are several microns [121–123] $\gg$ the size of ($\sim$ 10 nm) [124] such scatterers, and the Fraunhoffer criterion is satisfied [123, 125, 126]. In order to ob-

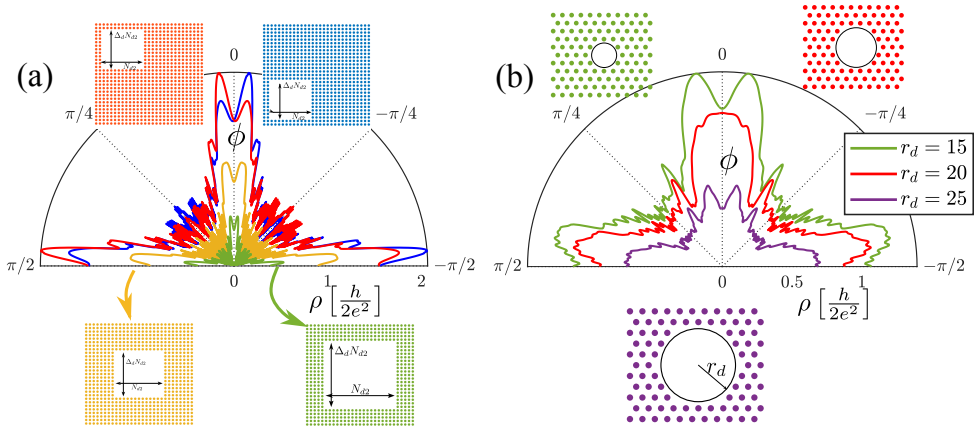

FIG. 3.2: Resistivity pattern for (a) square QD lattice of size $N_2 = 200$ and $\Delta = 1$ with square defect region with different sizes and (b) hexagonal QD lattice of size $N_2 = 61$ and $\Delta = 1$ with circular defect region of different radiuses. In (a), The resistivity pattern is symmetric on both sides of $\phi = 0$ only when the defect region is centred at the origin and for the blue curve, we have removed scatterers from $n_1 = 10$ to 110 and $n_2 = 10$ to 110. For the orange curve $n_1 = 10$ to 110 and $n_2 = 90$ to 190. In (b), the defect region is placed in the centre of the original QD lattice. Here, the resistivity pattern is symmetric on both sides of $\phi = 0$. Here, $\beta = 10$ nm. This figure is taken from our published work [44].

serve a clear diffraction pattern in the optical case, the aperture length must be comparable to the wavelength of light [27, 28]. This is ensured in our analogue solid-state system by considering that the lattice spacing ($\sim$ 40 nm) and characteristic length ($\sim$ 10 nm) of each barrier [124] in this QD lattice are smaller than the de Broglie wavelength calculated from the incident energy of the graphene electrons ($\sim$ 30 - 40 meV) [18]. Also, for the typical energy range we have considered, the wavevector of the MDF is much smaller than the Fermi wave vector, i.e.,$k \ll k_F$, eliminating the possibility of inter-valley scattering. The difference in K and K' valleys are separated by $10 - 11$ eV and the energy range associated with the graphene electrons are in $\sim$ 20 meV. Thus, the problem can be modelled by starting with the single-valley non-interacting Hamiltonian of the massless Dirac fermions in single-layer graphene given by $\hat{H}_0 = v_F \sigma \cdot \mathbf{p}$. Such a two-dimensional QD lattice (TDQDL) serves as two-dimensional grating for the incident charge carriers for graphene, leading to an electronic analogue of Fraunhofer diffraction pattern, but with an important distinction characterising the absence of backscattering for such MDF [58, 127]. Maintaining ballistic and phase-coherent electron transport over the length scale of a periodic gate array requires high-mobility, hBN-encapsulated graphene, which has already been demonstrated in electron-optics experiments [128, 129]. Furthermore, advances in nanoscale electrostatic gating enable controlled formation of smooth and well-defined p–n

junctions and collimating structures, providing a realistic pathway toward engineering periodic quantum dot lattices for Dirac fermion optics [11, 130]. Also, the mismatch of maximas from each quantum dot can introduce disorder. However as we have differences between maximas, $\delta V << V_0$, it can be ignored. In realistic devices, charge puddles arising from trapped impurities in the substrate can create spatial carrier-density inhomogeneity that distorts the intended periodic potential landscape [128, 131]. In addition, lithographic edge roughness and gate-induced potential fluctuations can break the ideal lattice symmetry, although such effects can be incorporated numerically by introducing random onsite potential disorder or correlated potential fluctuations within tight-binding or Green's function simulations [132, 133]. In Sec. 3.1, we discuss the scattering of MDF from three prototype combinations of such dot lattices and lay down the basic premises of our theoretical approach.

3.1 Theory

3.1.1 Calculation of Differential Scattering cross sections for three prototype cases

In **Chapter 2**, we have derived the Lippmann-Schwinger equation for MDFs in Eq. (2.7). We have also calculated the Green's function for MDFs in Eq. (2.16). Using those definitions, the scattered state of such MDF $|\Psi_{\mathbf{k}}\rangle$ from an arbitrary scattering potential V can be obtained by finding out the solutions of $\left(\hat{H}_0 + \hat{V}\right)|\Psi_{\mathbf{k}}\rangle = E\,|\Psi_{\mathbf{k}}\rangle$ using the Lippmann-Schwinger formalism and can be written as [90, 96]

$$\Psi^{e,+}_{\mathbf{k}}(\mathbf{r}) = \phi^{e}_{\mathbf{k}}\left(\vec{r}\right) - \frac{e^{ikr}}{2\hbar v_F}\sqrt{\frac{ik}{\pi r}}\begin{bmatrix}1\\ e^{i\theta}\end{bmatrix}\left\langle \phi^{e}_{\mathbf{k}'}\middle|\hat{T}\middle|\phi^{e}_{\mathbf{k}}\right\rangle \tag{3.1}$$

where, transition operator $\hat{T} = \hat{V} + \hat{V}\hat{G}^{\pm}_0\hat{V} + \hat{V}\hat{G}^{\pm}_0\hat{V}\hat{G}^{\pm}_0\hat{V} + \ldots$ and $\hat{G}^{\pm}_0$ is the Green's function defined as $\hat{G}^{\pm}_0 = \lim_{\epsilon\to 0}\left[EI_2 - \hat{\mathbf{H}}_0 \pm i\epsilon\right]$. $(\phi^{e,h}_{\mathbf{k}})$ are respectively free particle electron and hole solutions of $\hat{H}_0\,|\phi_{\mathbf{k}}\rangle = E\,|\phi_{\mathbf{k}}\rangle$, Here, $\mathbf{k}$ is the wave-vector of the incident wave, $\mathbf{k}' = k\hat{r}$, θ is the angle between $\mathbf{k}$ and $\mathbf{k}'$. We also discussed about the transition operator in Sec. 2.2.

Realistic QD lattices that are heavily n-doped centres on a p-doped background [53, 118, 119] serves as scattering potential V as a Gaussian quantum dot array

$$V(\mathbf{r}) = \sum_n \left(\frac{V_0}{2\pi\beta^2}\right) e^{-\frac{1}{2}(\frac{\mathbf{r}-\mathbf{r_n}}{\beta})^2} \tag{3.2}$$

where $\mathbf{r_n}$s are the centres of each quantum dot where the Gaussian potential of width β forms its maxima. The quantum dots are considered such that at $\boldsymbol{r} = \boldsymbol{r_n}$, $V(\boldsymbol{r}) = V_0$. Such potential profile can be created using a needle-like electrode offered by an STM tip [53, 117–119], connected with a gate potential as shown in FIG. 3.1(a).

In experimental systems [118, 134, 135], these quantum dots are made on graphene/hBN heterostructures on SiO_2/Si substrate. The gate potential creates a stationary charge distribution in the insulating hBN underlayer, which creates the Gaussian potential profile in the graphene sheet. The SiO_2/Si substrate acts as a global back gate. To make an array of such QDs, the single electrode can be replaced by an array of such electrodes [117, 136, 137].

For the type of potential profile depicted in Eq. (3.2), the premise for Fourier electron optics(FEO) with such MDF can be developed first by evaluating differential scattering cross-sections (DSC), which we did for three carefully chosen prototype combinations of such dot lattices and subsequently demonstrating their effect on transport. The DSCs evaluated respectively are:

$$\frac{\mathrm{d}\sigma}{\mathrm{d}\theta} = \frac{1}{4\hbar^2 v_F^2}\left(\frac{k}{\pi}\right) V_0^2 \mu(\theta) M_1^2(\theta,\phi) M_2^2(\theta,\phi),$$

square lattice with dimension $(\Delta N_2 \times N_2)$,and hexagonal

lattice rotated in an angle ϕ (3.3a)

$$= \frac{kV^2\mu(\theta)}{4\pi\hbar^2 v_F^2}\left[M_1\left(N_2,\Delta,\phi,\mathbf{q}\right) M_2\left(N_2,\phi,\mathbf{q}\right) - M_1\left(N_{d2},\Delta_d,\phi,\mathbf{q}\right) M_2\left(N_{d2},\phi,\mathbf{q}\right)\right]^2$$

, square QD lattice with a defect region of rectangular shape (3.3b)

$$= \frac{kV^2\mu(\theta)}{4\pi\hbar^2 v_F^2}\left[M_1\left(N_2,\Delta,\phi-\frac{\delta}{2},\mathbf{q}\right) M_2\left(N_2,\phi-\frac{\delta}{2},\mathbf{q}\right) + M_1\left(N_2,\Delta,\phi+\frac{\delta}{2},\mathbf{q}\right) M_2\left(N_2,\phi+\frac{\delta}{2},\mathbf{q}\right)\right]^2$$

moiré pattern of two QD lattices (3.3c)

Here,

$$M_1(N_2,\Delta,\phi,\mathbf{q}) = \sin\Big(N_2\Delta d\mathbf{q}\cdot\hat{x'}/2\Big)/\sin\Big(d\mathbf{q}\cdot\hat{x'}/2\Big) \tag{3.4a}$$

$$M_2(N_2,\phi,\mathbf{q}) = \sin\Big(N_2 d\mathbf{q}\cdot\hat{y'}/2\Big)/\sin\Big(d\mathbf{q}\cdot\hat{y'}/2\Big) \tag{3.4b}$$

in Eq. (3.3) are conventional Fraunhofer diffraction patterns for an one-dimensional grating in mutually transverse direction. $\mu(\theta) = (1+\cos\theta)\exp\left[-4k^2\beta^2\sin^2(\theta/2)\right]$ is due to the gaussian aperture profile (Eq. (3.2)) modulated by a factor due to the absence of backscattering [58, 104] for MDFs in graphene , and $\mathbf{q} = \mathbf{k} - \mathbf{k}'$, $\mathbf{r}_n = n_1 d\hat{x}' + n_2 d\hat{y}'$, where n_1 and n_2 are integers, and the x', y' axis is rotated with respect to the incident electrons by an angle ϕ.

For the first case, we take QDs arranged in square and hexagonal lattice arrangement with suitable choices of $\mathbf{r_n}$. The corresponding result, which is plotted in FIG. 3.1(b) in a polar plot, mimics the well-known Fraunhofer pattern with suitable modification due to the absence of back-scattering. This can be thought of as a two-dimensional generalisation of the well-known result of scattering by a smooth p-n junction in one dimension [20], $T \sim \exp\left(-\pi k_F \beta \sin^2(\theta)/2\right)$, as the scattering decreases exponentially with β in Eq. (3.3a) as $\frac{\mathrm{d}\sigma}{\mathrm{d}\theta} \sim e^{-4k^2\beta^2\sin^2(\theta/2)}$ with a characteristic length(β in our case). In the inset of FIG. 3.1 (b), we show a polar plot of DSC from a single quantum dot. Due to Klein tunnelling, we can observe that the DSC is maximum in the forward direction and zero in the backward direction due to absence of backscattering [58, 104].

Differernce between Scattering of 2DES and Graphene Electrons

The differential scattering cross sections for electrons in a two-dimensional electron system(2DES) scattered from a square TDQDL is given by

$$\frac{\mathrm{d}\sigma}{\mathrm{d}\theta} = \left(\frac{2m}{\hbar^2}\right)^2 \left(\frac{V_0^2}{8\pi k}\right) e^{-4k^2\beta^2\sin^2\left(\frac{\theta}{2}\right)} M_1^2(\theta,\phi) M_2^2(\theta,\phi). \tag{3.5}$$

By comparing Eq. (3.3a) and (3.5), we can observe that the differential scattering cross section in graphene is proportional to $k(\sim E)$, but in 2DES, it is proportional to $1/k$ $(\sim E^{-1/2})$ [138–140]. This happens due to the fact that the Green's function for 2DES, $G_0^{NR} \propto \frac{1}{\sqrt{k}}$ [96]. However for MDFs $G_0 \propto \sqrt{k}$ [44]. Such low-energy divergence of the two-dimensional scattering cross section has been observed in ultracold atoms confined to quasi-2D traps [141, 142]. This difference of energy dependence can be understood from FIG. 3.3, where we show the transport scattering cross section for massless Dirac fermions both in the case of graphene and two-dimensional non-relativistic systems. We can observe from Eq. (3.3a) that for scattering at low energy, the differential scattering cross section for massless-Dirac fermions becomes

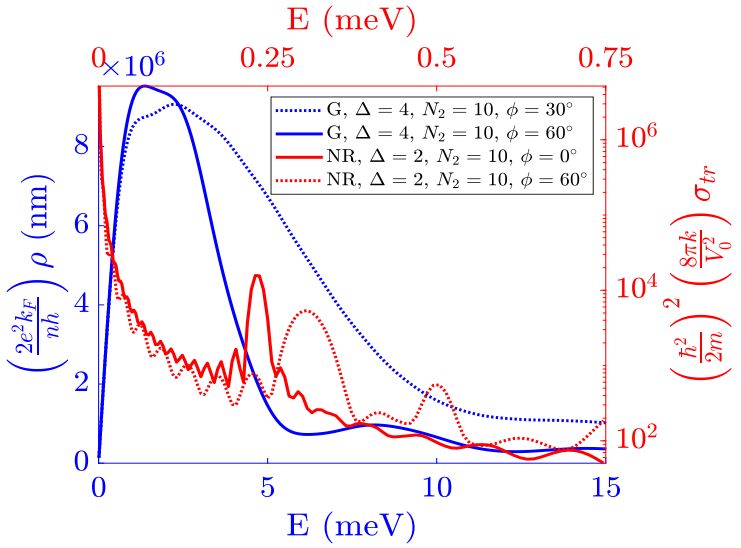

FIG. 3.3: The energy dependence of the resistivity for graphene(G) and non-relativistic(NR) two dimensional systems. This figure is taken from our published work [44].

$\frac{\mathrm{d}\sigma}{\mathrm{d}\theta} = \frac{k\Delta^2 N_2^4 V_0^2}{4\pi\hbar^2 v_F^2}(1+\cos\theta)$. That makes the transport scattering cross section $\sigma_{tr} = \left(\frac{\Delta^2 N_2^4 V_0^2}{4\hbar^2 v_F^2}\right) k$ and the resistivity becomes, $\rho = \left(\frac{n\pi^2\Delta^2 N_2^4 V_0^2}{2he^2 k_F v_F^2}\right) k$. Due to this, we see the linear variation of resistivity with E at low energies in FIG. 3.3. From Eq. (3.5) for non-relativistic electrons in 2D, at low energy the differential scattering cross section becomes, $\frac{\mathrm{d}\sigma}{\mathrm{d}\theta} = \left(\frac{2m}{\hbar^2}\right)^2 \left(\frac{V_0^2}{8\pi k}\right) \Delta^2 N_2^4$. The transport scattering cross section becomes $\sigma_{tr} = \left(\frac{mV_0\Delta N_2^2}{\hbar^2}\right)^2 \times \frac{1}{k}$. In FIG. 3.3, we see that at low energies, the transport scattering cross section becomes inversely proportional to the energy of the incident particle.

Scattering from a lattice with a defect region and moiré pattern of two QD lattices

In the next two cases, we first consider a scattering lattice made of TDQDL with defects of different shapes and sizes (Eq. (3.3b), FIG. 3.2), and then a third case of scattering potential made with moiré pattern of two square lattices of TDQDL (FIG. 3.4), making the differential scattering cross-section dependent on the twist angle(δ) between the two square TDQDLs. The scattering amplitude for the TDQDL with a defect region is the difference between the contribution from the original TDQDL scattering potential (without the defect region) and a TDQDL of the same shape and position of the defect region in Eq. (3.3b). In the third case of moiré pattern, the scattering amplitude is again the sum of the contributions from two lattices rotated with respect to each other, and the differential scattering cross section in Eq. (3.3c) is the square of this sum. This happens due to the linearity property of the Fourier transform [27]. In the

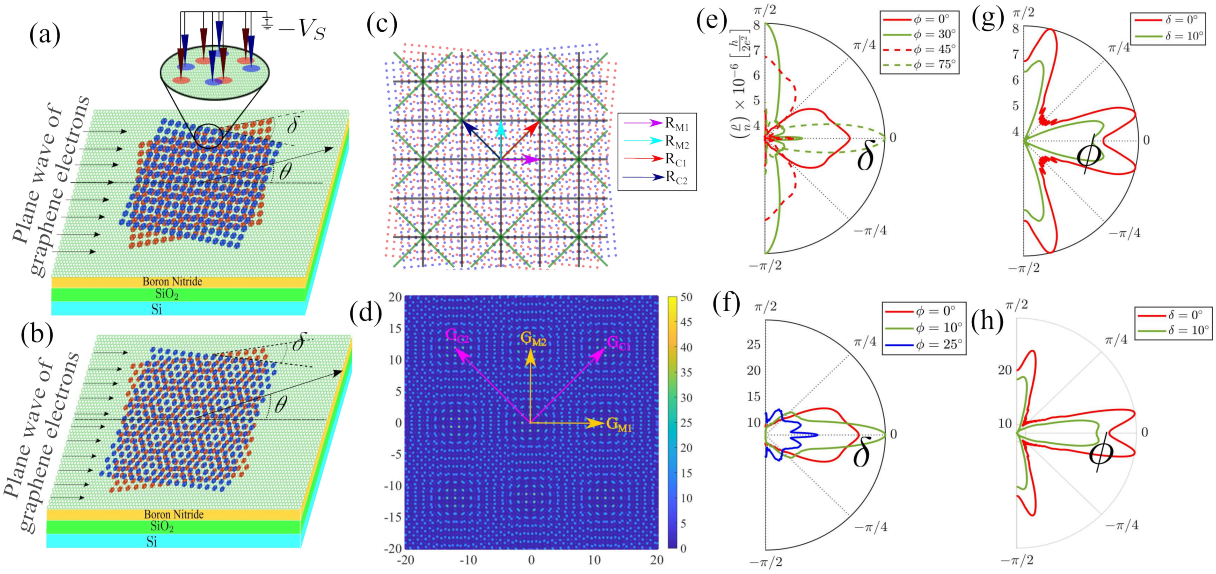

FIG. 3.4: The schematic diagram of a plane wave of massless Dirac fermions getting scattered by a moiré superlattice of two (a) square and (b) hexagonal lattices of Gaussian quantum dots(QD) in graphene. Moiré pattern made by two square lattices of TDQDL producing a commensurate structure at a twist angle, $\delta \approx 6.026°$ is shown in (c). The moiré lattice is shown in green, and the commensurate lattice is shown in black. Such quantum dots can be created in experimental system by using tips with applied gate voltage in the same way as in FIG. 3.1. In (d) $\left|\tilde{V}(\mathbf{q_1})\right|^2$ is plotted as a function of q_{1x} and q_{1y} for the above scattering potential. The resistivity pattern with fixed the mean angle(ϕ) is shown in (e) and (f) for a TDQDL scattering potential made with moiré pattern of two square and hexagonal lattices, respectively. In (g) and (h), the resistivity pattern is plotted with fixed twist angle(δ) again for a moiré pattern of two square and hexagonal lattices, respectively. This figure is taken from our published work [44].

analogous case of optical diffraction systems, this is known as Babinet's principle [27, 143, 144].

For the square TDQDL with defect region, we have considered four specific cases by varying the locations and sizes of the cavities. For a square defect region ($(\Delta_d = 1)$) in a square TDQDL, the length of the side of the square-shaped cavities(N_{d2}) is varied to vary the size of the cavities. We have also taken two cases where the centre of the defect region does not coincide with the centre of the parent square TDQDL. In FIG. 3.2 (a) we can notice that the red and blue curves are interchangeable under reflection about $\phi = 0$. This happens because $\phi = 0$ denotes the direction of propagation of the plane wave of incoming electrons. The defects corresponding to these curves are located at opposite points with respect to the direction of propagation. This shows that the resistivity pattern is sensitive to the location of the defect.

For the moiré pattern, the moire lattice vector d_M is related to the twist angle by $\delta = 2\sin^{-1}\left(\frac{d}{2d_M}\right)$ [145]. The moiré pattern produces a periodic pattern with lattice periodicities $\sqrt{2N}d_M$ [145, 146]for the commensurate angles where N is an integer. The commensurate super-cell lattice vectors [147, 148] for $\phi = 0$ are given by $\mathbf{R}_{C1} = \left(\frac{d}{2\sin(\delta/2)}\right) N(\hat{x} + \hat{y})$ and $\mathbf{R}_{C2} = \left(\frac{d}{2\sin(\delta/2)}\right) N(-\hat{x} + \hat{y})$

For every value of N, we get a set of commensurate angles. For the particular commensurate structure that we have considered for square lattice, this common period is larger than the moiré cell by factor $\sqrt{2}$ [145] (see FIG. 3.4(c)). The moiré lattice with lattice periodicity d_M is shown in green. This commensurate lattice is shown in black in FIG. 3.4(c). The primitive lattice vectors $\mathbf{R}_{C1}$ and $\mathbf{R}_{C2}$ are not same as the moiré lattice vectors $\mathbf{R}_{M1} = \left(\frac{d}{2\sin(\delta/2)}\right)\hat{x}$ and $\mathbf{R}_{M2} = \left(\frac{d}{2\sin(\delta/2)}\right)\hat{y}$. Due to the commensurate periodicity, scattering potentials made with such patterns show additional Bragg condition from Eq. (3.3c),

$$2Nk^2 d_M^2 \sin^2\left(\frac{\theta}{2}\right) = (m_1^2 + m_2^2) \tag{3.6}$$

The detailed discussion on the maximum scattering conditions is shown in Sec. 3.1.2.

3.1.2 Condition for Maximum Scattering in case of moiré pattern of two TDQDL

The differential scattering cross-section for these systems is directly proportional to $\left|\tilde{V}(\mathbf{q})\right|^2$. Here $\tilde{V}(\mathbf{q})$ is the Fourier transform of the scattering potential $V(\mathbf{r})$. In FIG. 3.5, we show the Fourier transform of the scattering potential made by a square TDQDL. The positions for the principle maximas are given by $q_{1x} = n_1(2\pi/d)$ and $q_{1y} = n_2(2\pi/d)$ where n_1 and n_2 are integers. These correspond to the Bragg condition. The secondary minimas are separated by a distance of $\left(\frac{2\pi}{Nd}\right)$. We can also notice that $\left|\tilde{V}(\mathbf{q})\right|^2$ has maximum value for the central maxima at $q_{1x} = 0$ and $q_{1y} = 0$ because the Fourier transform of the scattering potential has a Gaussian term $e^{-4k^2\beta^2\sin^2(\theta/2)}$ same as in $\mu(\theta)$ in Eq. (3.3a).

For the case of moiré pattern of two square TDQDL scattering potentials, we have shown the maximum scattering cases in FIG. 3.4 (d). We can observe that the Fourier transform is also a moiré pattern of two square patterns in inverse space. The reciprocal lattice vectors, in this

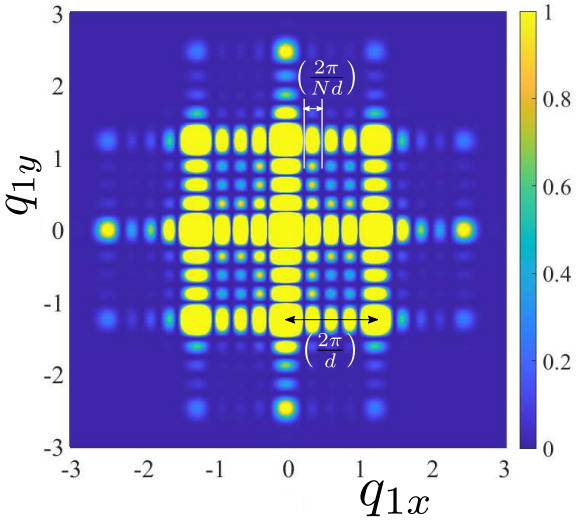

FIG. 3.5: $\left|\tilde{V}(\mathbf{q})\right|^2$ plotted as a function of q_{1x} and q_{1y} for a single layer of TDQDL for $N = 5$. This figure is taken from our published work [44].

case, is

$$\mathbf{G_{M1}} = \frac{4\pi \sin\left(\frac{\delta}{2}\right)}{d}\hat{x}, \qquad \mathbf{G_{M2}} = \frac{4\pi \sin\left(\frac{\delta}{2}\right)}{d}\hat{y} \tag{3.7}$$

$$\mathbf{G_{C1}} = \frac{4\pi \sin\left(\frac{\delta}{2}\right)}{d}N(\hat{x}+\hat{y}), \qquad \mathbf{G_{C2}} = \frac{4\pi \sin\left(\frac{\delta}{2}\right)}{d}N(\hat{y}-\hat{x}) \tag{3.8}$$

Where, N is an integer. For every value of N, we have a set of commensurate angles.

The Fourier transform produces a commensurate pattern only when the scattering potential itself produces a commensurate pattern. The Bragg conditions, which appear only in the case of commensurate lattice i.e.,Eq. (3.6) correspond to those points in FIG. 3.4 (d) for which $\mathbf{q} = m_1\mathbf{G_{C1}} + m_2\mathbf{G_{C2}}$.

3.1.3 Electronic Analogue of Fourier Optics

To understand how the above results can be interpreted as an electronics analogue of Fourier optics in a succinct way, in the left column of TABLE 3.1 we list quantities that characterise a Fraunhofer diffraction-based spatial frequency filtering in optical imaging systems [25, 26, 114] and are demonstrated in Figs. 3.1 (e), (f), (g). In the right column of the same table, we list

Table 3.1: Dictionary for various quantities in Fraunhofer diffraction in optics and their counterparts in scattering of MDF in graphene from a QD lattice:.

Fraunhofer Diffraction in optics	**Scattering of MDF in graphene from QD lattice**
Aperture profile in front focal plane, $A(\mathbf{r}')$	Scattering potential $V(\mathbf{r}')$
Field distribution at back focal plane: $G(u,v) = \frac{1}{\lambda f}\iint dx'dy'\, g(x',y')e^{-i(ux'+vy')}$	Scattering amplitude: $f(\theta) = -\sqrt{\frac{ik}{2\pi}}\frac{(1+e^{i\theta})}{2\hbar v_F} \times \iint dx'dy'\, V(x',y')e^{i(q_x x'+q_y y')}$
Intensity: $I = \lvert G(x,y)\rvert^2$	Differential scattering cross section: $\frac{d\sigma}{d\theta} = \lvert f(\theta)\rvert^2$
$u = \frac{2\pi x}{\lambda f}$, $v = \frac{2\pi y}{\lambda f}$	$-q_x$ and $-q_y$
$\frac{1}{\lambda f}$	$-\frac{1}{2\hbar v_F}\sqrt{\frac{ik}{2\pi}}\left(1+e^{-i\theta}\right)$
$\left(\frac{2\pi}{\lambda f}\right)\mathbf{r}$	$-\mathbf{q} = \mathbf{k}' - \mathbf{k}$
$\left(\frac{2\pi}{\lambda f}\right)^2 r^2$	$q^2 = 4k^2\sin^2\left(\frac{\theta}{2}\right)$

the corresponding quantities that define the analogue system of MDF scattered by a QD lattice.

From TABLE 3.1, we can observe that both the scattering amplitude in our system, $f(\theta)$ and the amplitude distribution at the spatial frequency plane in FIG. 3.1(e), $G(u,v)$ is the Fourier transform of the scattering potential $V(x',y')$ and the object distribution $g(x',y')$ respectively, whereas the presence of $(1+e^{i\theta})$ term in $f(\theta)$ of MDF indicates the absence of backscattering [58, 71, 104].

For MDF, the position coordinate ($\mathbf{r}$) is transformed to angular wave number coordinate ($\mathbf{q}$), whereas in the corresponding optical system, the coordinates of the plane of aperture, x' and y', are transformed to u and v, respectively. Correspondingly, the differential cross section, $\frac{\mathrm{d}\sigma}{\mathrm{d}\theta}$ in the case of MDF is replaced by intensity distribution I in the optical case as demonstrated in Figs. 3.1(b) and (f).

A noteworthy difference with the corresponding optical system appears when the superposition of two such TDQDL, rotated with respect to each other so that the resulting pattern is a

moiré pattern, widely studied in optics [1, 149–151] and condensed matter [147, 148, 152–156]. Such moiré patterns are studied in optical imaging to improve the microscope's imaging capabilities in Structural Imaging Microscopy [157–159]. In optical systems, the resultant aperture profile for two transparencies $g_1(x', y')$ and $g_2(x', y')$ is $g_1(x', y') \times g_2(x', y')$ [160, 161]. This leads to a new pattern which consists of new beating frequencies [162]. However, for MDF scattered by two potentials $V_1(x', y')$ and $V_2(x', y')$, the differential scattering cross-section depends on the Fourier transform of $V_1(x', y') + V_2(x', y')$. This leads to additional maximum scattering conditions from Eq. (3.3c) as shown in Eq. (3.6) and depicted in FIG. 3.4 (d). The resultant scattering potential shows a new periodicity only for commensurate angles.

The above analogy between the scattering problem of MDF from TDQDL and the Fourier optics using a 2D grating naturally leads to the question if this can be extended to the electronic analogue of optical image processing. In optical systems this is achieved through a second FT through lenses in the optical system (see FIG. 3.1(g)). In our system, we introduce another degree of freedom, by rotating our scattering potential about a transverse axis passing through the centre of the TDQDL. We define a spatial angle ϕ between the propagation direction of the MDF and the symmetry axis of the TDQDL in the graphene plane. While a direct analogy with the optical image processing is difficult, we show that some information about the structure of the TDQDL can be retrieved by calculating the dc resistivity at zero temperature for different rotation angles (ϕ). Using the semiclassical Boltzmann theory, the dc resistivity at zero temperature [93, 97, 98] is given by

$$\rho = \frac{2nv_F\sigma_{tr}}{e^2v_F^2D(E_F)} = \frac{2n}{e^2v_FD(E_F)}\int_0^{2\pi} d\theta\,(1-\cos\theta)\,\frac{\mathrm{d}\sigma}{\mathrm{d}\theta}. \tag{3.9}$$

We note that Eq. (3.9) is valid in the limit of small concentration (n) of scattering centers due to quantum dot lattice potential. Here, e =charge of an electron, v_F = Fermi velocity, $D(E_F)$ = density of states at Fermi energy and σ_{tr} is the transport scattering cross-section. Corresponding values of the resistivities in systems considered are within the typical range of observed resistivities in graphene-based systems [163–165]. Additionally, our calculated values of resistivities can also be adjusted by choosing the gate voltages applied at every QD and varying the height of the scatterers.

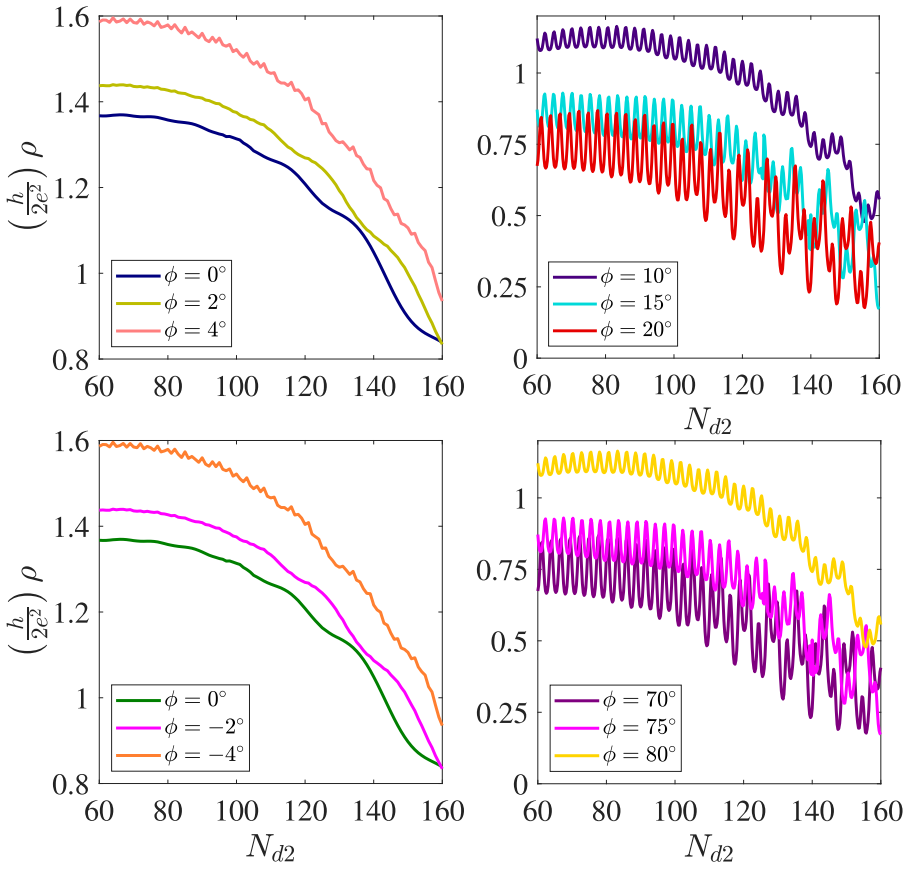

FIG. 3.6: Resistivity vs N_{d2} plot for different values of ϕ. This figure is taken from our published work [44].

3.1.4 Analysis of the angular distribution of resistivity

The corresponding results, namely the angular distribution of resistivity, are plotted in Figs. 3.1(c) and (d) for square and hexagonal TDQDL, in Figs. 3.2(a) and (b) for TDQDL with a defect region , and in Figs. 3.4 (e),(f),(g) and (h) for moiré pattern of two TDQDL lattices, to demonstrate how certain structural information of these TDQDLs can be retrieved from this angle-resolved resistivity.

We begin with the observation that $\rho(\phi)$ in Figs. 3.1(c) and (d) reflects the discrete rotational symmetry of the square and hexagonal lattice, e.g. $\frac{\mathrm{d}\sigma}{\mathrm{d}\theta}\Big|_{\Delta,N_2,\phi=0°} = \frac{\mathrm{d}\sigma}{\mathrm{d}\theta}\Big|_{\frac{1}{\Delta},\Delta N_2,\phi=90°}$ in case for square lattice, but not for the hexagonal lattice.

This may be contrasted with the observation in Figs. 3.1(c) and (d) that $\rho(-\pi/2) = \rho(\pi/2)$ for both square and hexagonal lattice of TDQDL. For TDQDL with a defect region , the resistivity pattern calculated with the help of Eq. (3.3b) and Eq. (3.9) reveals both the symmetry of the TDQDL, as well as the location and size of the defect region . In FIG. 3.2(a) comparing

between blue, red, and orange-yellow plots of the $\rho(\phi)$, we see that the location of the square defect region in the corresponding square TDQDL indeed exhibits itself in the symmetry of the resistivity plot about the $\phi = 0$ line. Similarly, comparing the cases of orange-yellow and the green plots of $\rho(\phi)$, we see that the size of the defect region , which is proportional to the number of removed scattering centres, indeed affects the magnitude of the resistivity pattern. Hexagonal TDQDL, with cavities of circular shape with radius(r_d) in FIG. 3.2(b), shows the same effect. In FIG. 3.6, we show the dependence on resistivity at different values of ϕ on the size of the defect region. Here, we can notice that the oscillations are more prominent at higher values of ϕ. This can be explained from Eq. (3.4). Near $\phi = 0$, we can write,

$$M_1(N_2, \Delta, \phi, \mathbf{q}) = \frac{\sin\left(\frac{N2\Delta dq_{1x}}{2}\right)}{\sin\left(\frac{dq_{1x}}{2}\right)} - \frac{\phi dq_{1y}}{2} \frac{N_2\Delta \sin\left(\frac{(N2\Delta-1)dq_{1x}}{2}\right)}{\sin^2\left(\frac{dq_{1x}}{2}\right)} \tag{3.10a}$$

$$M_2(N_2, \phi, \mathbf{q}) = \frac{\sin\left(\frac{N2dq_{1y}}{2}\right)}{\sin\left(\frac{dq_{1y}}{2}\right)} - \frac{\phi dq_{1x}}{2} \frac{N_2 \sin\left(\frac{(N2-1)dq_{1y}}{2}\right)}{\sin^2\left(\frac{dq_{1y}}{2}\right)} \tag{3.10b}$$

This shows that for lower values of ϕ we have less oscillations. From FIG. 3.6, we can observe that the plot is the same for angles ϕ, $(\pi/2 - \phi)$ and $-\phi$. As both the original scattering lattice is made of square lattice and of square shape($\Delta = 1$) and the defect region is also in the shape of a square, this symmetry comes.

The differential scattering cross section for the scattering potential made with a moiré pattern of two square lattices of TDQDL is shown in Eq. (3.3c). In FIG. 3.4 (d), we show $\tilde{V}(\mathbf{q})$ as a function of q_{1x} and q_{1y} (see Sec. 3.1.2). As expected, FT is also a moiré pattern of two square patterns in inverse space but multiplied by the same $\mu(\theta)$ given in Eq. (3.3c). In FIG. 3.4, (e), we show the dependence of the resistivity pattern on the twist angle(δ) for fixed values of average angle (ϕ) with the incident plane wave of massless Dirac fermions.

The most prominent features of these resistivity plots of TDQDL in Figs. 3.1(c) and (d), for TDQDL with cavities in Figs. 3.2(a), and (b), and for moiré pattern of TDQDLs in Figs. 3.4(e)-(h), are oscillations in resistivity as a function of the angular variable. To understand the oscillations in resistivity plots Figs. 3.1(c) and (d) in a more quantitative way we did an FT of the resistivity that can provide the range of these angular frequencies (see FIG. 3.8). If we choose l as the conjugate variable of ϕ, we can denote the highest angular frequency component present

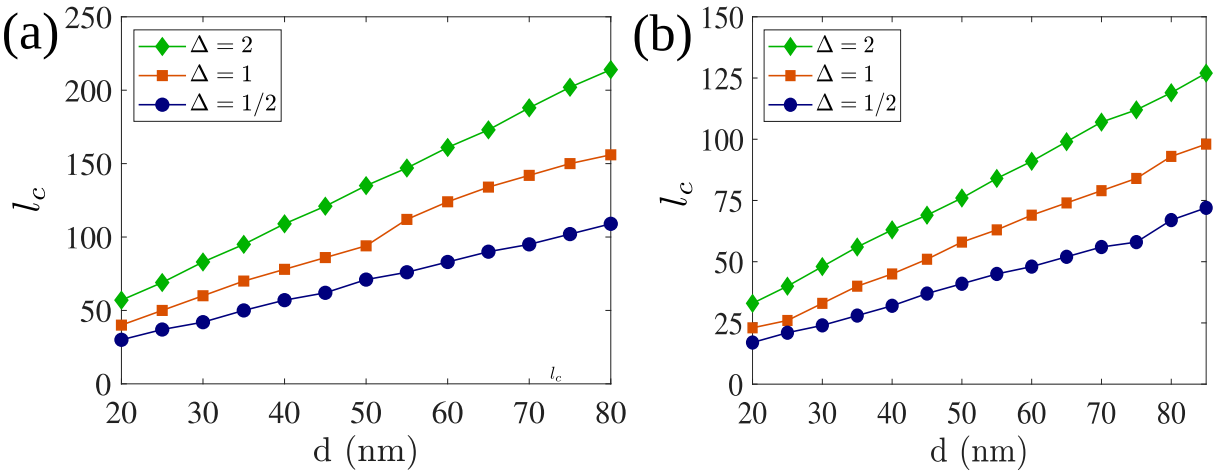

FIG. 3.7: Cut-off frequency(l_C) vs lattice constant(d) plot in the case for (a) square and TDQDL with $N_2 = 100$(b) hexagonal TDQDL with $N_2 = 30$. This figure is taken from our published work [44].

in one ρ vs ϕ curve as l_c or cut-off angular frequency for a given lattice.

For the single layer of TDQDL, l_c depends on the lattice parameter of the scattering lattice as the DSC also depends on the lattice parameter in Eq. (3.3a). In FIG. 3.7, we show the dependence of cut-off frequency on the lattice constant both for square and hexagonal lattice. Here, we see that at a particular value of d, the cut-off frequency is different for different Δ values. In FIG. 3.8 (a), the Fourier spectrum of the resistivity pattern as a function of l for a TDQDL shows a feature that is similar to the side-band formation. We highlight this aspect through an envelope function (dotted orange curve) over the actual result. For the same TDQDL, with a defect region at the centre, and for the same cut-off frequency, this side-band like feature becomes more prominent in FIG. 3.8 (b), whereas this side-band like feature gets highly suppressed in the case of moiré pattern of two relatively twisted TDQDls in FIG. 3.8 (c). These points out that certain angular frequency components get enhanced or suppressed as the scattering region is removed or added, a phenomenon akin to the spatial frequency filtering in Fourier optics, but now happening in the solid state environment for the angle-resolved resistivity, a transport coefficient. This can also be linked to the electronic analogue of Babinet's principle that we reported earlier in this manuscript. In the ballistic transport regime, the spatial frequency filtering in the angle resolved resistivity of MDFs scattered from TDQDL is shown as an electronic analogue of Babinet's principle. This forms one of the most prominent findings in this work.

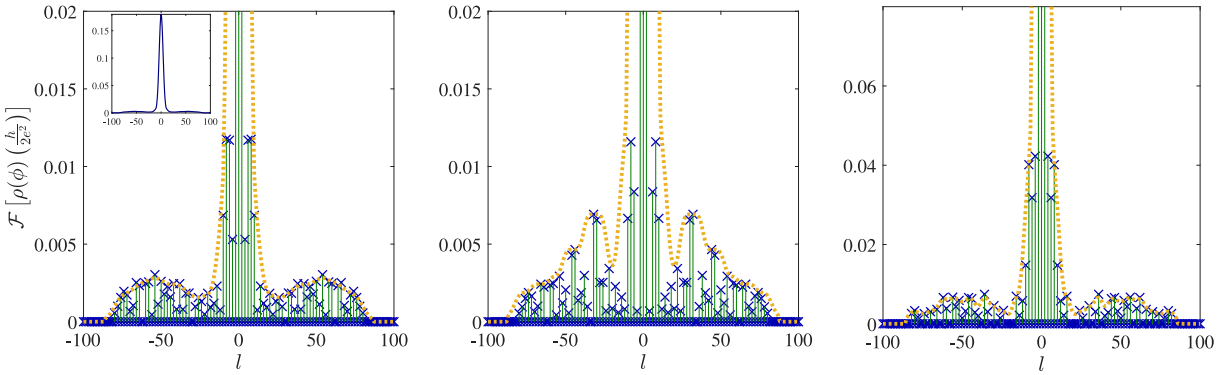

FIG. 3.8: (a) Shows the Fourier transform(FT) of the resistivity pattern for a TDQDL with $N_2 = 50$, $\Delta = 1$ and $d = 70$(nm). The blue cross ($\times$) denotes the value of amplitude corresponding to each spatial frequency (l). In the inset, we have shown the total data. The main figures do not show the central peak to display the smaller values. The FT of the resistivity pattern through a Gaussian filter for the same TDQDL scattering potential with a square defect region (in the centre) is shown in (b). In (c), we show the FT of the resistivity pattern through a Gaussian filter for a scattering potential made with a moiré pattern of two square TDQDL with the same lattice constant. This figure is taken from our published work [44].

3.2 Conclusion

To summarize, using the Lippmann-Schwinger formalism, we established an electronic analogue of Fourier optics i.e.,FEO by mapping the scattering cross-section of MDF from TDQDLs to the Fraunhauffer diffraction pattern and providing a dictionary of such mapping. By considering TDQDL with defect region and moiré pattern of such TDQDLs, we demonstrated an electronic analogue of Babinet's principle. Harnessing this analogy further with an eye on practical application, we evaluated the angle-resolved resistivity of these scattered MDs, and Fourier analyze the same to show that the Fourier spectrum shows spatial frequency filtering consistent with Babinet's principle. With the quantum dot arrays now routinely produced in semiconductor-based systems [136, 166, 167], we hope our proposed analogy can be used for making new electronic devices based on such analogue FEO.

CHAPTER 4

Magnetically modulated superconductor-graphene-superconductor (SGS) Josephson junctions and their tunability

This chapter is based on the published work - "*Magnetically modulated superconductor-graphene-superconductor (SGS) Josephson junctions and their tunability*", Partha Sarathi Banerjee, Rahul Marathe and Sankalpa Ghosh, *Phys. Scr.*, **100**, 015965.

4.1 Introduction

The dissipation-less super-current, namely the Josephson current (JC) that flows through Josephson junctions (JJ) [81, 82] played a significant role in quantum technologies such as superconducting qubit devices [32, 34, 168–170], sensing small magnetic fields [35, 171], parametric amplifiers [172, 173], single photon detection [174], etc., to name a few. The JC decreases with increasing temperature, which is the primary tuning parameter for such JJs for given materials, and vanishes at the critical temperature [175–177]. The JJs have been made with a thin insulating layer [178–180], metal [181–183], two-dimensional-electron-gas[184, 185], ferromagnet[186], and in recent times using mono and bilayer graphene where two closely spaced superconducting electrodes are placed on a graphene(G) sheet to make an SGS type [29, 43, 187–191] of JJ due to proximity induced superconductivity [30, 40, 41]. As first pointed out by Beenakker [83], compared to other weak links, the Josephson effect in SGS junctions can be attributed to both specular Andreev reflection (SAR) and conventional retro Andreev reflection (RAR) [183, 192], due to the peculiar quasiparticle dispersion in graphene [193–196]. Tunability of JC in such junctions using different means is therefore desirable for wider applicability of such devices.

In this chapter, we show that the temperature-dependent JC in such SGS junctions can be made more tunable for possible device applications by exposing the graphene region to a regularly spaced highly localised magnetic field typically dubbed in the literature as magnetic barriers [59, 61–63, 74, 197, 198]. In our proposed model, such SGS junctions are exposed

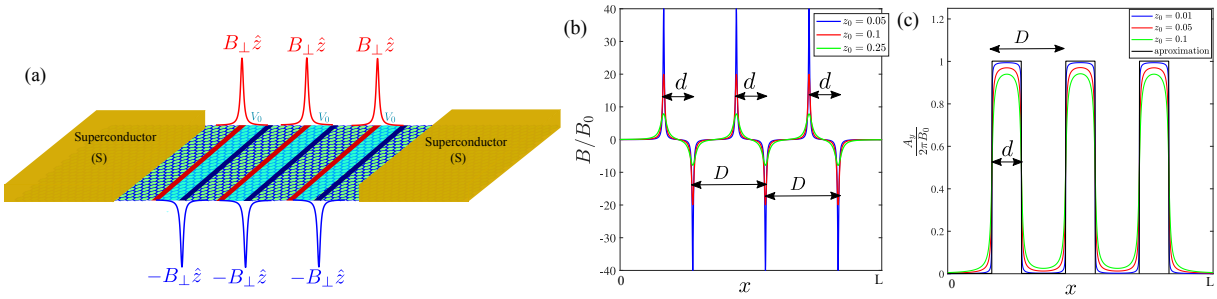

FIG. 4.1: In (a) the schematic depiction of the SGS type JJ with periodic electric and magnetic field. in the graphene region is shown. In the regions between the red and blue magnetic stripes a non zero electric field (V_0) is also considered. In (b) we compare the perpendicular magnetic field profile as seen by the massless Dirac fermions for different values of z_0. This can be done by changing the distance between the ferromagnetic stripe and the graphene sheet. The corresponding magnetic vector potential is shown in (c). As z_0 is reduced the magnetic field barriers become more close to a perfectly rectangular barrier. This figure is taken from our published work [45].

to magnetic barriers that can be created by putting a ferromagnetic stripe on top of the surface of graphene region [64, 65]. In experiments, such metallic stripes have been made by NdFeB [64], Co [65]. They emit a strong magnetic field to create this highly inhomogeneous magnetic field which breaks the time reversal symmetry in the graphene region explicitly. Using these stripes, a magnetic vector potential barrier can be created where two of such stripes produce a strong magnetic fields of equal magnitude, but in mutually opposite directions [66] which is transverse to the plane of the graphene layer as depicted in FIG. 4.1 (a). In graphene, using a fully scalable photolithographic process, Co based ferromagnetic layer has been deposited to make a magnetic tunnel junction [67–69, 80]. This makes the synthesis of such magnetically modulated SGS junctions a realistic possibility.

Because of the ultra-relativistic dispersion of the charge carriers in monolayer graphene, the strength of such magnetic barriers can be additionally tuned by an electrostatic barrier [11, 70, 71, 110]. These potential barriers can be created by putting a gate voltage to create a p-n junction in graphene [7, 20, 72]. Array of such barriers can be viewed as a realisation of magnetic Kronig-Penny model [62, 74, 198]. They consequently modify the band structure, thereby impacting Andreev reflection [192] in such relativistic Josephson junction. This, in turn, changes the JC flowing through such JJs. The combined electrostatic and magnetic barrier is schematically depicted in FIG. 4.1 (a).

JJs with high transition temperature (T_C) and higher superconducting energy gaps provide advantages for qubit applications involving graphene, as they are operable for higher tempera-

ture range. Superconductors with Al [199–201], W [40], Pt/Ta [202] and $Pb_{1-x}In_x$ [203] as superconducting electrodes has been used in experiments to make Josephson junctions. Keeping that in mind, in our calculations, we consider the superconducting gap for $Pb_{0.93}In_{0.07}$ electrode at 1.1 meV and the transition temperature at 7.0 K [203]. It may be noted that even though Pb ($T_C = 7.19$K) and In ($T_C = 3.4$K) are type-I superconductors, their alloy becomes a type-II superconductor. The transition temperature also depends on their composition [204].

In realistic graphene-based Josephson junctions, disorder arising from charged impurities, atomic vacancies, edge roughness, and substrate-induced potential fluctuations can induce intervalley scattering, suppress carrier mobility, and reduce phase coherence, thereby modifying the Andreev bound state spectrum and suppressing the critical Josephson current [205, 206]. Such disorder effects can be quantitatively understood using tight-binding Bogoliubov–de Gennes simulations, recursive Green's function methods, or self-consistent Born approximation techniques, which allow computation of disorder-averaged supercurrents and density of states in mesoscopic graphene systems [132, 207].

The rest of the chapter is organized as follows. The formalism and the DBdG equations in the three types of regions are discussed in Sec. 4.2. In Sec. 4.3, we discuss the solutions of the DBdG equation in three regions we are considering. In Sec. 4.4 we discuss the electronic analogue of the Snell's law in the magnetically modulated graphene region and their impact on the Andreev refelction. In Sec. 4.5 we calculate the transfer matrices from the boundary value conditions. The method to calculate the $\varepsilon - \phi$ relation for these systems is shown in Sec. 4.6. The Josephson current for both SAR and RAR regimes, and how the Josephson current can be modulated by the geometry and the magnetic barrier is discussed in Sec. 4.7. In Sec. 4.8, we summarize the results obtained in this chapter.

4.2 Superconductor-Graphene-Superconductor Junctions in the Presence of Electric and Magnetic Barrier in the Graphene Region

The system under consideration is a two-dimensional monolayer graphene (MLG) in the x-y plane, which is covered with a superconducting electrode in two regions ($x < 0$ and $x >$

L) (see FIG. 4.1 (a)). The regions under superconducting electrode become two-dimensional superconductors due to the proximity effect [41, 83, 188]. Due to the difference between the phases of the two superconductors (ϕ), a dissipation-less current flows in these systems which is periodic in ϕ [81]. The non-superconducting graphene region in between ($0 \leq x \leq L$), is exposed to ferromagnetic stripes with thickness d and height h, that are deposited on top of the two-dimensional graphene sheet with magnetization parallel [67] to the plane of the MLG.

If the graphene layer is situated at distance z_0 below the stripe then the magnetic field in the perpendicular direction can be written by [208] $B_z\hat{z} = \hat{z}K(x, z_0)$ where,

$$K(x, z_0) = B_0 \left[\frac{z_0 d}{x^2 + z_0^2} - \frac{z_0 d}{(x-d)^2 + z_0^2} \right] \tag{4.1}$$

The profile magnetic vector potential corresponding to this magnetic field takes form of a barrier, that shifts the momentum of the charge carriers. A series of N such magnetic vector potential barriers can be created, where the successive barriers are separated by a distance D. The resulting magnetic field becomes,

$$B_z\hat{z} = \hat{z} \sum_{m=0}^{N-1} K\left[x - (m+1)D + d, z_0\right]. \tag{4.2}$$

For N such barriers in graphene region with uniform spacing between them, $L = ND + (D - d)$, where both d and D (defined in the figure) varied in a given situation to achieve wider tunability. The magnetic field profile is shown in FIG. 4.1(b) and the corresponding magnetic vector potential in Landau gauge, $\mathbf{A} = \hat{y}A_y$ is shown in FIG. 4.1 (c). For a typical value of $B_0 = 0.1$ T [208–210], which depends on the magnetization(M_0), height (h) and thickness (d) of the stripe as $B_0 = M_0 h/d$, outside the magnetic barrier regime the magnetic field is several orders of magnitude less than the critical field of $Pb_{0.93}In_{0.07}$ electrode that we are considering [203]. A typical value for B_0 can be inferred from the fact that magnetic fields upto the order of $\approx$ 1T [80] has been used to create Co based magnetic tunnel junctions in graphene. In an experimental setup, the magnetic potential profile can be changed by changing the parameters z_0 and d as shown in FIG. 4.1 (b). Typically, the Fermi energy of pristine monolayer graphene is $\sim$ 27 meV [211], and the corresponding Fermi wavelength $\lambda_F \sim 152$ nm. This Fermi energy can further be shifted by doping [211, 212]. If $z_0 \ll \lambda_F$ in a typical experimental situation, the magnetic barrier is highly localised, and a $z_0 \to 0$ limit can be assumed to facilitate the

subsequent analysis. In the limit $z_0 \to 0$, the magnetic field profiles become delta functions, and the corresponding magnetic vector potentials approaches a perfect rectangular barrier. We perform our further calculation in this limit, and the approximated vector potentials are shown by the black curve in FIG. 4.1 (c).

To proceed further we write the magnetic vector potentials in Landau gauge as,

$$\mathbf{A}(x) = \begin{cases} \hat{y}Bl_m & \text{in the barrier region } (nD-d) < x < nD, \\ 0 & \text{in the G region } (n-1)D < x < (nD-d), \\ 0 & \text{in the S region } x < 0 \text{ and } x > L. \end{cases} \tag{4.3}$$

Here, $n = 1, 2, ...N$, $l_m = \sqrt{\frac{\hbar c}{eB}}$ is the magnetic length. As suggested in the introduction, for $0 \leq x \leq L$, we additionally consider a series of electrostatic potential barriers coupled with the magnetic barriers with the same width d and height $V (V > 0)$ [110]. These electrostatic potentials can be created by putting a series of electric gates [7, 11, 20, 70–72]. Such gate-defined electrostatic barriers have been experimentally demonstrated to create graphene p-n junctions in graphene [71, 72, 213]. In a realistic sample, for a finite distance between the graphene sample and the local gate (d_t), the edge of the barrier on both sides can be approximated as a linear function of width δ [214–216]. The electrostatic potential created by one such barrier of width d centred at $x = 0$ can be written as,

$$V(x) = \begin{cases} 0 & \text{at,} |x| > d + \delta, \\ \frac{V_0}{\delta}(d+\delta) - \frac{V_0}{\delta}x & \text{at,} d < x < d + \delta, \\ V_0 & \text{at,} |x| < d, \\ \frac{V_0}{\delta}x + \frac{V_0}{\delta}(d+\delta) & \text{at,} -d < x < -(d+\delta) \end{cases} \tag{4.4}$$

In a typical experimental setup, we generally have δ in the range of a few tens of nanometers and d is in the range of a few micrometres. This makes $\delta \ll d$ [215]. Also, the mean free path of the charge carriers of graphene is several micrometres [129, 193, 217]. Thus a leading approximation we can ignore terms dependent on δ/d, which gives us a rectangular scalar potential barrier. Further calculations are done in this limit. In FIG. 4.2, we show the scalar potentials created by three such electrostatic gate-defined scalar potential barriers for different values of

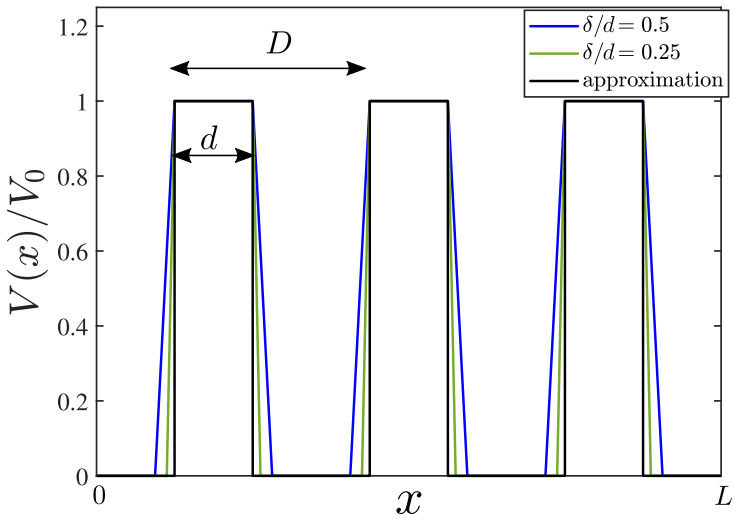

FIG. 4.2: In this figure, we show the scalar potential profile seen by the massless Dirac fermions in graphene created by electrostatic gate-defined potential barriers for different values of δ/d. This figure is taken from our published work [45].

δ/d. The black curve in FIG. 4.2 shows the approximation we have taken. An additional constant electrostatic potential $-U_0$, whose value can be adjusted by an external gate potential or by doping [83] in the superconducting region , is also introduced to offset the difference in electrostatic potential in the superconducting region and the graphene region. The resulting scalar electrostatic potential is given by

$$V(x) = \begin{cases} -U_0 & \text{in the S region } x < 0 \text{ and } x > L, \\ 0 & \text{in the G region } (n-1)D < x < (nD - d), \\ V & \text{in the barrier region } (nD - d) < x < nD. \end{cases} \tag{4.5}$$

The dynamics of charge carriers, namely the electron and hole excitations, in such SGS junction can be described by Dirac-Bogoliubov-De-Gennes (DBdG) equation [29, 83–86], and can be written as

$$\begin{bmatrix} \mathcal{H} - \mu & \Delta(T) \\ \Delta^*(T) & \mu - \mathcal{T}\mathcal{H}\mathcal{T}^{-1} \end{bmatrix} \begin{bmatrix} \Psi_e \\ \Psi_h \end{bmatrix} = \varepsilon \begin{bmatrix} \Psi_e \\ \Psi_h \end{bmatrix} \tag{4.6}$$

Here $\mathcal{H}$ is the (4×4) Dirac Hamiltonian for the charge carriers in graphene under effective mass approximation, namely massless Dirac fermions, in the presence of the electrostatic potential $V(x)$ and magnetic field $\mathbf{B}$, which acts on two sub-lattice and two valley degrees of freedom for such charge carriers. v_F is the Fermi velocity, $\Delta(T)$ is the temperature dependent superconducting pair potential which couples the time reversed electron and hole states. For our present

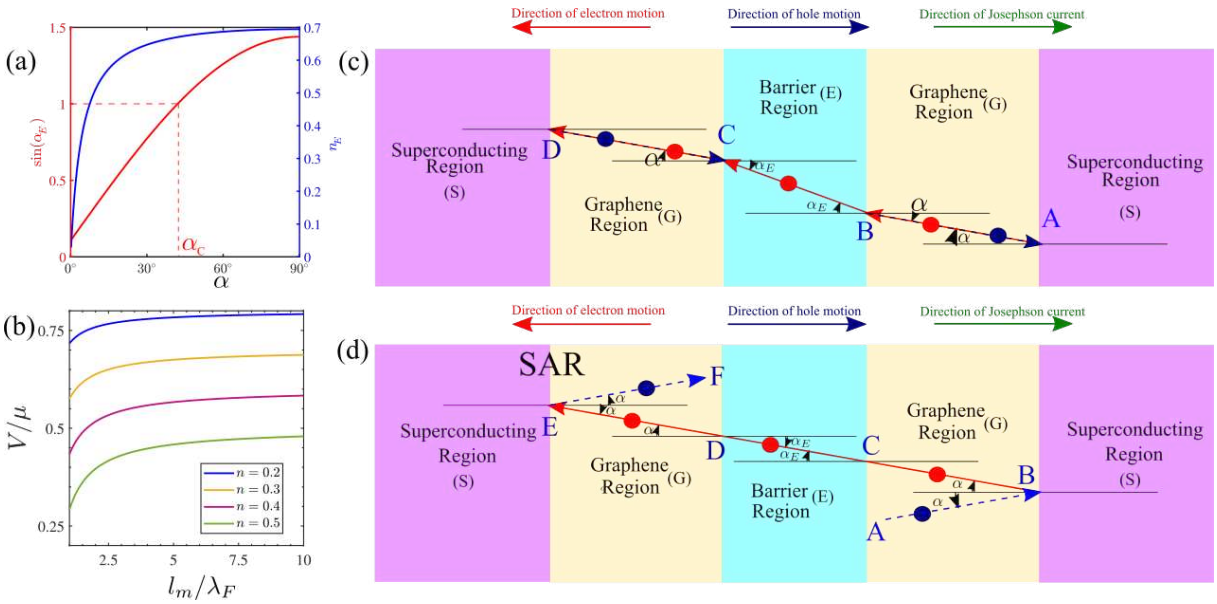

FIG. 4.3: In (a) we show the plot of $\sin(\alpha_E)$ calculated from the Snell's law in the RAR ($\mu \gg \varepsilon$) regime for as a function of α using the red curve. In the red curve we show the dependence of refractive index of the barrier region on α for a barrier with $\kappa_{lm} = 0.5$ and $\kappa_V = 0.25$. In (b), we have plotted the values of barrier potential (V) and magnetic length (l_m) which share the given values of refractive index (n_E) for $\alpha = \pi/8$. Here μ and λ_F is the Fermi energy and the Fermi wavelength of the barrier free region (G). In (c) we show the propagation of electron and hole for the same barrier in the RAR regime. In the schematic diagram, a hole following path BA undergoes RAR in the GS interface at point A. Due to RAR, a reflected electron traces back the path of the incident hole AB with $\alpha = 10^\circ$ and in the barrier region(E) acts as a medium with lighter refractive index (n_E) and the electron goes through BC path with $\alpha_E = 19.73^\circ$ and then again CD path through the G region with $\alpha_E = 10^\circ$. After that at point D, the electron undergoes RAR in the GS boundary and again reflects back as a hole. In (d), we show the schematic diagram for the propagation of electron and hole for the same barrier in the SAR regime. A hole from path AB with angle $\alpha' = 10^\circ$ undergoes SAR in the GS interface at B and reflects back as an electron with $\alpha = 10^\circ$. As the refractive index of the barrier region becomes $n_E \approx 1$ in the SAR regime, the reflected electron traces path BCDE and undergoes SAR and a reflected hole travels through EF direction. The blue solid circle denotes a hole and an electron is represented by a red solid circle. This figure is taken from our published work [45].

analysis, we consider s-wave pair potential such that

$$\Delta(T) = \begin{cases} \Delta_0(T)e^{i\phi_1} & \text{at, } x < 0 \\ 0 & \text{at, } 0 < x < L \\ \Delta_0(T)e^{i\phi_2} & \text{at, } x > L. \end{cases} \tag{4.7}$$

This can be generalised for more complicated pairing potential. The temperature dependence of such superconducting pair potential is given by [218],

$$\Delta_0(T) = \Delta_0(T=0)\sqrt{1-\left(\frac{T}{T_C}\right)^2}, \tag{4.8}$$

where critical temperature of a superconductor is given by T_C. $\mathcal{T}$ is the time-reversal operator and ε is the excitation energy measured relative to the Fermi energy μ. Ψ_e and Ψ_h represent the electron and hole excitations. The time-reversal operator which interchanges the valleys is given by [29, 83, 100],

$$\mathcal{T} = \begin{bmatrix} 0 & \sigma_z \\ \sigma_z & 0 \end{bmatrix} \mathcal{C} = \mathcal{T}^{-1}. \tag{4.9}$$

Here, $\mathcal{C}$ is the complex conjugation operator. As the pair-potential $\Delta(T)$ is same for both sub-lattice and valley degrees of freedom, in the presence of a magnetic field, it is more convenient to use a "valley-isotropic" basis for the Hamiltonian [86] by making a unitary transformation to both the Hamiltonian and the time-reversal operator $H = \mathcal{U}\mathcal{H}\mathcal{U}^\dagger$ and $T = \mathcal{U}\mathcal{T}\mathcal{U}^\dagger$ with $\mathcal{U} = \frac{1}{2}(\tau_0 + \tau_z) \otimes \sigma_0 + \frac{1}{2}(\tau_0 - \tau_z) \otimes \sigma_x$. σ_i and τ_i are the Pauli spin matrices which act on the sub-lattice and valley degrees of freedom respectively. Also, τ_0 and σ_0 represent 2×2 unit matrices. Upon these transformations the Hamiltonian now becomes,

$$\begin{aligned} H &= v_F \begin{bmatrix} \left[(\mathbf{p} + e\mathbf{A}) \cdot \boldsymbol{\sigma} + \frac{V(x)}{v_F}\right] & 0 \\ 0 & \left[(\mathbf{p} + e\mathbf{A}) \cdot \boldsymbol{\sigma} + \frac{V(x)}{v_F}\right] \end{bmatrix} \\ &= v_F \tau_0 \otimes \left[(\mathbf{p} + e\mathbf{A}) \cdot \boldsymbol{\sigma} + \frac{V(x)}{v_F}\right]. \end{aligned} \tag{4.10}$$

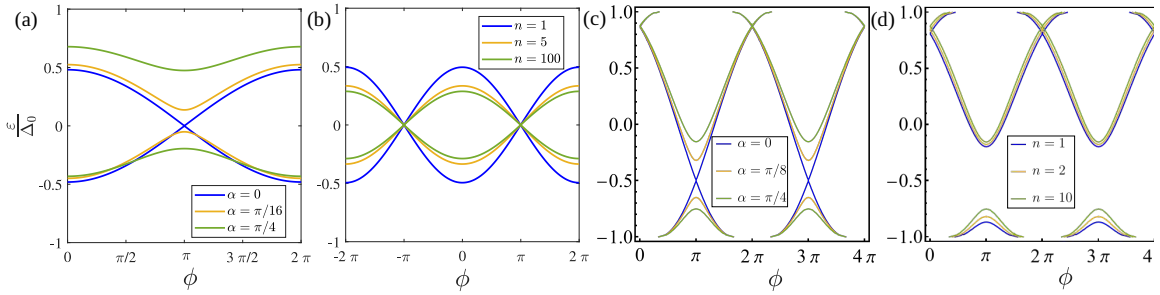

FIG. 4.4: The $\varepsilon - \phi$ relation for SG(EG)^{n}S for retro and specular Andreev reflection is shown in (a),(b) and (c),(d) respectively. In (a) we show the $\varepsilon - \phi$ relation for different values α for $\kappa = 1$, $\kappa_V = 0.5$, $n = 10$ and $\kappa_{lm} = 3$. In (b) the $\varepsilon - \phi$ relation is shown in case of RAR for different values of n and for $\kappa = 1$, $\kappa_V = 0.5$, $\kappa_{lm} = 3$ and $\alpha = \pi/4$. For the case of SAR, we show the $\varepsilon - \phi$ relation for different values of α in an SG(EG)^{n}S junction with κ=1, $\kappa_V = 0.5$, $\kappa_{lm} = 1$ and $n = 10$. $\varepsilon - \phi$ relation is plotted in (d) for the case of SAR for different values of n for $\kappa = 1$, $\kappa_V = 2$, $\kappa_{lm} = 2$ and $\alpha = \pi/4$. This figure is taken from our published work [45].

The time-reversal operator now becomes,

$$T = \begin{bmatrix} 0 & i\sigma_y \\ -i\sigma_y & 0 \end{bmatrix} \mathcal{C} = -(\tau_y \otimes \sigma_y)\mathcal{C}. \tag{4.11}$$

Using the Hamiltonian and the time-reversal operator from the Eq. (4.10) and (4.11) in the Dirac Bogoliubov De Gennes (DBdG) equation Eq. (4.6) in the presence of external potential $V(x)$ and magnetic vector potential $\mathbf{A}(x)$ as,

$$\begin{bmatrix} v_F\tau_0 \otimes \left[\boldsymbol{\pi}\cdot\boldsymbol{\sigma} + \frac{V(x)}{v_F} - \frac{\mu}{v_F}\right] & \Delta(T) \\ \Delta^*(T) & -v_F\tau_0 \otimes \left[\bar{\boldsymbol{\pi}}\cdot\boldsymbol{\sigma} + \frac{V(x)}{v_F} - \frac{\mu}{v_F}\right] \end{bmatrix} \begin{bmatrix} \Psi_e \\ \Psi_h \end{bmatrix} = \varepsilon \begin{bmatrix} \Psi_e \\ \Psi_h \end{bmatrix} \tag{4.12}$$

Where $\boldsymbol{\pi} = (\mathbf{p} + e\mathbf{A}(x))$ and $\bar{\boldsymbol{\pi}} = (\mathbf{p} - e\mathbf{A}(x))$. The scalar potential $V(x)$ does not invert the sign, but the magnetic vector potential $\mathbf{A}$ changes the sign under the time reversal operation [219]. We need the solutions for the DBdG equation in our system for energies below the superconducting gap ($\Delta_0(T)$) of the superconductor.

The Josephson current depends on the phase difference between the two superconducting regions ($\phi = \phi_2 - \phi_1$). Here if we define the electron and hole excitations Ψ_e and Ψ_h as, $\begin{bmatrix}\psi_{e1} & \psi_{e2} & \psi_{e3} & \psi_{e4}\end{bmatrix}^T$ and $\begin{bmatrix}\psi_{h1} & \psi_{h2} & \psi_{h3} & \psi_{h4}\end{bmatrix}^T$ then it is sufficient to calculate the solu-

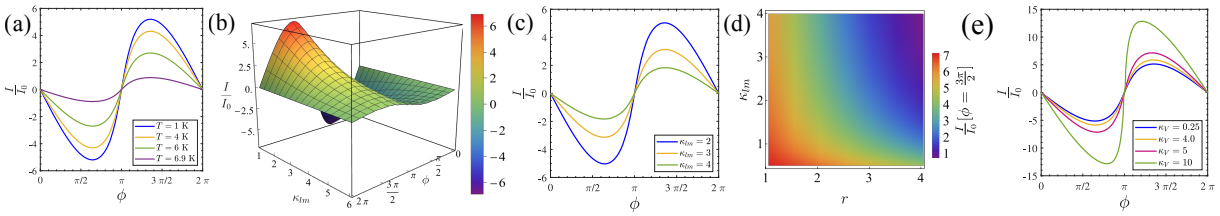

FIG. 4.5: In (a) we show the ϕ and T dependence of the Josephson current. For a constant temperature, the Josephson current is periodic in ϕ for an SG(EG)^{n}S type Josephson junction with $n = 10$ in the RAR regime. In this case, we have taken, $\kappa_{lm} = 2.0$ and $\kappa_V = 0.5$. In (b) we show the Josephson Current as a function of ϕ and the strength of magnetic barrier (κ_{lm}). We can observe from the 3D plot that for a constant value of ϕ, the Josephson current decreases with the increasing κ_{lm}. In (c) we show the cross-sectional plots to highlight this behaviour. In (d) we combine the effect of κ_{lm} and the ratio of size of EVMP regions and pure-graphene regions for an SG(EG)^{n}S type Josephson junction in the same RAR regime. In (b), (c) and (d), we have taken, $\kappa_V = 0.5$. In (e) we plot the Josephson current for different values of κ_V with ϕ for $\kappa_{lm} = 2.0$. In all these cases we have fixed $\kappa = 1$. This figure is taken from our published work [45].

tions of ψ_{e1}, ψ_{e2}, ψ_{h1} and ψ_{h2} from Eq. (4.6) because of the basis we have chosen. From these solutions, the full (8×1) wave function can be evaluated by

$$\Psi = \begin{bmatrix} \begin{pmatrix} C_{e1} \\ C_{e2} \end{pmatrix} \otimes \begin{pmatrix} \psi_{e1} \\ \psi_{e2} \end{pmatrix} \\ \begin{pmatrix} C_{h1} \\ C_{h2} \end{pmatrix} \otimes \begin{pmatrix} \psi_{h1} \\ \psi_{h2} \end{pmatrix} \end{bmatrix} \tag{4.13}$$

Now the (8×8) DBdG equation transforms into two equivalent four-dimensional DBdG equation,

$$\begin{bmatrix} V(x) - \mu & v_F(\pi_x - i\pi_y) & \Delta(T) & 0 \\ v_F(\pi_x + i\pi_y) & V(x) - \mu & 0 & \Delta(T) \\ \Delta^*(T) & 0 & \mu - V(x) & -v_F(\bar{\pi}_x - i\bar{\pi}_y) \\ 0 & \Delta^*(T) & -v_F(\bar{\pi}_x + i\bar{\pi}_y) & \mu - V(x) \end{bmatrix} \begin{bmatrix} \psi_{e1} \\ \psi_{e2} \\ \psi_{h1} \\ \psi_{h2} \end{bmatrix} = \varepsilon \begin{bmatrix} \psi_{e1} \\ \psi_{e2} \\ \psi_{h1} \\ \psi_{h2} \end{bmatrix} \tag{4.14}$$

4.3 Solutions of DBdG Equation

The wave-functions in the three types of region considered can be calculated for a given value of ε, q and ϕ from Eq. (4.14).

4.3.1 Superconducting Region

In the superconducting region, the DBdG equation from Eq. (4.14) is given by,

$$\begin{bmatrix} -\mu - U_0 & v_F(p_x - ip_y) & \Delta_0 e^{i\Phi} & 0 \\ v_F(p_x + ip_y) & -\mu - U_0 & 0 & \Delta_0 e^{i\Phi} \\ \Delta_0 e^{-i\Phi} & 0 & \mu + U_0 & -v_F(p_x - ip_y) \\ 0 & \Delta_0 e^{-i\Phi} & -v_F(p_x + ip_y) & \mu + U_0 \end{bmatrix} \begin{bmatrix} \psi_{e1} \\ \psi_{e2} \\ \psi_{h1} \\ \psi_{h2} \end{bmatrix} = \varepsilon \begin{bmatrix} \psi_{e1} \\ \psi_{e2} \\ \psi_{h1} \\ \psi_{h2} \end{bmatrix} \tag{4.15}$$

Here, Φ is the superconducting phase. The possible solutions in the regime of $U_0 + \mu \gg \Delta_0, \varepsilon$ are given by

$$\psi_1(\Phi) = e^{iqy + ik_o x - k_i x} \begin{pmatrix} e^{i\beta} \\ e^{i\beta + i\gamma} \\ e^{-i\Phi} \\ e^{-i\Phi + i\gamma} \end{pmatrix}, \tag{4.16a}$$

$$\psi_2(\Phi) = e^{iqy + ik_o x + k_i x} \begin{pmatrix} e^{-i\beta} \\ e^{-i\beta + i\gamma} \\ e^{-i\Phi} \\ e^{-i\Phi + i\gamma} \end{pmatrix}, \tag{4.16b}$$

$$\psi_3(\Phi) = e^{iqy - ik_o x - k_i x} \begin{pmatrix} e^{-i\beta} \\ -e^{-i\beta - i\gamma} \\ e^{-i\Phi} \\ -e^{-i\Phi - i\gamma} \end{pmatrix}, \tag{4.16c}$$

$$\psi_4(\Phi) = e^{iqy-ik_ox+k_ix}\begin{pmatrix} e^{i\beta} \\ -e^{i\beta-i\gamma} \\ e^{-i\Phi} \\ -e^{-i\Phi-i\gamma} \end{pmatrix}. \tag{4.16d}$$

where,

$$\beta = \begin{cases} \cos^{-1}\left(\frac{\varepsilon}{\Delta_o}\right) & \text{if } \varepsilon < \Delta_o \\ -i\cosh^{-1}\left(\frac{\varepsilon}{\Delta_o}\right) & \text{if } \varepsilon > \Delta_o \end{cases} \tag{4.17}$$

$$\gamma = \sin^{-1}\left[\frac{\hbar v_F q}{U_o+\mu}\right] \tag{4.18}$$

$$k_o = \sqrt{\left(\frac{U_o+\mu}{\hbar v_F}\right)^2 - q^2} \tag{4.19}$$

$$k_i = \frac{(U_o+\mu)\Delta_o}{\hbar^2 v_F^2 k_o}\sin\beta \tag{4.20}$$

In the regime of $|q| \leq \frac{\mu}{\hbar v_F}$ and if we take $U_o \gg \mu, \varepsilon$ then, $\gamma \to 0$, $k_o \to \frac{U_o}{\hbar v_F}$ and $k_i \to \frac{\Delta_o}{\hbar v_F}\sin\beta$. In the region $x < 0$, (i.e.,left superconductor), the wavefunction is $\Psi_l = a_1\psi_2(\phi_1) + a_2\psi_4(\phi_1)$. In the region $x > L$, (i.e.,right superconductor) the wave-function is $\Psi_r = b_1\psi_1(\phi_2) + b_2\psi_3(\phi_2)$.

4.3.2 Outside the EMVP Barrier

Outside the EMVP barrier in the graphene region, the wave-functions are given by,

$$\psi^{\mathbf{e}+} = \frac{e^{iqy+ikx}}{\sqrt{\cos\alpha}}\begin{pmatrix} e^{-\frac{i\alpha}{2}} \\ e^{\frac{i\alpha}{2}} \\ 0 \\ 0 \end{pmatrix}, \tag{4.21a}$$

$$\psi^{\mathbf{e}-} = \frac{e^{iqy-ikx}}{\sqrt{\cos\alpha}} \begin{pmatrix} e^{\frac{i\alpha}{2}} \\ -e^{-\frac{i\alpha}{2}} \\ 0 \\ 0 \end{pmatrix}, \tag{4.21b}$$

$$\psi^{\mathbf{h}+} = \frac{e^{iqy+ik'x}}{\sqrt{\cos\alpha'}} \begin{pmatrix} 0 \\ 0 \\ e^{-\frac{i\alpha'}{2}} \\ -e^{\frac{i\alpha'}{2}} \end{pmatrix}, \tag{4.21c}$$

$$\psi^{\mathbf{h}-} = \frac{e^{iqy-ik'x}}{\sqrt{\cos\alpha'}} \begin{pmatrix} 0 \\ 0 \\ e^{\frac{i\alpha'}{2}} \\ e^{-\frac{i\alpha'}{2}} \end{pmatrix}. \tag{4.21d}$$

Where,

$$\alpha \quad = \text{angle of incidence of electron} = \quad \sin^{-1}\left[\frac{\hbar v_F q}{\varepsilon+\mu}\right],$$

$$\alpha' \quad = \text{angle of reflection of hole} = \quad \sin^{-1}\left[\frac{\hbar v_F q}{\varepsilon-\mu}\right],$$

$$q \quad = \text{transverse wave vector in this region,}$$

$$k \quad = \text{longitudinal wave vector of electron} = \quad \left(\frac{\varepsilon+\mu}{\hbar v_F}\right)\cos\alpha\,,$$

$$k' \quad = \text{longitudinal wave vector of hole} = \quad \left(\frac{\varepsilon-\mu}{\hbar v_F}\right)\cos\alpha'\,.$$

The wavefunction in this region is a linear superposition of all four basis states in Eq. (4.21)

4.3.3 Inside the EMVP barrier

Inside the EMVP barrier in the graphene region, the wave-functions are given by,

$$\psi_{\mathbf{E}}^{\mathbf{e}+} = \frac{e^{iqy+ik_E x}}{\sqrt{\cos\alpha_E}} \begin{pmatrix} e^{-\frac{i\alpha_E}{2}} \\ e^{\frac{i\alpha_E}{2}} \\ 0 \\ 0 \end{pmatrix}, \tag{4.22a}$$

$$\psi_{\mathbf{E}}^{\mathbf{e}-} = \frac{e^{iqy-ik_E x}}{\sqrt{\cos\alpha_E}} \begin{pmatrix} e^{\frac{i\alpha_E}{2}} \\ -e^{-\frac{i\alpha_E}{2}} \\ 0 \\ 0 \end{pmatrix}, \tag{4.22b}$$

$$\psi_{\mathbf{E}}^{\mathbf{h}+} = \frac{e^{iqy+ik'_E x}}{\sqrt{\cos\alpha'_E}} \begin{pmatrix} 0 \\ 0 \\ e^{-\frac{i\alpha'_E}{2}} \\ -e^{\frac{i\alpha'_E}{2}} \end{pmatrix}, \tag{4.22c}$$

$$\psi_{\mathbf{E}}^{\mathbf{h}-} = \frac{e^{iqy-ik'_E x}}{\sqrt{\cos\alpha'_E}} \begin{pmatrix} 0 \\ 0 \\ e^{\frac{i\alpha'_E}{2}} \\ e^{-\frac{i\alpha'_E}{2}} \end{pmatrix}. \tag{4.22d}$$

Here,

$$\sin(\alpha_E) = \left(\frac{\hbar v_F \left(q + \frac{1}{l_m} \right)}{\varepsilon - V + \mu} \right) \tag{4.23a}$$

$$\cos(\alpha_E) = \left(\frac{\hbar v_F k_E}{\varepsilon - V + \mu} \right) \tag{4.23b}$$

$$\sin(\alpha'_E) = \left(\frac{\hbar v_F \left(q - \frac{1}{l_m} \right)}{\varepsilon - \mu + V} \right) \tag{4.23c}$$

$$\cos(\alpha'_E) = \left(\frac{\hbar v_F k'_E}{\varepsilon - \mu + V} \right) \tag{4.23d}$$

Here also the wave-function in this region is a linear superposition of all four basis states in

Eq. (4.22).

4.4 Snell's law

The two superconductors at the two ends of our system acts as Andreev reflectors for the graphene electrons as depicted in FIG. 4.3 (b) and (c). When an electron encounters the graphene (G)- superconductor(S) interface, it is reflected as a hole and a hole is reflected as an electron [83, 101]. Between these two reflectors, the barriers (E) in the graphene region now act as mediums with modulated refractive index.

The solutions of the DBdG equation in all the regions is discussed in detail in Sec. 4.3. Using the properties of these wavefunctions, we can get Snell's law for graphene electrons propagating from the free region to the barrier region. The direction of the propagation of electron and the hole can be obtained from their respective wavefunctions. If the angle of propagation of graphene electron with respect to normal direction in free region and the barrier region is α and α_E respectively, then for the case of RAR ($\mu \gg \varepsilon$), the electronic analogue of the refractive index in the G region that captures the effect of the barriers in this region can be gives as

$$n_E = \frac{\sin(\alpha)}{\sin(\alpha_E)} = \frac{\left(1 - \frac{V}{\mu}\right) k_F l_m \sin(\alpha)}{1 + k_F l_m \sin(\alpha)}. \tag{4.24}$$

In FIG. 4.3(a) we have shown the value of $\sin(\alpha_E)$ calculated from the Snell's law defined in Eq. (4.24).

For the case of RAR, the critical angle of incidence for graphene electron is,

$$\alpha_C = \sin^{-1}\left(1 - \frac{V}{\mu} - \frac{1}{k_F l_m}\right). \tag{4.25}$$

Beyond the critical angle of incidence the propagating solution representing scattering states in the G region become evanescent waves (bound states). Their hybridization with the Andreev bound states may lead to interesting features somewhat akin to the one studied in electron transport in SGS type of JJs in the presence of uniform magnetic to detect the valley polarisation of edge states produced in the graphene region[86]. We shall not discuss this issue any further in the current work and will shelve it for future work. Eq. (4.24) that gives the electronics

analogue of Snell's law shows that different values of electrostatic barrier potential (V) and magnetic length (l_m) can give the same refractive index (n_E) for a given angle of propagation α. which can be expressed as

$$V_2 = \mu \left[1 + \left(\frac{V_1}{\mu} - 1\right)\right] \left(\frac{l_{m1}}{l_{m2}}\right) \left[\frac{1 + k_F l_{m2} \sin\alpha}{1 + k_F l_{m1} \sin\alpha}\right]. \tag{4.26}$$

To elucidate this issue further in FIG. 4.3 (b), we have plotted the values of barrier potential (V) and magnetic length (l_m) with which a given refractive index (n_E) can be achieved for a given angle of propagation (α). The interconvertibility between the electric and magnetic field as they are applied to charge carriers in graphene that are massless Dirac fermions was studied extensively in various contexts in a number of earlier works [110, 220, 221]. In the current work we demonstrate its implication for JC through SGS junctions.

In FIG. 4.3 (c) we have depicted a schematic diagram of motion of electron and hole in the RAR regime. In case of RAR, the reflected electron/hole traces back the path of incident hole/electron. The E region in this figure is the barrier region. It acts as a rarer medium compared to the G region for all possible angles of α as shown in FIG. 4.3 (a). However, for the case of SAR ($\mu \ll \varepsilon$), we have,

$$n_E = \frac{\sin(\alpha)}{\sin(\alpha_E)} \approx 1. \tag{4.27}$$

After traveling through the barrier region with $\alpha < \alpha_C$, the charge carriers in graphene again moves with the same angle of propagation α. The propagation of electrons and holes in the SAR regime is schematically depicted in FIG. 4.3 (d). In this case, the angle of reflection in the GS interface is same as angle of incidence, as happens in specular optical reflection. Again, when the graphene electron encounters the superconducting surface, only the electrons with angle of propagation(α) less than $\alpha_A = \sin^{-1}(|\varepsilon - \mu|/\varepsilon + \mu)$ undergoes Andreev reflection [83].

4.5 Wavefunctions and boundary value conditions

From the DBdG equation Eq. (4.14), we get four plane wave solutions for all the three types of regions, i.e.,superconducting region, graphene region both outside and inside the barrier regime. In Eq. (4.14) let us define $u = \begin{bmatrix}\psi_{e1} & \psi_{e2}\end{bmatrix}^T$ and $v = \begin{bmatrix}\psi_{h1} & \psi_{h2}\end{bmatrix}^T$. The solutions of the DBdG

equation for a given value of ε and q are shown in Sec. 4.3. Using the wave functions we can evaluate some boundary value conditions to make transfer matrices in this system. As we are considering the Andreev bound state spectrum i.e.,$\varepsilon < \Delta_0(T)$ at the GS interface, the electron and hole part of the wave-function of DBdG equation Eq. (4.14) is related by [29]

$$v(x=0) = e^{-i\phi_1 + i\beta\sigma_x} u(x=0) \tag{4.28a}$$

$$u(x=L) = e^{i\phi_2 + i\beta\sigma_x} v(x=L) \tag{4.28b}$$

where $e^{i\beta\sigma_x} = \begin{bmatrix} \cos(\beta) & i\sin(\beta) \\ i\sin(\beta) & \cos(\beta) \end{bmatrix}$ and $\phi_{1,2}$ are the phases of superconductors. β in this case is defined by $\cos\beta = \varepsilon/\Delta_0(T)$ and the range of β is $\left(-\frac{\pi}{2}, \frac{\pi}{2}\right)$.

In the graphene region outside each barrier, the two ends of the region (i.e.,$x = (n-1)D$ and $x = nD - d$) are related by [29],

$$v\left[x = (n-1)D\right] = M_2\left(\varepsilon, q\right) v\left[x = nD - d\right] \tag{4.29a}$$

$$u\left[x = nD - d\right] = M_1\left(\varepsilon, q\right) u\left[x = (n-1)D\right] \tag{4.29b}$$

Here, $M_1\left(\varepsilon, q\right) = \Lambda_1 e^{-ik(D-d)\sigma_z}\Lambda_1$ and $M_2\left(\varepsilon, q\right) = \Lambda_2 e^{-ik'(D-d)\sigma_z}\Lambda_2$. Also, k and k' is the wave vector in x direction i.e.,the longitudinal wave vector for electron and hole excitations respectively, Λ_1 and Λ_2 are (2×2) matrices given by:

$$\Lambda_1 = \Lambda_1^{-1} = \frac{1}{\sqrt{2\cos\alpha}} \begin{bmatrix} e^{-i\alpha/2} & e^{i\alpha/2} \\ e^{i\alpha/2} & -e^{-i\alpha/2} \end{bmatrix} \tag{4.30a}$$

$$\Lambda_2 = \Lambda_2^{-1} = \frac{1}{\sqrt{2\cos\alpha}} \begin{bmatrix} e^{i\alpha'/2} & e^{-i\alpha'/2} \\ e^{-i\alpha'/2} & -e^{i\alpha'/2} \end{bmatrix} \tag{4.30b}$$

$$\text{with}, \sin(\alpha) = \frac{\hbar v_F q}{\varepsilon + \mu}, \qquad \sin(\alpha') = \frac{\hbar v_F q}{\varepsilon - \mu} \tag{4.30c}$$

The angle α, α' $\left(0, \frac{\pi}{2}\right)$ are the angles of incidence and reflection of the electrons and holes respectively in the NS interface. Contrary to an SGS junction in the absence of any magnetic

barrier[29], in our case due to the presence of non-zero magnetic vector potential in the barrier region (E), the parallel component of the wave vector changes when it comes from the barrier-free region (G). In Eq. (4.22) in Sec. 4.3, we show the wavefunctions in the barrier region. By comparing the wavefunctions at the two ends of n'th barrier ($x = nD - d$ and $x = nD$) we show that they are related by

$$v(x = nD - d) = M_{2E}(\varepsilon, q)\, v(x = nD) \tag{4.31a}$$

$$u(x = nD) = M_{1E}(\varepsilon, q)\, u(x = nD - d) \tag{4.31b}$$

Here $M_{1E}(\varepsilon, q) = \Lambda_{1E} e^{-ik_E d\sigma_z} \Lambda_{1E}$ and $M_{2E}(\varepsilon, q) = \Lambda_{2E} e^{-ik'_E d\sigma_z} \Lambda_{2E}$. Also, k_E and k'_E are the wave vectors in the x direction for electron and hole excitations inside the barrier, and Λ_{1E} and Λ_{2E} are (2×2) matrices.

$$\Lambda_{1E} = \Lambda_{1E}^{-1} = \frac{1}{\sqrt{2\cos\alpha_E}} \begin{bmatrix} e^{-i\alpha_E/2} & e^{i\alpha_E/2} \\ e^{i\alpha_E/2} & -e^{-i\alpha_E/2} \end{bmatrix} \tag{4.32a}$$

$$\Lambda_{2E} = \Lambda_{2E}^{-1} = \frac{1}{\sqrt{2\cos\alpha'_E}} \begin{bmatrix} e^{i\alpha'_E/2} & e^{-i\alpha'_E/2} \\ e^{-i\alpha'_E/2} & -e^{i\alpha'_E/2} \end{bmatrix} \tag{4.32b}$$

$$\sin(\alpha_E) = \left(\frac{\hbar v_F \left(q + \frac{1}{l_m} \right)}{\varepsilon - V + \mu} \right), \quad \sin(\alpha'_E) = \left(\frac{\hbar v_F \left(q - \frac{1}{l_m} \right)}{\varepsilon - \mu + V} \right) \tag{4.32c}$$

By comparing the angles α and α_E from Eq. (4.30) (c) and Eq. (4.32) (c) we observe that q is replaced by $q \pm 1/l_m$ for electrons and holes respectively.

4.6 Dispersion $(\varepsilon - \phi)$relation

Let us consider n electrostatic and magnetic vector potential (EMVP) barriers of width d in the graphene region of the SGS junction separated by a distance D such that $L = ND + (D - d)$. The condition for a bound state in this system is that the transfer matrix for a round trip from $x = 0$ to $x = L$ and again from $x = L$ to $x = 0$ to be a unit matrix of dimension (2×2) [29]. Using Eq. (4.28a), (4.35) and (4.31) it can be shown that this condition results in,

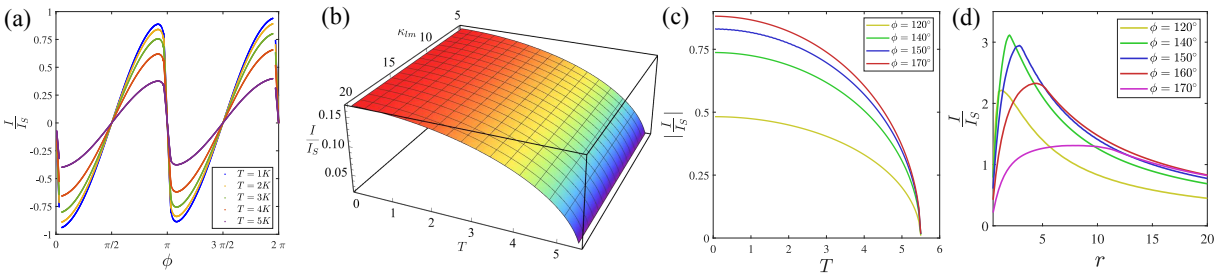

FIG. 4.6: In (a) the Josephson Current is plotted with its dependence on ϕ for an SG(EG)^{n}S type Josephson junction with $n = 10$ in the SAR regime for different values of temperature while keeping $\kappa_{lm} = 10$ and $\kappa_V = 2$. In (b) we show the Josephson current for different values of κ_{lm} and temperature (T) for $\phi = 2\pi/3$ and $\kappa_V = 2$. We can observe that as we are in the short junction limit, the κ_{lm} does not impact the Josephson current. In (c) we show the temperature dependence of the Josephson current in the SAR regime for different values of ϕ for $\kappa_V = 2$ and $\kappa_{lm} = 10$. In (d) the Josephson current is plotted with r for different values of ϕ again for the SAR regime while keeping $\kappa_{lm} = 10$ and $\kappa_V = 2$. In all these cases we have taken κ=1 . This figure is taken from our published work [45].

$$Det\left[\mathbb{I}_2 - e^{i\phi}T(\varepsilon, q)\right] = 0 \tag{4.33a}$$

$$T(\varepsilon, q) = M_1(\varepsilon, q)\left[M_{1E}(\varepsilon, q)M_1(\varepsilon, q)\right]^n e^{i\beta\sigma_x}\left[M_2(\varepsilon, q)M_{2E}(\varepsilon, q)\right]^n M_2(\varepsilon, q)e^{i\beta\sigma_x} \tag{4.33b}$$

This equation can be solved for any value of ε, q and ϕ. The $\varepsilon - \phi$ relation calculated from Eq. (4.33a) can be written as an equation for a conic section [222] for a fixed value of ϕ,

$$A - By^2 + Cxy + \cos(\phi) = 0 \tag{4.34}$$

where A, B, C and D are constants which depend on the parameters defining and characterising the barrier regime (such as $\kappa_V = \frac{V}{\mu}$, $\kappa_{lm} = \frac{\lambda_F}{l_m}$, $\kappa = \frac{\mu d}{\hbar v_F}$ and the angles α and α'), $x = \sin(\varepsilon/\Delta_0)$ and $y = \cos(\varepsilon/\Delta_0)$. Here λ_F is the Fermi wavelength in the barrier free graphene region (G) of our system. From Eq. (4.34), we can numerically evaluate $\varepsilon/\Delta_0(T)$ as a function of ϕ to write as

$$\frac{\varepsilon_n}{\Delta_0(T)} = g_n(\phi, \kappa, \kappa_V, \kappa_{lm}, \alpha, \alpha'). \tag{4.35}$$

Here, $g_n(\phi, \kappa, \kappa_V, \kappa_{lm}, \alpha, \alpha')$ is numerically as the nth solution of Eq. (4.33a) and Eq. (4.33b) for given values of ϕ, κ, κ_V, κ_{lm}, α and α'. There are two regimes of energy which are inter-

esting to study, retro Andreev reflection (RAR) and specular Andreev reflection (SAR). RAR dominates in the superconductor-graphene junctions when $\mu \gg \Delta_0(T)$[83]. From Eq. (4.30c), we can see that in this regime $\alpha' = -\alpha$. In the regime of $\mu \ll \Delta_0(T)$, the SAR dominates. From Eq. (4.30c), we can show that in the SAR regime $\alpha' = \alpha$. In FIG. 4.4 (a) and (b) we show the $\varepsilon - \phi$ relation for the RAR regime and in (c) and (d) we show the $\varepsilon - \phi$ relation for the SAR regime. As a prototype case, for 10 such barriers inside the graphene region of the SGS junction, we can observe that the ϕ dependence on ε for $\alpha \neq 0$, is asymmetric with respect to $\varepsilon = 0$ in our system. This is not the case in normal SGS junctions. For $\alpha \neq 0$, the gap opens at $\phi = 0$. In (b) we show the dependence of the $\varepsilon - \phi$ relation on the number of barriers we have considered in the graphene region. As we increase the number of barriers, the two values of energy for a fixed value of ϕ come closer. As the number of barriers increases, multiple scattering reduces the effective transparency and quasiparticles undergo multiple refraction, thereby suppressing the Andreev bound state energies and lowering the overall energy scale of the system. In (c) we show the $\varepsilon - \phi$ relation for the SAR regime. Again, similar to RAR we can see for $\alpha = 0$ the gap closes. Again in (d) we show the dependence of the number of barriers for the $\varepsilon - \phi$ relation in the SAR regime. As we see in the next section 4.7, this change in the dispersion strongly influences the Josephson current in the presence of such barriers and provides us a way to tune the junction properties.

4.7 Josephson Current

Josephson current I across this junction at a temperature T is given by [29, 85, 182, 223]

$$I(\phi, T) = \frac{4e}{\hbar} \sum_{n} \sum_{q=-k_F}^{k_F} \left(\frac{\partial \varepsilon_n}{\partial \phi} \right) f(\varepsilon_n), \tag{4.36}$$

where $f(\varepsilon_n)$ is the Fermi distribution function given by $f(\varepsilon_n) = 1/\left[\exp\{\varepsilon_n / k_B T\} + 1\right]$ and k_B is the Boltzmann constant. The partial differential term in Eq. (4.36) is calculated from Eq. (4.35) as,

$$\left(\frac{\partial \varepsilon_n}{\partial \phi}\right) = \left[\Delta_0(T=0)\sqrt{1-\left(\frac{T}{T_C}\right)^2}\right]\frac{\partial g_n}{\partial \phi} \tag{4.37}$$

From Eq. (4.37), we can see that the temperature dependence of the current is dominated by the $\sqrt{1-(T/T_C)^2}$ term. This makes the critical value of the periodic (in ϕ) Josephson current decrease with temperature. And at $T = T_C$, as the superconductivity is destroyed, we can also see that the Josephson current also becomes zero. In FIG. 4.5 (a) we plot the Josephson current as a function of ϕ for different temperatures in the RAR regime. As predicted earlier, we see that for higher values of temperature, the Josephson current is reduced in this regime. In (b) and (c), we show the effect of strength of magnetic barrier on the Josephson current using a 3D plot and 2D plot respectively in the RAR regime. The magnetic barrier has a pronounced effect on the magnitude of the Josephson current. We define the ratio of the length of barrier region (E) and the barrier free graphene region (G) as r. By combining the effect both this ratio r and the strength of the magnetic field (κ_{lm}) we show in (d) how the Josephson current can be tuned. In (e) we show the effect of κ_V, which denotes the strength of the electrostatic scalar potential, on the Josephson current. Here, $I_0 = \frac{8ek_F\Delta_0(T=0)}{\hbar}$ and for demonstrative purpose in all of these cases, we have considered 10 EMVP barriers inside the graphene region of the SGS junction.

For the SAR regime, we show the Josephson current in FIG. 4.6 (a) for different temperatures. As discussed earlier, in SAR regime also, the Josephson current reduces with increasing temperature. In (c) we show the temperature dependence of the Josephson current for different values of ϕ. We can see that because of the $\sqrt{1-(T/T_C)^2}$ term, the Josephson current decreases with temperature and goes to zero at the critical temperature. In the short junction limit, the SAR current does not depend on the strength of the magnetic barrier (κ_{lm}), unlike the RAR case which is shown in (b). This happens because the transfer matrices M_{1E} and M_{2E} in Eq. (4.33a) become unit matrices in this limit. Also, we can observe from the Snell's law in the SAR regime Eq. (4.27) that the refractive index of the barriers approaches unit value in the SAR regime, thereby making the magnetic barrier transparent to the Josephson current in the SAR regime.

The thermal fluctuations in such JJs can be studied in the framework of the Stewart-McCumber or Resistively and Capacitively Shunted Junction(RCSJ) [224, 225] model. The thermal fluctuations become very important in the case of the ac-Josephson effect. In the RCSJ model, the resistance accounts for the dissipative processes, and the capacitor represents the junction's

capacitance. The Josephson junction is modelled with a parallel combination of the resistance and capacitor. At finite temperatures, thermal fluctuations can cause premature switching from the superconducting state to the resistive state. In our present analysis, we do not consider the effects of thermal fluctuation, which gives a good approximation for lower temperatures where thermal energy is significantly smaller than the Josephson energy [226]. Also in our current study, we did not consider any effect of impurity and defects in graphene. Impurities or doping can make local p or n-type regions [227] in graphene which could create additional scattering centers and potentially reduce the Josephson current. The vacancy-type defects in graphene can also decrease the Josephson current by reducing carrier mobility [228, 229].

The temperature dependence of the critical current has been observed in various graphene-based SGS-type Josephson junctions [230, 231]. We have shown using our theoretical analysis that in the presence of the electrostatic and magnetic barriers, similar temperature dependence will still be observed with our model. However, the presence of barriers gives extra control of the Josephson current in the RAR regime as shown in FIG. 4.5. This happens due to the change of wave vector following Snell's law given in Eq. (4.24). Experimentally the potential barriers in graphene have been demonstrated [11, 71, 213] to study the scattering of charge carriers of graphene and its impact on electron transport. On the other hand, using a fully scalable photolithographic process, the tunnel junctions in graphene have been experimentally realized by depositing Co based ferromagnetic layers [67–69, 80]. We hope the present study can guide us to combine these two to create the possibility of new device applications with the help of proximity-induced graphene-based Josephson Junctions [199, 200, 232, 233].

4.8 Conclusion

To conclude we have shown that the Josephson current in a SGS junction can be significantly tuned by magnetically modulate the graphene regime. Additionally the strength of this magnetic barrier can be tuned by introducing gate voltage. This combination thus provides an important tuning parameter to control Josephson current through such junctions and indicates possibility of interesting device applicability. Following the work on electron transport in SGS type of JJs in the presence of uniform magnetic field that shows hybridisation of edge states in the graphene region with andreev bound state [86], superposition of the uniform magnetic field and

the magnetic barrier in the graphene region [234] are expected to show rich physics with wider possibility of device application. This could be an interesting topic for future research in this direction.

CHAPTER 5

Intermediate chiral edge states in quantum Hall Josephson junctions

This chapter is based on the published work - "*Intermediate chiral edge states in quantum Hall Josephson junctions*", Partha Sarathi Banerjee, Rahul Marathe and Sankalpa Ghosh, arXiv: 2510.11432.

5.1 Introduction

In superconductor-quantum Hall-superconductor (SQHS) Jospehson junctions (JJ) [235, 236], the Josephson effect occurs due to Andreev reflection in high magnetic fields [75, 237–240] at SN interface. This was further experimentally explored in graphene [86, 241], graphene nano-ribbons [242] and other topological materials [243], chiral Andreev edge states in twisted graphene bilayer and hBN encapsulated graphene [244, 245]. S–quantum Hall junctions are realized by contacting a high-mobility 2D system in the quantum Hall regime (e.g., graphene) with a thin, high–critical-field superconductor (such as NbN or MoRe) that remains superconducting at several tesla [246, 247]. Transparent edge contacts enable proximity coupling to chiral edge states, allowing supercurrent and Andreev processes to be observed in the quantum Hall regime [246, 247]. We show that local potentials in quantum Hall regime that can induce ICES (classically skipping orbits in the N region than at the Superconductor-quantum Hall (SQH) boundaries) at the electrostatic boundaries [77, 78] that can significantly impact and alter the Josepshson conductivity through such junctions.

In experimental systems disorder can play a role by introducing random local potential fluctuations in the normal (quantum Hall) region, which can scatter and mix the chiral edge states and thereby modify the Landau level structure and the Josephson conductivity [77].

The current work achieves two distinct results: a. A theoretical framework is developed to calculate and understand this variation of conductance in ballistic regime due to induction of ICES. This uses transfer matrices derived within BTK [79] and subsequently conductivity is

calculated using Landauer-Buttiker formula. b. The formalism is subsequently extended to a periodically modulated SQHS JJ where a periodic potential is applied to the N regions along with the transverse magnetic field. Given the experimental demonstration of band conductance oscillation in graphene superlattice [248, 249], spectroscopy of fractal Hofstatder spectrum [250] in recent work, our theoretical framework can be used to understand the impact of ICES in junctions made with such lattice QH systems.

5.2 BdG equation for the S, B and N regions

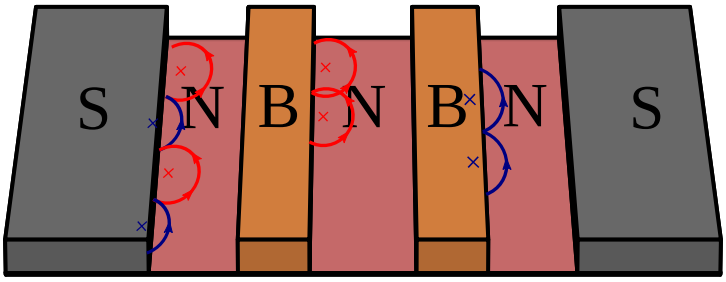

FIG. 5.1: Schematic diagram of SNBNS junction we are considering here. The red semicircles represent the classical electron orbits and the blue semicircles represent the classical hole orbits.

We begin by considering a case where a finite number of identical rectangular potential barriers with an uniform spacing between two consecutive barriers, in the N region of length $2L$ that is also exposed to a strong transverse magnetic field $B\hat{z}$, in an SNS junction. The schematic diagram of the system is shown in FIG. 5.1 . The imperfections in the SN and NS interfaces are quantified with two delta function potentials $U_1\delta(x-L)$ and $U_2\delta(x+L)$. The S region is defined as $|x| > L$ in the unit of magnetic length $l = \sqrt{\hbar/|eB|} = 25.6/\sqrt{B}$ nm with B in Tesla, and energies are in the units of $\hbar\omega_C$. For, $V(x) = \hbar\omega_C U(x)$, the BDG equation that models different parts of the system in BTK formalism can be written as,

$$\begin{bmatrix} H_0(x,X)-\mu & \Delta \\ \Delta^* & \mu - H_0(x,-X) \end{bmatrix} \begin{bmatrix} f_X \\ g_X \end{bmatrix} = E \begin{bmatrix} f_X \\ g_X \end{bmatrix} \tag{5.1}$$

Here X is the guiding centre of electrons. For an uniform magnetic field $\mathbf{B} = B\hat{z}$, in Landau gauge the vector potential becomes, $\mathbb{A} = xB\hat{y}$ in the N and B region and 0 in the S region. We define, $\nu = 2\mu/\hbar\omega_C$. If we write the length in the units of magnetic length ($l = \sqrt{\frac{\hbar}{|eB|}}$) and

enrgy in the units of $\hbar\omega_C$, then,

$$H_0(x,X) = \frac{(\mathbf{p} - e\mathbb{A})^2}{2m} + V(x) = -\frac{1}{2}\frac{d^2}{dx^2} + F(x,X) + U(x) \tag{5.2}$$

Here,

$$F(x,X) = \begin{cases} \frac{X^2}{2} \text{ ,in the S region} \\ \frac{1}{2}(x-X)^2 \text{ ,in the N region} \end{cases} \tag{5.3}$$

The pair potential for an NS junction can be taken as,

$$\Delta = \begin{cases} \Delta_0 \text{ ,in S region} \\ 0 \text{ ,in B and N region} \end{cases} \tag{5.4}$$

In Sec. 2.7 of **Chapter 2** we have described the breaking of time reversal symmetry in the BdG equation which explains the term $H_0(x,-X)$ in the Hamiltonian. Now putting Eq. (5.2) in (5.1), we get,

$$\begin{bmatrix} -\frac{1}{2}\frac{d^2}{dx^2} + F(x,+X) - \frac{\nu}{2} + U(x) & \Delta \\ \Delta^* & \frac{\nu}{2} + \frac{1}{2}\frac{d^2}{dx^2} - F(x,-X) - U(x) \end{bmatrix} \begin{bmatrix} f_X \\ g_X \end{bmatrix} = E \begin{bmatrix} f_X \\ g_X \end{bmatrix} \tag{5.5}$$

And, the potential $U(x)$ can be modeled as

$$U(x) = U_0\delta(x+L) + U_0\delta(x-L) + \sum_{n=1}^{N} V_0\Theta\left(x - x_n + \frac{d}{2}\right)\Theta\left(x - x_n - \frac{d}{2}\right) \tag{5.6}$$

Without the barrier [75, 251], the solutions of this BdG equation, with the electron and hole components of the wavefunctions denoted by $f_X(x)$ and $g_X(x)$, are defined as:

$$f_X = a\chi_{\varepsilon_+} = \begin{cases} aU\left(-\left\{\frac{\nu}{2}+E\right\},\sqrt{2}(x-X)\right) \text{ , in N} \\ d_-\gamma_- e^{ixk_-} + d_+\gamma_+ e^{-ixk_+} \text{ , in S} \end{cases} \tag{5.7a}$$

$$g_X = b\chi_{\varepsilon_-} = \begin{cases} bU\left(-\left\{\frac{\nu}{2}-E\right\},\sqrt{2}(x+X)\right) \text{ , in N} \\ d_- e^{ixk_-} + d_+ e^{-ixk_+} \text{ , in S} \end{cases} \tag{5.7b}$$

Here,

$$k_\pm = \left[(\nu \pm i2\Delta_0) - X^2\right]^{1/2} \tag{5.8a}$$

$$\gamma_\pm = \frac{1}{\left(\frac{E_{nX}}{\Delta_0}\right) \mp \sqrt{\left(\frac{E_{nX}}{\Delta_0}\right)^2 - 1}} \tag{5.8b}$$

In presence of the barriers, the problem can be approached in two different ways, (i) *method-I:* we take a finite number of electrostatic barriers in the N region with equal spacing between consecutive barriers resulting in potentail profile given in Eq. (5.6)

$$V(x) = \sum_{n=1}^{N} V_0 \Theta\left(x - x_n + \frac{d}{2}\right)\Theta\left(x - x_n - \frac{d}{2}\right)$$

. (ii) *method-II:* In the second approach, initially the N region in the presence of transverse magnetic field is considered to be subjected to a one dimensional periodic potential of the form

$$V(x) = \sum_{n=-\infty}^{\infty} V_0 \Theta\left(x - nD + \frac{d}{2}\right)\Theta\left(x - nD - \frac{d}{2}\right)$$

so that Bloch condition can be imposed.

5.3 Theoretical Framework of Obtaining Dispersion

5.3.1 Method - I

For an NS junction, the wavefunctions, f_X and g_X are shown in Eq. (5.7). The boundary value conditions are that the wavefunctions should match at the boundary and the discontinuity of the derivative of the wavefunction is adjusted by the delta potential(shown in Eq. (5.6)) at the SN boundary. Using this, the boundary value conditions for the SN boundary at $x = 0$ is given by

$$a \times \chi_{\varepsilon_+}(-X) + b \times 0 = d_- \times \gamma_- + d_+ \times \gamma_+ \tag{5.9a}$$

$$a \times 0 + b \times \chi_{\varepsilon_-}(X) = d_- + d_+ \tag{5.9b}$$

$$a \times |_{\frac{\mathrm{d}\chi_{\varepsilon_+}}{\mathrm{d}x}} x = 0 - d_- \times \gamma_- \times (ik_-) - d_+ \times \gamma_+ \times (-ik_+) = 2U_0 \left(d_- \times \gamma_- + d_+ \times \gamma_+\right) \tag{5.9c}$$

$$b \times |_{\frac{\mathrm{d}\chi_{\varepsilon_-}}{\mathrm{d}x}} x = 0 - d_- \times (ik_-) - d_+ \times (-ik_+) = 2U_0 \left(d_- + d_+\right) \tag{5.9d}$$

The coefficients of a, b, d_- and d_+ from this boundary value equation gives the elements of the transfer matrix $M(X)$

$$M(X) = \begin{bmatrix} \chi_{\varepsilon_+}(-X) & 0 & -\gamma_- & -\gamma_+ \\ 0 & \chi_{\varepsilon_-}(-X) & 1 & 1 \\ |_{\frac{\mathrm{d}\chi_{\varepsilon_+}}{\mathrm{d}x}} x{=}0 & 0 & -\gamma_-(ik_- {+} 2U_0) & \gamma_+(ik_+ {-} 2U_0) \\ 0 & |_{\frac{\mathrm{d}\chi_{\varepsilon_-}}{\mathrm{d}x}} x{=}0 & -(ik_- {+} 2U_0) & \gamma_+(ik_+ {-} 2U_0) \end{bmatrix}. \tag{5.10}$$

We calculate the barrier boundary conditions at $x = 0$, where the left side is N region and right side is B region. Then the boundary value conditions are given by,

$$a \times \chi_{\varepsilon_+}(-X) + b \times 0 = a_B \times \chi_{B,\varepsilon_+}(-X) + b_B \times 0 \tag{5.11a}$$

$$a \times 0 + b \times \chi_{\varepsilon_-}(-X) = a_B \times 0 + b_B \times \chi_{B,\varepsilon_-}(-X) \tag{5.11b}$$

$$a \times |_{\frac{\mathrm{d}\chi_{\varepsilon_+}}{\mathrm{d}x}} x = 0 + b \times 0 = a_B \times |_{\frac{\mathrm{d}\chi_{B,\varepsilon_+}}{\mathrm{d}x}} x = 0 + b_B \times 0 \tag{5.11c}$$

$$a \times 0 + b \times |_{\frac{\mathrm{d}\chi_{\varepsilon_-}}{\mathrm{d}x}} x = 0 = a_B \times 0 + b_B \times |_{\frac{\mathrm{d}\chi_{B,\varepsilon_-}}{\mathrm{d}x}} x = 0 \tag{5.11d}$$

This coefficients of a, b, a_B and b_B in the boundary value conditions Eqs. (5.11) give us the matrix $M_B(X)$

$$M_B(X) = \begin{bmatrix} \chi_{\varepsilon_+}(-X) & 0 & -\chi_{\varepsilon_{B+}}(-X) & 0 \\ 0 & \chi_{\varepsilon_-}(-X) & 0 & \chi_{\varepsilon_{B-}}(-X) \\ |_{\frac{\mathrm{d}\chi_{\varepsilon_+}}{\mathrm{d}x}\, x=0} & 0 & |_{\frac{\mathrm{d}\chi_{\varepsilon_{B+}}}{\mathrm{d}x}\, x=0} & 0 \\ 0 & |_{\frac{\mathrm{d}\chi_{\varepsilon_-}}{\mathrm{d}x}\, x=0} & 0 & |_{\frac{\mathrm{d}\chi_{\varepsilon_{B-}}}{\mathrm{d}x}\, x=0} \end{bmatrix}. \tag{5.12}$$

A single potential barrier that is responsible for inserting ICES in the N region can be written as, $V(x) = V_0\Theta(x + d/2)\Theta(d/2 - x)$. For this we create the transfer matrices from the boundary conditions at every edge(SN, NB,BN and NS) as

$$\mathcal{M} = \begin{bmatrix} M_{SN} & 0 & 0 & 0 \\ 0 & M_{NB} & 0 & 0 \\ 0 & 0 & M_{BN} & 0 \\ 0 & 0 & 0 & M_{NS} \end{bmatrix}. \tag{5.13}$$

Now the M_{SN} and M_{NS} are derived from M by axis transformations. For M_{SN} the transformation is $x \to x + L$. For M_{NS} the transformation is $x \to -x - L$. Now the M_{BN} and M_{NB} are derived from M_B by axis transformations. For M_{NB} the transformation is $x \to x + d/2$. For M_{BN} the transformation is $x \to -x - d/2$. The E-X dispersion is given by,

$$\det(\mathcal{M}) = \det(M_{SN})\det(M_{NB})\det(M_{BN})\det(M_{NS}) = 0 \tag{5.14}$$

This approach can be generalized for the case of n barriers in the QH region,

$$\mathcal{M} = \begin{bmatrix} M_{SN} & 0 & 0 & \dots & 0 & 0 & 0 \\ 0 & M_{NB}^{(1)} & 0 & \dots & 0 & 0 & 0 \\ 0 & 0 & M_{BN}^{(1)} & \dots & 0 & 0 & 0 \\ \vdots & \vdots & \vdots & \ddots & \vdots & \vdots & \vdots \\ 0 & 0 & 0 & \dots & M_{NB}^{(n)} & 0 & 0 \\ 0 & 0 & 0 & \dots & 0 & M_{BN}^{(n)} & 0 \\ 0 & 0 & 0 & \dots & 0 & 0 & M_{NS} \end{bmatrix} \tag{5.15}$$

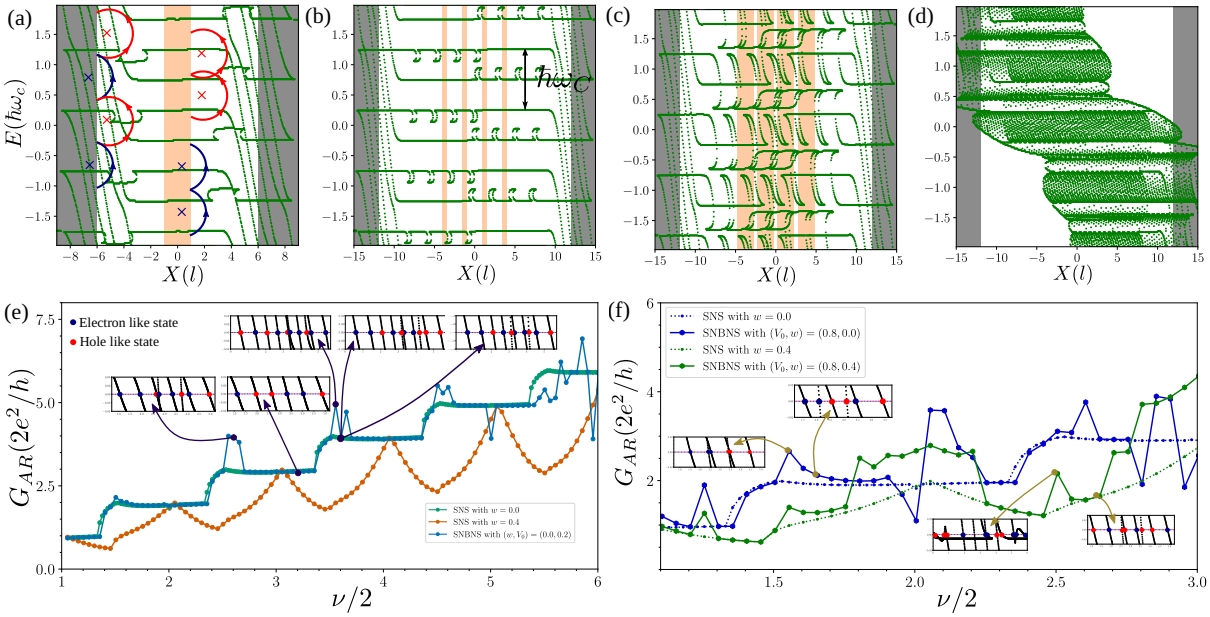

FIG. 5.2: We show the dispersion plots for the SNS junctions with barriers in the N region for $\nu = 5.5$ using Eq. (5.16). To show the presence of Landau levels, we set $\Delta_0 = 2.0\hbar\omega_C$. In (a), we have one barrier with width $d = 2$. In (b), (c) we have taken 4 barriers in the N region with (b) $V_0 = 0.2$, separation $D = 2$ and $d = 1$, (c)$V_0 = 0.9$, $D = 0.5$ and $d = 2$ and in (d) we have taken 40 barriers in the N region with $d = 0.3$ and $D = 0.3$. The red semicircles denote the classical electron orbit, and the blue semicircles denote the classical hole orbits. In (e) and (f), we compare the conductivity of the SNS junction with a single barrier in the N region with two cases of the SNS junction with $w = 0$ and $w = 0.4$ for different ranges of V_0 . Here w is defined by $w = 2U_0/\sqrt{\nu}$. In this case, we have taken $\Delta_0 = 0.01 \times \nu$. Here, the distance between two SN edges is taken as 6 and the width of the barrier is taken as 1. In the inset of (e) and (f) we show the intermediate chiral edge states which contribute to the fluctuation in conductivity. the red and blue dot denotes their electron like or hole like nature.

For this, the dispersion is given by,

$$\det(\mathcal{M}) = \det(M_{SN}) \left[\prod_{i=1,2...n} \det\left(M_{NB}^{(n)}\right) \det\left(M_{BN}^{(n)}\right) \right] \det(M_{NS}) = 0 \tag{5.16}$$

5.3.2 Method- II

Now we consider an large array of barrier potentials in the QH region. The wavefunctions in n'th N region, extended from $x = x_n$ to $x_n + D$ is given by,

$$(f, g)_{nX} = (a, b)_n U \left[\left(-\frac{\nu}{2} \pm E \right), \sqrt{2}\,(x - x_n \mp X) \right] \tag{5.17}$$

The wavefunctions in n'th B region, extended from $x = x_n + D$ to $x_n + D + d$ is given by,

$$(f,g)_{B,nX} = (a,b)_{B,n} U\left[\left(-\frac{\nu}{2} \pm E - V_0\right), \sqrt{2}\,(x - x_n - D \mp X)\right] \tag{5.18}$$

The wavefunctions in $(n+1)$'th N region, extended from $x = x_n + D + d + D$ to $x_n + 2D + 2d$ is given by,

$$(f,g)_{(n+1)X} = (a,b)_{n+1} U\left[\left(-\frac{\nu}{2} \pm E\right), \sqrt{2}\,(x - x_n - D - d \mp X)\right] \tag{5.19}$$

Now the boundary value condition in $x = x_n + D$ gives,

$$a_n U\left[\left(-\frac{\nu}{2} + E\right), \sqrt{2}\,(D - X)\right] = a_{B,n} U\left[\left(-\frac{\nu}{2} + E - V_0\right), \sqrt{2}\,(-X)\right] \tag{5.20}$$

$$b_n U\left[\left(-\frac{\nu}{2} - E\right), \sqrt{2}\,(D + X)\right] = b_{B,n} U\left[\left(-\frac{\nu}{2} - E - V_0\right), \sqrt{2}\,(+X)\right] \tag{5.21}$$

This boundary condition gives,

$$\begin{bmatrix} a_{B,n} \\ b_{B,n} \end{bmatrix} = \begin{bmatrix} \frac{U\left[\left(-\frac{\nu}{2}+E\right), \sqrt{2}(D-X)\right]}{U\left[\left(-\frac{\nu}{2}+E-V_0\right), \sqrt{2}(-X)\right]} & 0 \\ 0 & \frac{U\left[\left(-\frac{\nu}{2}-E\right), \sqrt{2}(D+X)\right]}{U\left[\left(-\frac{\nu}{2}-E-V_0\right), \sqrt{2}(+X)\right]} \end{bmatrix} \begin{bmatrix} a_n \\ b_n \end{bmatrix} \tag{5.22}$$

Again the boundary value condition at $x = x_n + D + d$ gives,

$$a_{B,n} U\left[\left(-\frac{\nu}{2} + E - V_0\right), \sqrt{2}\,(d - X)\right] = a_{n+1} U\left[\left(-\frac{\nu}{2} + E\right), \sqrt{2}\,(-X)\right] \tag{5.23}$$

$$b_{B,n} U\left[\left(-\frac{\nu}{2} - E - V_0\right), \sqrt{2}\,(d + X)\right] = b_{n+1} U\left[\left(-\frac{\nu}{2} - E\right), \sqrt{2}\,(+X)\right] \tag{5.24}$$

This boundary condition gives,

$$\begin{bmatrix} a_{n+1} \\ b_{n+1} \end{bmatrix} = \begin{bmatrix} \frac{U\left[\left(-\frac{\nu}{2}+E-V_0\right), \sqrt{2}(d-X)\right]}{U\left[\left(-\frac{\nu}{2}+E\right), \sqrt{2}(-X)\right]} & 0 \\ 0 & \frac{U\left[\left(-\frac{\nu}{2}-E-V_0\right), \sqrt{2}(d+X)\right]}{U\left[\left(-\frac{\nu}{2}-E\right), \sqrt{2}(+X)\right]} \end{bmatrix} \begin{bmatrix} a_{B,n} \\ b_{B,n} \end{bmatrix} \tag{5.25}$$

By combining this we get,

$$\begin{bmatrix} a_{n+1} \\ b_{n+1} \end{bmatrix} = \begin{bmatrix} \frac{U\left[\left(-\frac{\nu}{2}+E-V_0\right),\sqrt{2}(d-X)\right]}{U\left[\left(-\frac{\nu}{2}+E\right),\sqrt{2}(-X)\right]} & 0 \\ 0 & \frac{U\left[\left(-\frac{\nu}{2}-E-V_0\right),\sqrt{2}(d+X)\right]}{U\left[\left(-\frac{\nu}{2}-E\right),\sqrt{2}(+X)\right]} \end{bmatrix} \times \begin{bmatrix} \frac{U\left[\left(-\frac{\nu}{2}+E\right),\sqrt{2}(D-X)\right]}{U\left[\left(-\frac{\nu}{2}+E-V_0\right),\sqrt{2}(-X)\right]} & 0 \\ 0 & \frac{U\left[\left(-\frac{\nu}{2}-E\right),\sqrt{2}(D+X)\right]}{U\left[\left(-\frac{\nu}{2}-E-V_0\right),\sqrt{2}(+X)\right]} \end{bmatrix} \begin{bmatrix} a_n \\ b_n \end{bmatrix} \quad (5.26)$$

As we are putting a periodic potential $V(x) = \sum_{n=-\infty}^{\infty} V_0 \Theta\left(x - nD + \frac{d}{2}\right) \Theta\left(x - nD - \frac{d}{2}\right)$, in Eq. (5.2). For an infinitely large lattice, the wavefunctions, f_X and g_X in Eq. (5.17) and Eq. (5.19) satisfies the Bloch conditions. Under the bloch condition if we define the Bloch momentums of electrons and holes as K_1 and K_2,

$$(f,g)_X(x+d+D) = (f,g)_X(x) \times cos(K_{1,2}(d+D)) \quad (5.27)$$

In Eq. (5.3.2), we see that the ratio of the wavefunctions are real numbers. So we put the Bloch condition with only cosine term. Here, we have separated the electron and hole Bloch momentum as they are decoupled in N and B region. We satisfy the Bloch condition saparately for electron and hole part of the wavefunctions, which are stationary solutions of Eq. (5.17). Eq. (5.27) gives,

$$\frac{(a,b)_{n+1}}{(a,b)_n} = \cos\big(K_{(1,2)}(d+D)\big) \quad (5.28)$$

Combining Eq. (5.3.2) and (5.28), we get

$$\cos(K_1(d+D)) = \frac{U\left[\left(-\frac{\nu}{2}+E-V_0\right),\sqrt{2}\,(d-X)\right]}{U\left[\left(-\frac{\nu}{2}+E\right),\sqrt{2}\,(-X)\right]} \times \frac{U\left[\left(-\frac{\nu}{2}+E\right),\sqrt{2}\,(D-X)\right]}{U\left[\left(-\frac{\nu}{2}+E-V_0\right),\sqrt{2}\,(-X)\right]} \quad (5.29a)$$

$$\cos(K_2(d+D)) = \frac{U\left[\left(-\frac{\nu}{2}-E-V_0\right),\sqrt{2}\,(d+X)\right]}{U\left[\left(-\frac{\nu}{2}-E\right),\sqrt{2}\,(+X)\right]} \times \frac{U\left[\left(-\frac{\nu}{2}-E\right),\sqrt{2}\,(D+X)\right]}{U\left[\left(-\frac{\nu}{2}-E-V_0\right),\sqrt{2}\,(+X)\right]} \quad (5.29b)$$

Now for a large number of barriers, the allowed solutions are those (E, X) values, for which one gets $|\cos(K_1(d+D))| < 1$ in Eq. (5.29a) and $|\cos(K_2(d+D))| < 1$ in Eq. (5.29b). Now we have the superconducting boundaries of this lattice at $x = -L$ and $x = +L$. We assume the solutions are Bloch periodic inside this region. Outside the region it take the usual superconductor wavefunction defined in (5.7a) and (5.7b).

Now, with the wavefunctions f_X and g_X described in Eq. (5.17) and inserting the Bloch conditions Eq. (5.29), we use the boundary value conditions similar to Sec. 5.3. Let us calculate the bounadry value conditions for an nth NB barrier located at $x_n = 0$. This boundary condition is between nth N region and n th B region. The wavefunction for this is given in Eq. (5.17) and (5.18).

$$a_n \times e^{iK_1(n-1)(D+d)}\chi_{\varepsilon_+}(-X) + b_n \times 0 = a_{B,n} \times e^{iK_1((n-1)(D+d)+d)}\chi_{\varepsilon_{B+}}(-X) + b_{B,n} \times 0 \tag{5.30}$$

$$a_n \times 0 + b_n \times e^{iK_2(n-1)(D+d)}\chi_{\varepsilon_-}(-X) = a_{B,n} \times 0 + b_{B,n} \times e^{iK_2((n-1)(D+d)+d)}\chi_{\varepsilon_{B-}}(-X) \tag{5.31}$$

$$a_n \times e^{iK_1(n-1)(D+d)}|_{\frac{\mathrm{d}\chi_{\varepsilon_+}}{\mathrm{d}x}} x = 0 + b_n \times 0 = a_{B,n} e^{iK_1((n-1)(D+d)+d)} \times |_{\frac{\mathrm{d}\chi_{B,\varepsilon_+}}{\mathrm{d}x}} x = 0 + b_{B,n} \times 0 \tag{5.32}$$

$$a_n \times 0 + b_n \times e^{iK_2(n-1)(D+d)}|_{\frac{\mathrm{d}\chi_{\varepsilon_-}}{\mathrm{d}x}} x = 0 = a_{B,n} \times 0 + b_{B,n} \times \times e^{iK_2((n-1)(D+d)+d)}|_{\frac{\mathrm{d}\chi_{B,\varepsilon_-}}{\mathrm{d}x}} x = 0 \tag{5.33}$$

From this we calculate the matrix $M^{(n)}_{B,lat}$ as the coefficients of a_n, b_n, c_n and d_n.

Although we are considering Bloch condition, in the JJ, NS and SN interfaces breaks the lattice translational symmetry. To introduce that aspect we assume that the Bloch condition can be used with the following modifications. The change in the wavefunction is limited upto first n barriers in right and left side of the N region due to the presence of SN and NS edges and inside that the Bloch periodicity remains intact. Under this assumption, we increase n in step of 1 till we get covergence of the energy spectrum for n and $n+1$th case. This condition holds better as one approaches the limit $n/N \ll 1$, which in turn implies stronger limit of $(d+D)/L \ll 1$. Unlike the method adopted by Hatsugai [252] the current scheme is not contingent upon the

formation of magnetic Brillouin zone which is a consequence of lattice translational symmetry. Those results can be recovered in the limit $V_0 \to \infty, d \to 0$, such that $V_0 d$ is finite and number of barriers $n \to \infty$.

In this method, the dispersion can be obtained from,

$$\det(\mathcal{M}) = \det(M_{SN}) \left[\prod_{i=1,2...n} \det\left(M_{NB}^{(n)}\right) \det\left(M_{BN}^{(n)}\right) \right] \left[\prod_{j=1,2...(N-2n)} \det\left(M_{NB,lat}^{(n+j)}\right) \det\left(M_{BN,lat}^{(n+j)}\right) \right] \left[\prod_{k=1,2...n} \det\left(M_{NB}^{(N-n+k)}\right) \det\left(M_{BN}^{(N-n+k)}\right) \right] \det(M_{NS}) = 0 \tag{5.34}$$

5.4 Conductivity

The method of calculation of conductivity for such systems is described below.

1. Without any externally applied bias voltage, the Landau Level Andreev Bound States (LLABS) determined from the $E = 0$ with the dispersion (the dotted red line in FIG. 5.2), and the chemical potential is absorbed in filling fraction ν in the BdG equations of N and S regions (For details see appendix) contributes to the Josephson current .

2. In Landauer-Buttiker formalism, the conductivity of this JJ can now be straight-forwarded by summing over the hole probability as [88]

$$G_{AR} = \frac{e^2}{\pi h} \sum_{n=1}^{n^*} B_n \tag{5.35}$$

where $B_n = \int_x |g_X|^2$ of all electron-like states staisfying $\int_x \left[|f_X|^2 - |g_X|^2 \right] > 0$ such that $B_n \leq 1/2$.

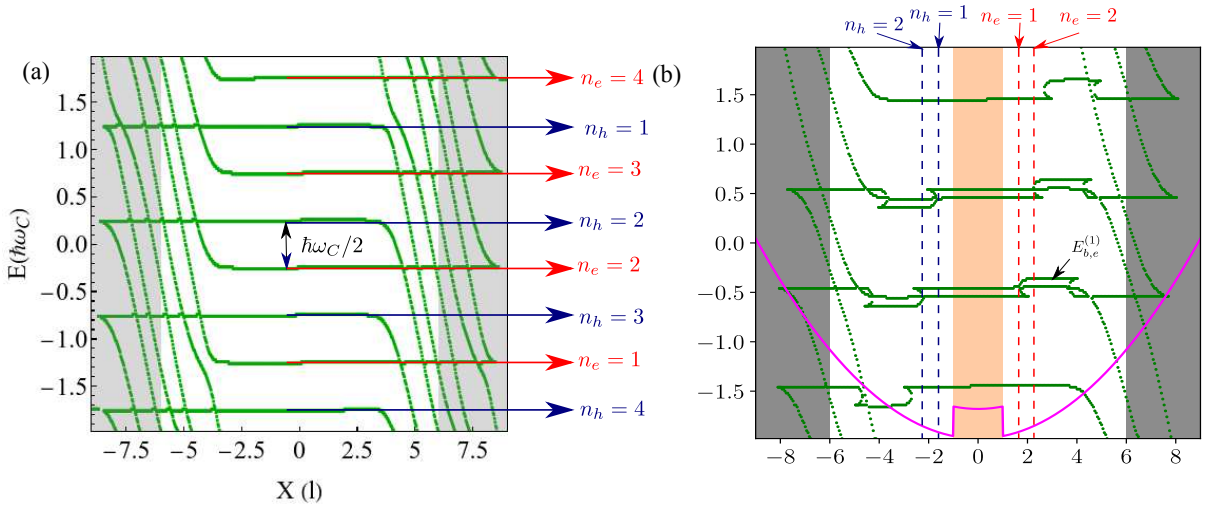

FIG. 5.3: In (a) we show the dispersion(energy vs guiding center) plot for an SNS junction for the case of $\nu = 5.5$. These are the solutions of $\det(M_{SN})\det(M_{NS}) = 0$. We denote the LLs from f_X by n_e and LLs from g_X by n_h. In (b) we show the dispersion for the case of a single barrier present in the QH region. We have taken $\nu = 2.1$ and $d = 2$. The maroon curve shows the effective potential $V_{eff} = (x - X)^2/2 + V_0\Theta(-x + d/2)\Theta(x + d/2)$ acting on the LLs for $X = 0$. The value of the y axis in this curve is scaled appropriately to display with the dispersion plot and the x axis is exact. The dotted red (blue) lines show the positions of the start of the lifting of degeneracy in f_X (g_X) LLs due to barrier potential in the QH region. n_e and n_h are the same as in (a). $E^{(1)}_{b,e}$ corresponds to the eigenvalue inside the barrier region and we have given its coressponding expression in the text.

5.5 Dispersion of SQHS and lifting of degeneracy in dispersion with single barrier in the quantum Hall region

The BdG equation Eq. (5.1) in the N region decouples into following equations,

$$[H_0(x, X) - \mu]\, f_X = E f_X \tag{5.36}$$

$$[H_0(x, -X) - \mu]\, g_X = -E g_X \tag{5.37}$$

Wavefunctions f_X and g_X from Eq. (5.36) and (5.37) are the solutions of same equation (5.36) with transformation $E \to -E$ and $X \to -X$.

$$H_0(x, X) f_X = (E + \mu) f_X \tag{5.38}$$

$$H_0(x, -X) g_X = -(E - \mu) g_X \tag{5.39}$$

In FIG. 5.3, we plot E vs X for these solutions. If we confine one dimensional electrons like [77], we get the solutions of Eq. (5.38). However, here the presence of f_X and g_X give two types of Landau levels with energies $(E+\mu)$ and $-(E-\mu)$ and underscores the effect of Andreev refelction on the Landau levels in a SNS junction. From Eq. (5.38) and (5.39), the n'th LL from f_X and g_X has energy eigenvalues, $[(n_e+1/2)-\nu/2]$ and $-[(n_e+1/2)-\nu/2]$ respectively. In FIG. 5.3 we see the energy gap is between the states $n_e=2$ and $n_h=2$. Their energy gap becomes $\hbar\omega_C/2$.

Now let us discuss the single barrier dispersion shown in FIG. 5.2 (a). For a square barrier inside the quantum Hall region, inside the barrier H_0 from Eq. (5.2) becomes,

$$H_0(x,X) = -\frac{1}{2}\frac{d^2}{dx^2} + \frac{1}{2}(x-X)^2 + V_0\Theta(-x+\frac{d}{2})\Theta(x+\frac{d}{2}) \tag{5.40}$$

Now, the axis transformation to create the M_{NB} (given in Eq. (5.13) in the main text) matrix, $X \to X + d/2$ (discussed in the main text). The boundary value conditions are discussed in Eq. (5.11) in Sec. 5.3. Now Eq. (5.40) becomes,

$$H_0(x,X) = -\frac{1}{2}\frac{d^2}{dx^2} + \frac{1}{2}(x-X-\frac{d}{2})^2 + V_0\Theta(-x+\frac{d}{2})\Theta(x+\frac{d}{2}). \tag{5.41}$$

As we are discussing the matrix M_{NB} due to boundary condition at $x=-d/2$, (left side of the barrier), the value of the second term in the hamiltonian becomes $\frac{1}{2}(X+d)^2$ at $x=-d/2$. We solve the eigenvalue equation and then match the boundary value conditions at $x=-d/2$ to obtain M_{NB}. The dispersion relation is plotted as E vs X. The effect of the term $\frac{1}{2}(X+d)^2$ can be seen at $X=d$ in the dispersion plot. For a given value of energy, E, LLs of different orders form in the neighborhood of the boundary and correspond to different values of X near the boundary. In our case the NB boundary is at $x=-d$. Hence the lifting of degeneracy due to the barrier potential are shifted in the X axis as compared to exact edges of NB boundary. Comparing with the case of a confined quantum Hall system [77] we also see the exact location depends on the quantum number of that LL. In FIG. 5.3 (b) we show the location where the lifting of degeneracy occurs in the LLs. In the case considered here, $d=2$. Hence we see that this location for f_X LLs occur in the neighbourhood of the point $X=2$ in the dispersionn plot.

Now let us discuss the lifting of degeneracy inside the barrier region with the help of

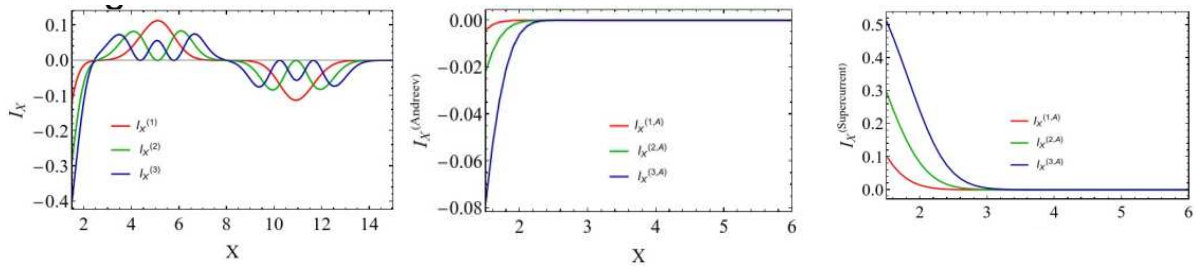

FIG. 5.4: Edge current, Andreev current and Supercurrent for the first three electron like LL states.

FIG. 5.3 (b). The eigenvalues inside the barrier from Eq. (5.41) can be written as $E_{b,e} = [(n_e + 1/2) - \nu/2 + V_0]$. For hole states g_X, the eigenvalues are, $E_{b,h} = -[(n_e + 1/2) - \nu/2 + V_0]$. This shows that the change in eigenvalue is opposite for f_X LLs and g_X LLs. Due to the presence of the barrier, we now have two regions of degenerate states, (i) inside the barrier and (ii) outside the barrier. The boundary condition allows the energy to continuously change from $[(n_e + 1/2) - \nu/2]$ to $[(n_e + 1/2) - \nu/2 + V_0]$ and form intermediate chiral edge states. The same analysis can be done for the g_X LLs and their direction is opposite to the f_X LLs in the dispersion plot.

5.6 Distribution of various current components

The total quasiparticle charge current in the superconductor-quantum Hall juctions is given by [75]

$$I_X^{(Q)} = I_X^{(Q,n)} - I_X^{(Q,a)} + I_X^{(Q,s)}. \tag{5.42}$$

This current captures the contribution from the currect carrying edge states (normal reflection) and Andreev reflection in such junctions. It has three components which composes ordinary edge current $I_X^{(Q,n)}$, Andreev reflection contribution ($I_X^{(Q,a)}$) and Supercurrent ($I_X^{(Q,s)}$).

$$I_X^{(Q,n)} = \frac{el^2}{\hbar L_y}\frac{\partial E}{\partial X} \tag{5.43a}$$

$$I_X^{(Q,a)} = \frac{el^2}{\hbar L_y}\frac{\partial E}{\partial X} 2\int_x |g_x(x)|^2 \tag{5.43b}$$

$$I_X^{(Q,s)} = \frac{el^2}{\hbar L_y} 2\Delta \int_x \Theta(-x)\left[g_X^* \frac{df_X}{dX} - f_X^* \frac{dg_X}{dX}\right] \tag{5.43c}$$

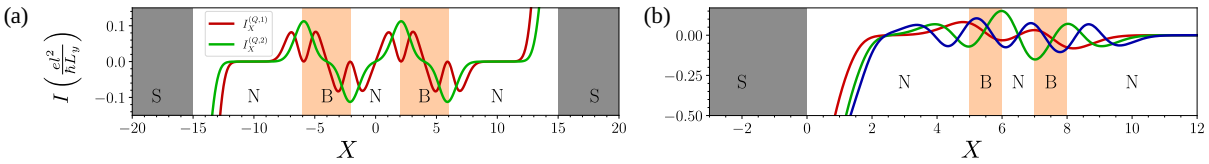

FIG. 5.5: In (a), we show the charge current for an SNS junction with two barriers of $d = 4$ and $D = 4$. In (b), we show the charge current for $d = 4$ and $D = 4$ in an NS junction with two barriers in the N region.

In FIG. 5.5 (a) and (b) we show the charge current as a function of the guiding center demonstrating how with the reduction of the separation between barriers the current contribution due to LLs of a given quantum number interfere.

5.7 Analysis of the Dispersion and the Conductivity Plots

Now, in light of the above discussion we shall analyze the dispersion and the conductivities we calculated from Method-I and shown in FIG. 5.2. In FIG. 5.2 (a) -(d), using (5.16) we show the E vs X we dispersions for (a) single barrier with width $d = 2$, (b) four barriers with $d = 1$, separation $D = 2$ and $V_0 = 0.2$, (c)four barriers with $d = 2$, separation $D = 0.5$ and $V_0 = 0.9$ and (d) 40 barriers with separation $D = 0.3$ and $d = 0.3$, with all barrier(s) placed symmetrically inside the QH region. The formation of the ICES and their variation in the electron and hole LLs in these figures are described in detail in Sec. 5.5 with the help of FIG. 5.3 (a) and (b). Comparison of FIG. 5.2(a) and (b) shows that the addition of more electrostatic barriers in the QH region increases the number intermediate chiral edge states inside the QH region. The intermediate chiral edge states form a convexo-concave structure over the usual LLs over a range of X. In (c) we reduced separation between the barriers D, and also increased the value of V_0. The increase in V_0 results in overlapping of convexo-concave (CC) structures from different LLs (inter LL overlap), whereas reduced D leads to overlapping

of the adjacent CC structures in the same LLs (intra LL overlap). As we see this deeply effect the subsequent LL band formation, when number of barriers are large.

In (d) , a relatively large number of barriers $n = 40$ in the QH region lead to the formation of LL bands due to inter and intra-LL overlap of the CC regions in the dispersion. The interband region also contains states. This situation may be compared with the seminal work by Hatsugai [252] with two fundamental differences (a) broken lattice translational symmetry by NS interface and (b) electron hole conversion due to Andreev reflection. As a result even though the Landau bands are clearly formed the width of the bands and the states in between such bands are very different from that of an unbounded QH system in a one dimensional lattice under tight-binding approximation.

Finally, in (e) and (f) we plot the variation of Josephson conductivity as a function of filling fraction $\frac{\nu}{2}$ calculated with the help of Eq. (5.35).

In (e), particularly we plot conductance for the cases of S-QH-S junctions (i) without any barrier, (ii) delta function barriers at the NS edges which affect the Andreev reflection and then (iii) scatterer in the form of one rectangular barrier symmetrically placed in the QH region which introduces ICES. In the inset we show the existence of the ICES at the Fermi energy, and its effect on the conductivity.

We also provide the tables for some of the insets in TABLE 5.1, 5.2 and 5.3.

n	B_n
1	0.471016
2	0.499073
3	0.502286
4	0.365599
5	0.497525
6	0.500802
7	0.0704867
8	0.528958

Table 5.1: Hole probabilities of $\nu = 5.31$

n	B_n
1	0.465506
2	0.500595
3	0.501658
4	0.498537
5	0.499180
6	0.534521

Table 5.2: Hole probabilities of $\nu = 5.41$

In FIG. 5.2 (f) we have studied joint effect of delta function scatterer at the NS edge and a symmetrically placed rectangular barrier in the QH region, on the Jospephson conductance of the SQHS junction. Additionally the height of the barrier V_0 is increased as compared to FIG. 5.2(g). Pronounced change in the conductance was observed.

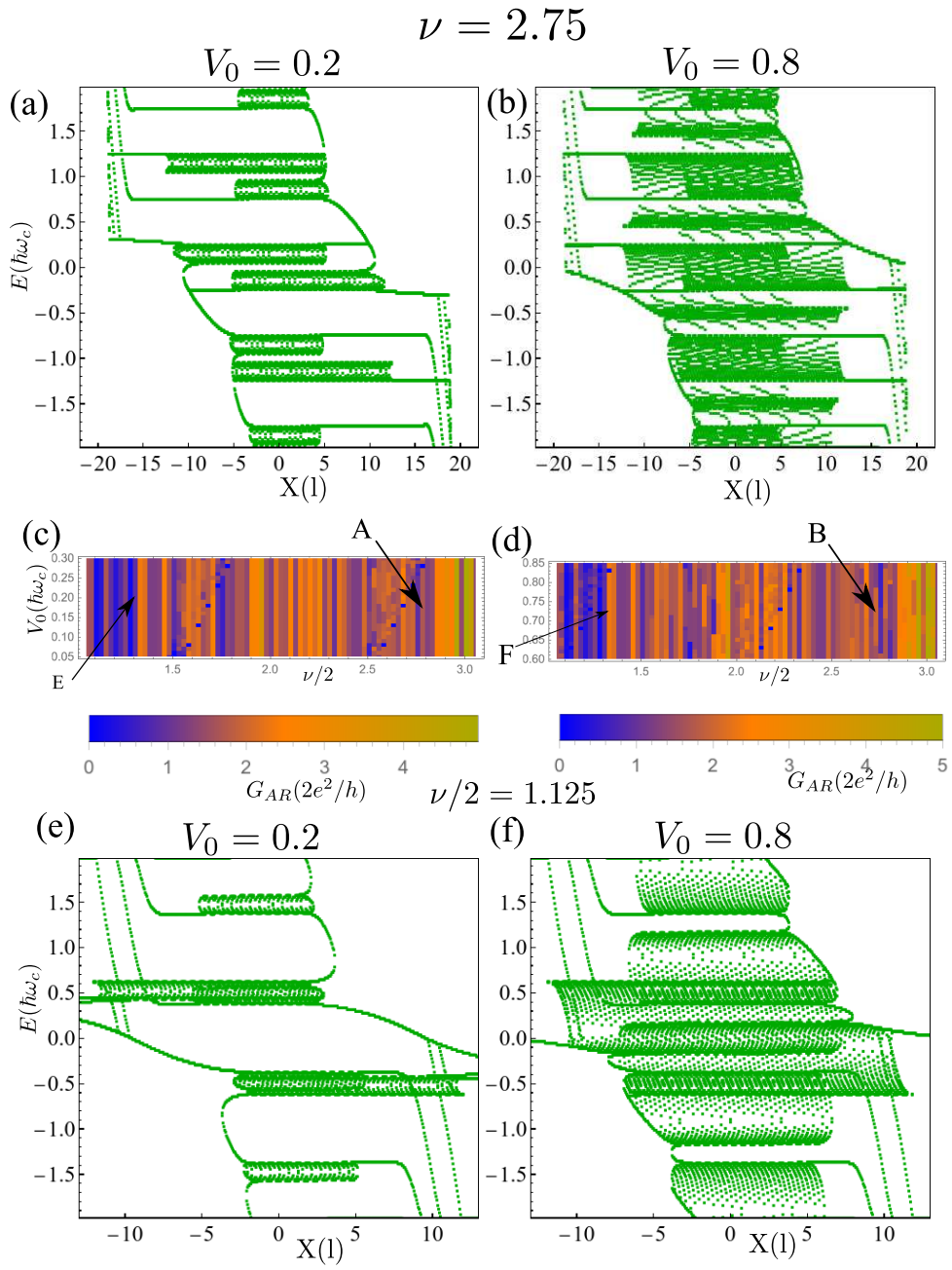

FIG. 5.6: In (a), (b), (e) and (f) we show the dispersion plot for SN(BN)^{n}S junction with $n = 30$. For (a) $\nu/2 = 2.75$ and $V_0 = 0.2$, (b) $\nu/2 = 2.75$ and $V_0 = 0.8$, (e) $\nu/2 = 1.125$ and $V_0 = 0.2$ and (f) $\nu/2 = 1.125$ and $V_0 = 0.8$. The with of the barriers are taken as $d = 0.3$ and the separation between them is taken as $D = 0.3$. In (c) and (d) we show the conductivity, calculated using Eq. (5.35) as a function of both V_0 and $\nu/2$. The x axes of the dispersion plots (a), (b), (e) and (f) are X and the y axes are energy E. The E vs X dispersions (a), (b), (e) and (f) correspond to 4 points A, B , E and F in the conduction plots (c) and (d). For the dispersion we have taken $\Delta = 2$ and the conduction plots we have taken $\Delta = 0.01\nu$. The dispersion plots are calculated with same values of ν and V_0. However as we have changed the Δ for the conductance calculation the window of energy in which Andreev bound states are formed get reduced to -0.01ν to $+0.01\nu$.

n	B_n for $\nu/2 = 3.555$	B_n for $\nu/2 = 3.605$	B_n for $\nu/2 = 3.655$
1	0.50275	0.48505	0.47407
2	0.49439	0.49630	0.49795
3	0.50486	0.50405	0.50315
4	0.49543	0.49607	0.49661
5	0.50456	0.50418	0.50339
6	0.00230	0.00004	0.07291
7	0.49509	0.49586	0.49669
8	0.50566	0.58670	0.50193
9	0.48991	0.50387	0.32144
10	0.49729	0.51516	0.52569

Table 5.3: Hole probabilities of $\nu/2 = 3.555$, 3.605 and 3.655 for the inset of FIG. 5.2(e).

To gain more insight in the modification of Jospephson conductivity due to the existence of such ICES and the consequent LL band formation, in FIG. 5.6 (c) and (d) we study the variation of conductace due to multiple equidistant rectangular barriers again symmetrically placed in the QH region over a range of ν and V_0. To elucidate the resulting behavior further, we the dispersion relation in (a), (b), (e) and (f) which correspond's to four specific points in the V_0, ν plane. We can observe strong Josephson conductance fluctuations over the plataues. The fluctuation is due the formation of Landau bands due to intra and inter LL overlap of ICES. For lower value of V_0 (a) and (e) it is almost due to intra LL overlap of the ICES There are large gaps between the bands and clear edge states between the bands somewhat similar to the case studied by [252], (ii) in (b) and (f) the LL bands are more complex and accompanied by additional inter LL overlapping of ICES that mixes different quantum numbers corresponding to particle and hole. This is very different from the previous case, and also contains a significant number of intermediate states between two bands. More detailed discussion is given in Sec. 5.5 with FIG. 5.3. The two different mechanism of formation of LL bands due to intra and inter LL overlap of ICES injected by array of rectangular barrier potentials and the modification of Josephson conductivity in S-QH-S junction is one of most important findings of this work.

5.7.1 Comparison of the transfer matrix method with and without Bloch Condition

We have also compared the results obtained from Method-I and Method-II to check the lattice effects. We have compared the number of points in the E vs X dispersion plots (bound states)

for different values of n using both methods. In FIG. 5.7 we show that as we change n, for large lattices the number of bound states start showing convergence towards the result obtained from Method-I. This shows both methods provide same result for large lattices. Unlike the method adopted by Hatsugai [252] the current scheme is not contingent upon the formation of magnetic Brillouin zone which is a consequence of lattice translational symmetry.

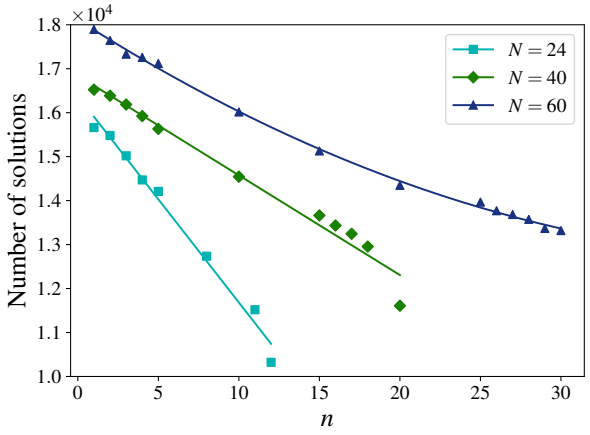

FIG. 5.7: The number of points in the E-X dispersion plots (bound states) obtained from the method II Eq. (5.34) for the case of $N = 24, 40$ and 60. The solid line denotes the fitted curve. The last points in each curve is where we do not have Bloch condition at all. This is same as the results obtained using Method-I.

5.8 Graphene based superconductor- quantum Hall- superconductor junctions

Now inspired by the earlier problem, here we study the effect of external electrostatic barrier potential on monolayer graphene based Josephson junctions [29, 83, 86]. The regions $|x| > L$ are covered by superconducting electrodes similar to what we consider in **Chapter 4**. Due to proximity effect these regions become two-dimensional superconductors [41, 83, 188]. The graphene region $|x| < L$ is exposed to uniform magnetic field [10]. The graphene LLs are different from non-relativistic system due to its linear dispersion. We shall see from the solutions discussed from the subsequent sections that the graphene LLs are not equispaced in the energy. The external potential can be constructed using a gate potential in graphene similar to the non-relativistic two-dimensional system discussed earlier.

5.8.1 DBdG equation

In **Chapter 2**, we have discussed how the usual BdG equation gets transformed in the presence of magnetic field and electrostatic potential. Eq. (4.12) in 2.7 shows the DBdG equation in such system,

$$\begin{bmatrix} v_F\tau_0 \otimes (\mathbf{p}+e\mathbf{A})\cdot\sigma + V(x) - \mu & \Delta \\ \Delta^* & \mu - v_F\tau_0 \otimes (\mathbf{p}-e\mathbf{A})\cdot\sigma - V(x) \end{bmatrix} \begin{bmatrix} \Psi_e \\ \Psi_h \end{bmatrix} = \varepsilon \begin{bmatrix} \Psi_e \\ \Psi_h \end{bmatrix} \tag{5.44}$$

5.8.2 Solution in the G Region

In the absence of any external potential, G region the DBdG equation becomes,

$$\begin{bmatrix} v_F\tau_0 \otimes (\mathbf{p}+e\mathbf{A})\cdot\sigma - \mu & 0 \\ 0 & \mu - v_F\tau_0 \otimes (\mathbf{p}-e\mathbf{A})\cdot\sigma \end{bmatrix} \begin{bmatrix} \Psi_e \\ \Psi_h \end{bmatrix} = \varepsilon \begin{bmatrix} \Psi_e \\ \Psi_h \end{bmatrix} \tag{5.45}$$

Here the wavefunctions contain Ψ_e and Ψ_h, a pair of four dimensional vectors, which represent the electron and hole excitaion. If we choose Ψ_e and Ψ_h as $\Psi_e = (\psi_{e1}, \psi_{e2}, \psi_{e3}, \psi_{e4})$ and $\Psi_h = (\psi_{h1}, \psi_{h2}, \psi_{h3}, \psi_{h4})$, then from Eq. (5.45), we can write

$$\begin{bmatrix} -\mu & v_F(\pi_x - i\pi_y) & 0 & 0 \\ v_F(\pi_x + i\pi_y) & -\mu & 0 & 0 \\ 0 & 0 & \mu & -v_F(\bar{\pi}_x - i\bar{\pi}_y) \\ 0 & 0 & -v_F(\bar{\pi}_x + i\bar{\pi}_y) & \mu \end{bmatrix} \begin{bmatrix} \psi_{e1} \\ \psi_{e2} \\ \psi_{h1} \\ \psi_{h2} \end{bmatrix} = \varepsilon \begin{bmatrix} \psi_{e1} \\ \psi_{e2} \\ \psi_{h1} \\ \psi_{h2} \end{bmatrix} \tag{5.46}$$

and,

$$\begin{bmatrix} -\mu & v_F(\pi_x - i\pi_y) & 0 & 0 \\ v_F(\pi_x + i\pi_y) & -\mu & 0 & 0 \\ 0 & 0 & \mu & -v_F(\bar{\pi}_x - i\bar{\pi}_y) \\ 0 & 0 & -v_F(\bar{\pi}_x + i\bar{\pi}_y) & \mu \end{bmatrix} \begin{bmatrix} \psi_{e3} \\ \psi_{e4} \\ \psi_{h3} \\ \psi_{h4} \end{bmatrix} = \varepsilon \begin{bmatrix} \psi_{e3} \\ \psi_{e4} \\ \psi_{h3} \\ \psi_{h4} \end{bmatrix} \tag{5.47}$$

Let us first start with Eq. (5.60), the electron and hole parts of this equation can be decoupled. From the electron part,

$$-\mu\psi_{e1} + v_F(\pi_x - i\pi_y)\psi_{e2} = \varepsilon\psi_{e1} \tag{5.48a}$$

$$v_F(\pi_x + i\pi_y)\psi_{e1} - \mu\psi_{e2} = \varepsilon\psi_{e2} \tag{5.48b}$$

In case of uniform magnetic field, we have,

$$\mathbf{A} = \begin{cases} Bx\hat{y} \text{ , G region} \\ 0 \text{ , S region} \end{cases} \tag{5.49}$$

If we take $k_y = \frac{X}{l^2}$, then from Eq. (5.48), we get,

$$\left[\hat{p_x}^2 + \hbar eB + \left(\hbar\frac{X}{l^2} + eBx\right)^2\right]\psi_{e1} = \left(\frac{\varepsilon + \mu}{v_F}\right)^2 \psi_{e1} \tag{5.50}$$

Now, $\left(\hbar\frac{X}{l^2} + eBx\right) = \sqrt{\hbar eB}\left[\frac{X}{l} + \frac{x}{l}\right]$, where, $l = \sqrt{\frac{\hbar}{eB}}$ is the magnetic length. If we now measure length in the units of l and energy in the units of $\hbar v_F/l$,

$$x \to xl$$

$$X \to Xl$$

$$(\varepsilon + \mu) \to (\varepsilon + \mu) \times \frac{\hbar v_F}{l}$$

This makes Eq. (5.50) and the corresponding equation of ψ_{h1} describing the hole part,

$$\left[-\frac{1}{2}\partial_x^2+\frac{1}{2}(x+X)^2\right]\psi_{e1}=\frac{1}{2}\left[(\mu+\varepsilon)^2-1\right]\psi_{e1} \tag{5.51a}$$

$$\left[-\frac{1}{2}\partial_x^2+\frac{1}{2}(x-X)^2\right]\psi_{h1}=\frac{1}{2}\left[(\mu-\varepsilon)^2-1\right]\psi_{h1} \tag{5.51b}$$

The solutions of ψ_{e1} from Eq. (5.51a) of this equation is

$$\psi_{e1}=-i\left(\varepsilon+\mu\right)e^{-\frac{1}{2}(x+X)^2}H_{\frac{1}{2}(\varepsilon+\mu)^2-1}(x+X) \tag{5.52}$$

$$\psi_{e2}=e^{-\frac{1}{2}(x+X)^2}H_{\frac{1}{2}(\varepsilon+\mu)^2}(x+X) \tag{5.53}$$

The wavefunctions in the G region is written as,

$$\mathbf{\Psi}(x,y)=e^{ik_y y}\begin{pmatrix}C_e\otimes\Phi_e(x+X)\\C_h\otimes\Phi_h(x-X)\end{pmatrix} \tag{5.54}$$

where,

$$\Phi_e(\xi)=e^{-(1/2)\xi^2}\begin{pmatrix}-i(\mu+\varepsilon)H_{\frac{1}{2}(\varepsilon+\mu)^2-1}(\xi)\\H_{\frac{1}{2}(\varepsilon+\mu)^2}(\xi)\end{pmatrix} \tag{5.55}$$

$$\Phi_h(\xi)=e^{-(1/2)\xi^2}\begin{pmatrix}H_{\frac{1}{2}(\mu-\varepsilon)^2}(\xi)\\-i(\mu-\varepsilon)H_{\frac{1}{2}(\mu-\varepsilon)^2-1}(\xi)\end{pmatrix} \tag{5.56}$$

If we restrict our calculation to single valley, then the wavefunction $\Psi(x,y)=\begin{bmatrix}\psi_{e1} & \psi_{e2} & \psi_{h1} & \psi_{h2}\end{bmatrix}^T$ has two solutions in the graphene region.

$$\Psi_{G1}(x,y)=e^{ik_y y}e^{-(1/2)(x+X)^2}\begin{pmatrix}-i(\mu+\varepsilon)H_{\frac{1}{2}(\varepsilon+\mu)^2-1}(x+X)\\H_{\frac{1}{2}(\varepsilon+\mu)^2}(x+X)\\0\\0\end{pmatrix} \tag{5.57a}$$

$$\Psi_{G2}(x,y) = e^{ik_y y} e^{-(1/2)(x-X)^2} \begin{pmatrix} 0 \\ 0 \\ H_{\frac{1}{2}(\mu-\varepsilon)^2}(x-X) \\ -i(\mu-\varepsilon) H_{\frac{1}{2}(\mu-\varepsilon)^2-1}(x-X) \end{pmatrix} \tag{5.57b}$$

From Eq. (5.51a), we see that we have solution for this wavefunction for half integer values of $\frac{1}{2}\left[(\mu+\varepsilon)^2-1\right]$,

$$\frac{1}{2}\left[(\mu+\varepsilon)^2-1\right] = n_e + \frac{1}{2} \tag{5.58}$$

Here, $n_e = 0, 1, 2, ...$

Similarly from Eq. (5.51b), we see that we have solution for this wavefunction for half integer values of $\frac{1}{2}\left[(\mu-\varepsilon)^2-1\right]$,

$$\frac{1}{2}\left[(\mu-\varepsilon)^2-1\right] = n_h + \frac{1}{2} \tag{5.59}$$

Here, $n_h = 0, 1, 2, ...$

This shows that for every value of n_e and n_h we have two values of energy. Earlier for the case of non-relativistic two-dimensional electronic system discussed in Sec. 5.5, we had one energy for every values of n_e and n_h. This is a consequence of graphene's linear dispersion.

5.8.3 Solution in the Barrier region

In the earlier calculation of S-QH-S junctions in non relativistic two dimensional electronic system, we had taken the barrier potential in the units of $\hbar\omega_C$. Here we take the energies in the units of $\frac{\hbar v_F}{l}$. We have also scaled the external scattering potential accordingly. If we put a electrostatic potential barrier of height V_0 in the graphene region, then we can write the DBdG equation as

$$\begin{bmatrix} V_0-\mu & v_F(\pi_x-i\pi_y) & 0 & 0 \\ v_F(\pi_x+i\pi_y) & V_0-\mu & 0 & 0 \\ 0 & 0 & \mu-V_0 & -v_F(\bar{\pi}_x-i\bar{\pi}_y) \\ 0 & 0 & -v_F(\bar{\pi}_x+i\bar{\pi}_y) & \mu-V_0 \end{bmatrix} \begin{bmatrix} \psi_{e1} \\ \psi_{e2} \\ \psi_{h1} \\ \psi_{h2} \end{bmatrix} = \varepsilon \begin{bmatrix} \psi_{e1} \\ \psi_{e2} \\ \psi_{h1} \\ \psi_{h2} \end{bmatrix} \tag{5.60}$$

The counterparts of equations (5.51) becomes,

$$\left[-\frac{1}{2}\partial_x^2+\frac{1}{2}(x+X)^2\right]\psi_{e1}=\frac{1}{2}\left[(\mu+\varepsilon-V_0)^2-1\right]\psi_{e1} \tag{5.61a}$$

$$\left[-\frac{1}{2}\partial_x^2+\frac{1}{2}(x-X)^2\right]\psi_{h1}=\frac{1}{2}\left[(\mu-\varepsilon-V_0)^2-1\right]\psi_{h1} \tag{5.61b}$$

With this, the modified solutions in this region become,

$$\Psi_{B1}(x,y)=e^{ik_y y}e^{-(1/2)(x+X)^2}\begin{pmatrix} -i(\mu+\varepsilon-V_0)H_{\frac{1}{2}(\varepsilon-V_0+\mu)^2-1}(x+X) \\ H_{\frac{1}{2}(\varepsilon-V_0+\mu)^2}(x+X) \\ 0 \\ 0 \end{pmatrix} \tag{5.62a}$$

$$\Psi_{B2}(x,y)=e^{ik_y y}e^{-(1/2)(x-q)^2}\begin{pmatrix} 0 \\ 0 \\ H_{\frac{1}{2}(\mu-V_0-\varepsilon)^2}(x-q) \\ -i(\mu-V_0-\varepsilon)H_{\frac{1}{2}(\mu-V_0-\varepsilon)^2-1}(x-q) \end{pmatrix} \tag{5.62b}$$

In the superconducting region, we can write

$$\begin{bmatrix} -\mu - U_0 & v_F(p_x - ip_y) & \Delta_0 e^{i\Phi} & 0 \\ v_F(p_x + ip_y) & -\mu - U_0 & 0 & \Delta_0 e^{i\Phi} \\ \Delta_0 e^{-i\Phi} & 0 & \mu + U_0 & -v_F(p_x - ip_y) \\ 0 & \Delta_0 e^{-i\Phi} & -v_F(p_x + ip_y) & \mu + U_0 \end{bmatrix} \begin{bmatrix} \psi_{e1} \\ \psi_{e2} \\ \psi_{h1} \\ \psi_{h2} \end{bmatrix} = \varepsilon \begin{bmatrix} \psi_{e1} \\ \psi_{e2} \\ \psi_{h1} \\ \psi_{h2} \end{bmatrix} \tag{5.63}$$

Again, from Eq. (5.61a) and (5.61b), we have solutions for,

$$\frac{1}{2}\left[(\mu + \varepsilon - V_0)^2 - 1\right] = n_e + \frac{1}{2} \text{ and } \frac{1}{2}\left[(\mu - \varepsilon - V_0)^2 - 1\right] = n_h + \frac{1}{2} \tag{5.64}$$

5.8.4 Solution in Superconducting Region

Here, Φ is the superconducting phase. The possible solutions in the regime of $U_0 + \mu \gg \Delta_0, \varepsilon$ are given by

$$\psi_{S1}(\Phi) = e^{ik_y y + ik_o x - k_i x} \begin{pmatrix} e^{i\beta} \\ e^{i\beta + i\gamma} \\ e^{-i\Phi} \\ e^{-i\Phi + i\gamma} \end{pmatrix}, \tag{5.65a}$$

$$\psi_{S2}(\Phi) = e^{ik_y y + ik_o x + k_i x} \begin{pmatrix} e^{-i\beta} \\ e^{-i\beta + i\gamma} \\ e^{-i\Phi} \\ e^{-i\Phi + i\gamma} \end{pmatrix}, \tag{5.65b}$$

$$\psi_{S3}(\Phi) = e^{ik_y y - ik_o x - k_i x} \begin{pmatrix} e^{-i\beta} \\ -e^{-i\beta - i\gamma} \\ e^{-i\Phi} \\ -e^{-i\Phi - i\gamma} \end{pmatrix}, \tag{5.65c}$$

$$\psi_{S4}(\Phi) = e^{ik_y y - ik_o x + k_i x} \begin{pmatrix} e^{i\beta} \\ -e^{i\beta - i\gamma} \\ e^{-i\Phi} \\ -e^{-i\Phi - i\gamma} \end{pmatrix}. \tag{5.65d}$$

where,

$$\beta = \begin{cases} \cos^{-1}\left(\frac{\varepsilon}{\Delta_o}\right) & \text{if } \varepsilon < \Delta_o \\ -i\cosh^{-1}\left(\frac{\varepsilon}{\Delta_o}\right) & \text{if } \varepsilon > \Delta_o \end{cases} \tag{5.66}$$

$$\gamma = \sin^{-1}\left[\frac{\hbar v_F k_y}{U_o + \mu}\right] \tag{5.67}$$

$$k_o = \sqrt{\left(\frac{U_o + \mu}{\hbar v_F}\right)^2 - k_y^2} \tag{5.68}$$

$$k_i = \frac{(U_o + \mu)\Delta_o}{\hbar^2 v_F^2 k_o} \sin\beta \tag{5.69}$$

In the regime of $|k_y| \leq \frac{\mu}{\hbar v_F}$ and if we take $U_o \gg \mu, \varepsilon$ then, $\gamma \to 0$, $k_o \to \frac{U_o}{\hbar v_F}$ and $k_i \to \frac{\Delta_o}{\hbar v_F}\sin\beta$. In the region $x < 0$, (i.e.,left superconductor), the wavefunction is $\Psi_l = a_1\psi_2(\phi_1) + a_2\psi_4(\phi_1)$. In the region $x > L$, (i.e.,right superconductor) the wave-function is $\Psi_r = b_1\psi_1(\phi_2) + b_2\psi_3(\phi_2)$.

5.8.5 Boundary Value Condition

The transfer matrices are calculated using boundary value conditions in the same method we used earlier in set of equations Eq. (5.9) and (5.11) in Sec. 5.3. We match the wavefunctions Eq. (4.16) and (5.57)at the SG interface to get M_{SG}, the wavefunctions Eq. (5.57) and (5.62) at the GB interface to get M_{GB}, the wavefunctions Eq. (5.62) and (5.57) at the BG interface to get M_{BG} and the wavefunctions Eq. (5.57) and (4.16) at the GS interface to get M_{GS}. Now we construct the transfer matrix similar to Eq. (5.13)

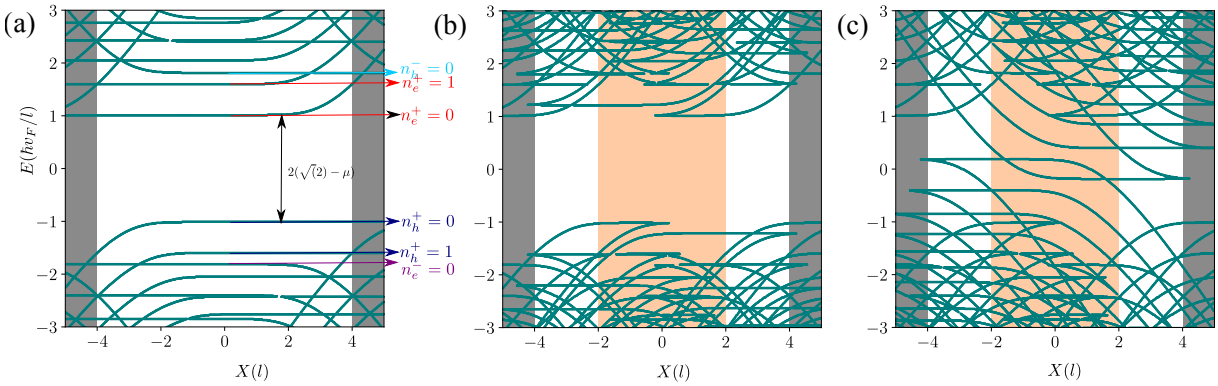

FIG. 5.8: (a) The dispersion of the monolayer graphene based SQHS junction with the separation between the two superconductors $2L = 8$, $\mu = 0.4$ and superconducting gap $\Delta_0 = 10$. Here we have measured the lengths in the units of magnetic length l and energies in the units of $\frac{\hbar v_F}{l}$. In (b) and (c) we show the dispersion for the same system when the electrostatic barrier of height (b) $V_0 = 0.2$ and (c) 2 is present in the QH region.

$$\mathcal{M} = \begin{bmatrix} M_{SG} & 0 & 0 & 0 \\ 0 & M_{GB} & 0 & 0 \\ 0 & 0 & M_{BG} & 0 \\ 0 & 0 & 0 & M_{GS} \end{bmatrix}. \tag{5.70}$$

We are not providing the explicit form of these matrices. As the graphene wavefunctions have four component, all the matrices in Eq. (5.70) are (4×4) matrices. The E - q dispersion in this case is given by

$$det(\mathcal{M}) = det(M_{SG})det(M_{GB})det(M_{BG})det(M_{GS}) = 0 \tag{5.71}$$

In FIG. 5.8, we show the dispersion which we obtained from the dispersion relation Eq. (5.71). In Eq. (5.71) (a) first we show the dispersion when the potential barrier is absent. We have marked the electron states n_e^+ and n_e^- and hole states n_h^+ and n_h^-. The $+$ and $-$ sign represent two solutions obtained from each value of n_e and n_h. In FIG. 5.8 (b) and (c) we show the dispersion when the barrier potential is present. The height of the barriers is taken as (b) $V_0 = 0.2$ and (c) $V_0 = 2$.

5.9 Conclusion and Future Scope

In this chapter we developed a transfer matrix based theoretical framework to study the effect of electrostatically defined barrier potential on a superconductor-quantum hall-superconductor junction(SQHS) Josephson junction. We studied both non-relativistic two dimensional electron system and graphene based SQHS junctions which show two different types of Landau Levels due to their different nature of dispersion. For the case of non-relativistic two dimensional electron system, we identified intermediate chiral edge states (ICES) which occur due to the presence of the barrier and identified its contribution to the Josephson conductivity. We have also extended our analysis to include the lattice effect when a large array of external barriers are present in the QH region. In graphene based SQHS junction we have obtained the dispersion. The framework we developed can also be extended for the case of graphene.

CHAPTER 6

Conclusions

This thesis has examined three interconnected problems in the scattering and transport of massless Dirac fermions (MDFs) in graphene and hybrid superconducting systems. Across these problems, we demonstrated how external electrostatic, magnetic, and periodic potentials provide powerful means of controlling electron dynamics, and established connections to optics, superconductivity, and quantum Hall physics.

In **Chapter 3**, based on [44], we studied the scattering of MDFs from two-dimensional quantum dot lattices (TDQDL). Using the Lippmann–Schwinger formalism in the first Born approximation, we showed that the differential scattering cross-section is proportional to the Fourier transform of the scattering potential, drawing a close analogy with Fraunhofer diffraction in optics [27]. While direct image reconstruction, as in optical Fourier optics, is not possible in graphene, we introduced the rotation angle between the incident wave and lattice symmetry as an additional degree of freedom. Analysis of angle-resolved dc-resistivity revealed that structural features such as lattice symmetry, defects, and moiré patterns leave distinct signatures in the resistivity spectrum. These results suggest a pathway toward electronic analogues of image processing and pattern recognition using graphene. Also, our work is first to show fractional Fourier transform in condensed matter system.

In **Chapter 4**, reported in [45], we investigated graphene-based Josephson junctions incorporating one-dimensional electrostatic and magnetic barriers as the weak link between superconducting electrodes. Josephson junctions are fundamental to superconducting electronics, providing dissipationless current flow that underpins applications from SQUID magnetometry to superconducting qubits [81, 82]. Using the Dirac–Bogoliubov–de Gennes (DBdG) formalism [29, 83], we showed that barrier regions act as tunable refractive index media for MDFs, with barrier strengths controlling the Andreev reflection process. With this our system show condensed matter analogues of both reflection and refraction in a two-dimensional system. This tunability directly modulates the Josephson current, demonstrating a mechanism for externally controlling superconducting transport in graphene-based devices.

In **Chapter 5**, we studied the effect of external electrostatic potential on superconductor–quantum Hall–superconductor (SQHS) Josephson junctions, where Landau quantization dominates the electronic states [75]. We developed a transfer-matrix framework and showed that local electrostatic barriers generate intermediate chiral edge states (ICES) [77, 78], which provide new current-carrying channels and significantly modify Josephson transport. Analysis of non-ideal interfaces further highlighted the sensitivity of transport to scattering, while extending the model to periodically modulated junctions revealed additional routes for controlling conductivity. These results emphasize the rich interplay between superconductivity and quantum Hall physics in hybrid graphene systems. We have studied both non-relativistic two-dimensional electron system and monolayer graphene based SQHS junctions. Due to their dispersion the nature of Landau levels show the signatures of these two systems.

Together, **Chapters 4 and 5** demonstrate the versatility of Josephson junctions as platforms for engineering superconducting transport in graphene. In Chapter 4, we showed that barrier engineering allows direct control over Josephson current, while in Chapter 5 we revealed how hybrid superconducting–quantum Hall junctions support novel current-carrying states. Both studies show the central role of Josephson junctions not only in fundamental physics but also in potential applications ranging from superconducting logic to quantum information processing.

In conclusion, this thesis demonstrates that the scattering of massless Dirac fermions in modulated graphene junctions controlled through engineered external electromagnetic potentials open up several possibilities of device application. The optical analogy of Chapter 3 illustrates how transport can reveal structural properties; the Josephson junction studies in Chapters 4 shows how barriers provide experimental knobs for controlling supercurrent; and the Chapters 5 highlights the emergence of novel edge states in hybrid systems. Beyond advancing theoretical understanding, these results point to practical routes for graphene-based **electronic imaging, superconducting device engineering, and quantum transport applications**, bridging the gap between fundamental condensed matter physics and emerging quantum technologies.

Bibliography

[1] M.-H. Liu, C. Gorini, and K. Richter, "Creating and steering highly directional electron beams in graphene", Phys. Rev. Lett. **118**, 066801 (2017).

[2] P. Bøggild, J. M. Caridad, C. Stampfer, et al., "A two-dimensional dirac fermion microscope", Nat. Commun. **8**, 15783 (2017).

[3] B. Brun, N. Moreau, S. Somanchi, et al., "Imaging dirac fermions flow through a circular veselago lens", Phys. Rev. B **100**, 041401 (2019).

[4] V. V. Cheianov, V. Fal'ko, and B. L. Altshuler, "The focusing of electron flow and a veselago lens in graphene p-n junctions", Science **315**, 1252–1255 (2007).

[5] S. Tchoumakov, J. Cayssol, and A. G. Grushin, "Three-dimensional chiral veselago lensing", Phys. Rev. B **105**, 075309 (2022).

[6] P. Rickhaus, P. Makk, M.-H. Liu, et al., "Gate tuneable beamsplitter in ballistic graphene", Appl. Phys. Lett. **107**, 251901 (2015).

[7] C.-H. Park, Y.-W. Son, L. Yang, et al., "Electron beam supercollimation in graphene superlattices", Nano Letters **8**, 2920–2924 (2008).

[8] M. S. Jang, H. Kim, Y.-W. Son, et al., "Graphene field effect transistor without an energy gap", Proc. Natl. Acad. Sci. U.S.A. **110**, 8786–8789 (2013).

[9] Q. Wilmart, S. Berrada, D. Torrin, et al., "A klein-tunneling transistor with ballistic graphene", 2D Mater. **1**, 011006 (2014).

[10] K. S. Novoselov, A. K. Geim, S. V. Morozov, et al., "Two-dimensional gas of massless dirac fermions in graphene", Nature **438**, 197–200 (2005).

[11] S. Chen, Z. Han, M. M. Elahi, et al., "Electron optics with p-n junctions in ballistic graphene", Science **353**, 1522–1525 (2016).

[12] G.-H. Lee, G.-H. Park, and H.-J. Lee, "Observation of negative refraction of dirac fermions in graphene", Nat. Phys. **11**, 925–929 (2015).

[13] T. Ohta, A. Bostwick, T. Seyller, et al., "Controlling the electronic structure of bilayer graphene", Science **313**, 951–954 (2006).

[14] R. L. Heinisch, F. X. Bronold, and H. Fehske, "Mie scattering analog in graphene: lensing, particle confinement, and depletion of klein tunneling", Phys. Rev. B **87**, 155409 (2013).

[15] D. S. Wei, T. van der Sar, J. D. Sanchez-Yamagishi, et al., "Mach-zehnder interferometry using spin-and valley-polarized quantum hall edge states in graphene", Sci. Adv. **3**, e1700600 (2017).

[16] M. Jo, P. Brasseur, A. Assouline, et al., "Quantum hall valley splitters and a tunable mach-zehnder interferometer in graphene", Phys. Rev. Lett. **126**, 146803 (2021).

[17] P. Rickhaus, R. Maurand, M.-H. Liu, et al., "Ballistic interferences in suspended graphene", Nat. Commun. **4**, 2342 (2013).

[18] G. Forghieri, P. Bordone, and A. Bertoni, "Time-dependent transport in graphene mach-zender interferometers", Phys. Rev. B **106**, 165402 (2022).

[19] C. Handschin, P. Makk, P. Rickhaus, et al., "Fabry-pérot resonances in a graphene/hbn moiré superlattice", Nano letters **17**, 328–333 (2017).

[20] V. V. Cheianov and V. I. Fal'ko, "Selective transmission of dirac electrons and ballistic magnetoresistance of $n-p$ junctions in graphene", Phys. Rev. B **74**, 041403 (2006).

[21] R. N. Sajjad, S. Sutar, J. U. Lee, et al., "Manifestation of chiral tunneling at a tilted graphene p-n junction", Phys. Rev. B **86**, 155412 (2012).

[22] F. Anwar, A. Iurov, D. Huang, et al., "Interplay between effects of barrier tilting and scatterers within a barrier on tunneling transport of dirac electrons in graphene", Phys. Rev. B **101**, 115424 (2020).

[23] D. PM, *L'intégrale de fourier et ses applications à l'optique* (1946).

[24] H. Levine and J. Schwinger, "On the theory of diffraction by an aperture in an infinite plane screen. i", Phys. Rev. **74**, 958–974 (1948).

[25] K. Birch, "A spatial frequency filter to remove zero frequency", Opt. Acta. **15**, 113–127 (1968).

[26] K. G. Birch, "Spatial filtering in optical data-processing", Rep. Prog. Phys. **35**, 1265 (1972).

[27] M. Born and E. Wolf, *Principles of optics: electromagnetic theory of propagation, interference and diffraction of light (7th edition)*, 7th (Cambridge University Press, 1999).

[28] F. Jenkins and H. White, *Fundamentals of optics*, International student edition (McGraw-Hill, 1976).

[29] M. Titov and C. W. J. Beenakker, "Josephson effect in ballistic graphene", Phys. Rev. B **74**, 041401 (2006).

[30] A. M. Black-Schaffer and S. Doniach, "Self-consistent solution for proximity effect and josephson current in ballistic graphene sns josephson junctions", Phys. Rev. B **78**, 024504 (2008).

[31] F. Arute, K. Arya, R. Babbush, et al., "Quantum supremacy using a programmable superconducting processor", Nature **574**, 505–510 (2019).

[32] A. D. Christianson, E. A. Goremychkin, R. Osborn, et al., "Unconventional superconductivity in $Ba_{0\cdot 6}K_{0\cdot 4}Fe_2As_2$ from inelastic neutron scattering", Nature **456**, 930–932 (2008).

[33] A. Wallraff, D. I. Schuster, A. Blais, et al., "Strong coupling of a single photon to a superconducting qubit using circuit quantum electrodynamics", Nature **431**, 162–167 (2004).

[34] M. A. Castellanos-Beltran and K. W. Lehnert, "Widely tunable parametric amplifier based on a superconducting quantum interference device array resonator", Appl. Phys. Lett. **91**, 083509 (2007).

[35] M. Bal, C. Deng, J.-L. Orgiazzi, et al., "Ultrasensitive magnetic field detection using a single artificial atom", Nature Communications **3**, 1324 (2012).

[36] A. Vettoliere, C. Granata, and R. Monaco, "Long josephson junction in ultralow-noise magnetometer configuration", IEEE Trans. Magn. **51**, 1–4 (2015).

[37] N. E. Frattini, U. Vool, S. Shankar, et al., "3-wave mixing josephson dipole element", Appl. Phys. Lett. **110**, 222603 (2017).

[38] N. E. Frattini, V. V. Sivak, A. Lingenfelter, et al., "Optimizing the nonlinearity and dissipation of a snail parametric amplifier for dynamic range", Phys. Rev. Appl. **10**, 054020 (2018).

[39] E. D. Walsh, W. Jung, G.-H. Lee, et al., "Josephson junction infrared single-photon detector", Science **372**, 409–412 (2021).

[40] A. Shailos, W. Nativel, A. Kasumov, et al., "Proximity effect and multiple andreev reflections in few-layer graphene", Europhys. Lett. **79**, 57008 (2007).

[41] G.-H. Lee and H.-J. Lee, "Proximity coupling in superconductor-graphene heterostructures", Rep. Prog. Phys. **81**, 056502 (2018).

[42] L. Bretheau, J. I.-J. Wang, R. Pisoni, et al., "Tunnelling spectroscopy of andreev states in graphene", Nature Physics **13**, 756–760 (2017).

[43] C. Li, S. Guéron, A. Chepelianskii, et al., "Full range of proximity effect probed with superconductor/graphene/superconductor junctions", Phys. Rev. B **94**, 115405 (2016).

[44] P. S. Banerjee, R. Marathe, and S. Ghosh, "Electronic analogue of fourier optics with massless dirac fermions scattered by quantum dot lattice", J. Opt. **26**, 095602 (2024).

[45] P. S. Banerjee, R. Marathe, and S. Ghosh, "Magnetically modulated superconductor-graphene-superconductor (sgs) josephson junctions and their tunability", Phys. Scr. **100**, 015965 (2024).

[46] P. G. Silvestrov and K. B. Efetov, "Quantum dots in graphene", Phys. Rev. Lett. **98**, 016802 (2007).

[47] D. Joung, L. Zhai, and S. I. Khondaker, "Coulomb blockade and hopping conduction in graphene quantum dots array", Phys. Rev. B **83**, 115323 (2011).

[48] J. Lee, D. Wong, J. Velasco Jr, et al., "Imaging electrostatically confined dirac fermions in graphene quantum dots", Nat. Phys. **12**, 1032–1036 (2016).

[49] F. Ghahari, D. Walkup, C. Gutiérrez, et al., "An on/off berry phase switch in circular graphene resonators", Science **356**, 845–849 (2017).

[50] C. Gutiérrez, D. Walkup, F. Ghahari, et al., "Interaction-driven quantum hall wedding cake–like structures in graphene quantum dots", Science **361**, 789–794 (2018).

[51] Y. Ren, Y. Gao, P. Wan, et al., "Effective medium theory for electron waves in a gate-defined quantum dot array in graphene", Phys. Rev. B **100**, 045422 (2019).

[52] H. V. Grushevskaya, G. G. Krylov, S. P. Kruchinin, et al., "Electronic properties and quasi-zero-energy states of graphene quantum dots", Phys. Rev. B **103**, 235102 (2021).

[53] Y. Zhao, J. Wyrick, F. D. Natterer, et al., "Creating and probing electron whispering-gallery modes in graphene", Science **348**, 672–675 (2015).

[54] R. Zhao, P. Wan, L. Zhou, et al., "Electron metasurfaces in graphene", Phys. Rev. B **107**, 155404 (2023).

[55] Y. Tang, X. Cao, R. Guo, et al., "Flat-lens focusing of electron beams in graphene", Scientific Reports **6**, 33522 (2016).

[56] A. F. Young and P. Kim, "Quantum interference and klein tunnelling in graphene heterojunctions", Nature Physics **5**, 222–226 (2009).

[57] M. I. Katsnelson, K. S. Novoselov, and A. K. Geim, "Chiral tunnelling and the klein paradox in graphene", Nat. Phys. **2**, 620–625 (2006).

[58] P. E. Allain and J.-N. Fuchs, "Klein tunneling in graphene: optics with massless electrons", Eur. Phys. J. B **83**, 301–317 (2011).

[59] A. De Martino, L. Dell'Anna, and R. Egger, "Magnetic barriers and confinement of dirac–weyl quasiparticles in graphene", Solid State Commun. **144**, 547–550 (2007).

[60] A. De Martino, L. Dell'Anna, and R. Egger, "Magnetic confinement of massless dirac fermions in graphene", Phys. Rev. Lett. **98**, 066802 (2007).

[61] L. Oroszlány, P. Rakyta, A. Kormányos, et al., "Theory of snake states in graphene", Phys. Rev. B **77**, 081403 (2008).

[62] M. R. Masir, P. Vasilopoulos, and F. M. Peeters, "Kronig–penney model of scalar and vector potentials in graphene", J. Phys.: Condens. Matter **22**, 465302 (2010).

[63] S. Ghosh and M. Sharma, "Electron optics with magnetic vector potential barriers in graphene", J. Phys.: Condens. Matter **21**, 292204 (2009).

[64] F. B. Mancoff, R. M. Clarke, C. M. Marcus, et al., "Magnetotransport of a two-dimensional electron gas in a spatially random magnetic field", Phys. Rev. B **51**, 13269–13273 (1995).

[65] V. Kubrak, F. Rahman, B. L. Gallagher, et al., "Magnetoresistance of a two-dimensional electron gas due to a single magnetic barrier and its use for nanomagnetometry", Appl. Phys. Lett. **74**, 2507–2509 (1999).

[66] J. Q. You, L. Zhang, and P. K. Ghosh, "Electronic transport in nanostructures consisting of magnetic barriers", Phys. Rev. B **52**, 17243–17247 (1995).

[67] E. Cobas, A. L. Friedman, O. M. J. van't Erve, et al., "Graphene as a tunnel barrier: graphene-based magnetic tunnel junctions", Nano Lett. **12**, 3000–3004 (2012).

[68] J. Meng, J.-J. Chen, Y. Yan, et al., "Vertical graphene spin valve with ohmic contacts", Nanoscale **5**, 8894–8898 (2013).

[69] J.-J. Chen, J. Meng, Y.-B. Zhou, et al., "Layer-by-layer assembly of vertically conducting graphene devices", Nat. Commun. **4**, 1921 (2013).

[70] E. C. Peters, E. J. H. Lee, M. Burghard, et al., "Gate dependent photocurrents at a graphene p-n junction", Appl. Phys. Lett. **97**, 193102 (2010).

[71] N. Stander, B. Huard, and D. Goldhaber-Gordon, "Evidence for klein tunneling in graphene $p-n$ junctions", Phys. Rev. Lett. **102**, 026807 (2009).

[72] J. R. Williams, L. DiCarlo, and C. M. Marcus, "Quantum hall effect in a gate-controlled p-n junction of graphene", Science **317**, 638–641 (2007).

[73] M. R. Masir, P. Vasilopoulos, and F. M. Peeters, "Magnetic kronig–penney model for dirac electrons in single-layer graphene", New J. Phys. **11**, 095009 (2009).

[74] V. Q. Le, C. H. Pham, and V. L. Nguyen, "Magnetic kronig–penney-type graphene superlattices: finite energy dirac points with anisotropic velocity renormalization", J. Phys.: Condens. Matter **24**, 345502 (2012).

[75] H. Hoppe, U. Zülicke, and G. Schön, "Andreev reflection in strong magnetic fields", Phys. Rev. Lett. **84**, 1804–1807 (2000).

[76] L. Landau, "Diamagnetismus der metalle", Z. Phys. **64**, 629–637 (1930).

[77] B. I. Halperin, "Quantized hall conductance, current-carrying edge states, and the existence of extended states in a two-dimensional disordered potential", Phys. Rev. B **25**, 2185–2190 (1982).

[78] D. B. Chklovskii, B. I. Shklovskii, and L. I. Glazman, "Electrostatics of edge channels", Phys. Rev. B **46**, 4026–4034 (1992).

[79] G. E. Blonder, M. Tinkham, and T. M. Klapwijk, "Transition from metallic to tunneling regimes in superconducting microconstrictions: excess current, charge imbalance, and supercurrent conversion", Phys. Rev. B **25**, 4515–4532 (1982).

[80] T.-C. Huang, W.-H. Wu, M.-T. Wu, et al., "Realizing high-quality interfaces in two-dimensional material spin valves", ACS Mater. Lett. **6**, 94–99 (2024).

[81] B. D. Josephson, "Possible new effects in superconductive tunnelling", Phys. Lett. **1**, 251–253 (1962).

[82] J. R. Waldram, A. B. Pippard, and J. Clarke, "Theory of the current-voltage characteristics of sns junctions and other superconducting weak links", Phil. Trans. R. Soc. A **268**, 265–287 (1970).

[83] C. W. J. Beenakker, "Specular andreev reflection in graphene", Phys. Rev. Lett. **97**, 067007 (2006).

[84] P. de Gennes, *Superconductivity of metals and alloys*, Advanced book classics (W.A. Benjamin, 1966).

[85] M. Maiti and K. Sengupta, "Josephson effect in graphene superconductor/barrier/superconductor junctions: oscillatory behavior of the josephson current", Phys. Rev. B **76**, 054513 (2007).

[86] A. R. Akhmerov and C. W. J. Beenakker, "Detection of valley polarization in graphene by a superconducting contact", Phys. Rev. Lett. **98**, 157003 (2007).

[87] F. Giazotto, M. Governale, U. Zülicke, et al., "Andreev reflection and cyclotron motion at superconductor—normal-metal interfaces", Phys. Rev. B **72**, 054518 (2005).

[88] M. Büttiker, "Absence of backscattering in the quantum hall effect in multiprobe conductors", Phys. Rev. B **38**, 9375–9389 (1988).

[89] B. A. Lippmann and J. Schwinger, "Variational principles for scattering processes. i", Phys. Rev. **79**, 469–480 (1950).

[90] J. J. Sakurai, *Modern quantum mechanics*, Rev. ed (Addison-Wesley Pub. Co, 1994).

[91] P. Strange, *Relativistic quantum mechanics: with applications in condensed matter and atomic physics* (Cambridge University Press, 1998).

[92] F. W. Olver, D. W. Lozier, R. F. Boisvert, et al., *Nist handbook of mathematical functions hardback and cd-rom* (Cambridge university press, 2010).

[93] T. M. Radchenko, A. A. Shylau, I. V. Zozoulenko, et al., "Effect of charged line defects on conductivity in graphene: numerical kubo and analytical boltzmann approaches", Phys. Rev. B **87**, 195448 (2013).

[94] R. G. Newton, *Scattering theory of waves and particles* (Springer Science & Business Media, 2013).

[95] I. R. Lapidus, "Quantum-mechanical scattering in two dimensions", American Journal of Physics **50**, 45–47 (1982).

[96] S. K. Adhikari, "Quantum scattering in two dimensions", American Journal of Physics **54**, 362–367 (1986).

[97] A. Ferreira, J. Viana-Gomes, J. Nilsson, et al., "Unified description of the dc conductivity of monolayer and bilayer graphene at finite densities based on resonant scatterers", Phys. Rev. B **83**, 165402 (2011).

[98] M. I. Katsnelson, *The physics of graphene*, 2nd ed. (Cambridge University Press, 2020).

[99] W. L. McMillan, "Theory of superconductor—normal-metal interfaces", Phys. Rev. **175**, 559–568 (1968).

[100] H. Suzuura and T. Ando, "Crossover from symplectic to orthogonal class in a two-dimensional honeycomb lattice", Phys. Rev. Lett. **89**, 266603 (2002).

[101] A. Andreev, "Thermal conductivity of the intermediate state of superconductors ii", Sov. Phys. JETP **20**, 1490 (1965).

[102] J. Demers and A. Griffin, "Scattering and tunneling of electronic excitations in the intermediate state of superconductors", Canadian Journal of Physics **49**, 285–295 (1971).

[103] F. Dolcini, "Andreev reflection", Lecture Notes for XXIII Physics GradDays **5**, 9 (2009).

[104] M. Katsnelson, K. Novoselov, and A. Geim, "Chiral tunnelling and the klein paradox in graphene", Nat. Phys. **2**, 620–625 (2006).

[105] J. B. Pendry, "Negative refraction makes a perfect lens", Phys. Rev. Lett. **85**, 3966–3969 (2000).

[106] D. Schurig, J. J. Mock, B. J. Justice, et al., "Metamaterial electromagnetic cloak at microwave frequencies", Science **314**, 977–980 (2006).

[107] X. Zhang, W. Ren, E. Bell, et al., "Gate-tunable veselago interference in a bipolar graphene microcavity", Nat Commun **13**, 6711 (2022).

[108] K. Wang, M. M. Elahi, L. Wang, et al., "Graphene transistor based on tunable dirac fermion optics", Proc. Natl. Acad. Sci. U.S.A. **116**, 6575–6579 (2019).

[109] E. Paredes-Rocha, Y. Betancur-Ocampo, N. Szpak, et al., "Gradient-index electron optics in graphene $p - n$ junctions", Phys. Rev. B **103**, 045404 (2021).

[110] M. Sharma and S. Ghosh, "Electron transport and goos–hänchen shift in graphene with electric and magnetic barriers: optical analogy and band structure", J. Phys.: Condens. Matter **23**, 055501 (2011).

[111] M. Karalic, A. Štrkalj, M. Masseroni, et al., "Electron-hole interference in an inverted-band semiconductor bilayer", Phys. Rev. X **10**, 031007 (2020).

[112] P. M. Duffieux, "The fourier transform and its applications to optics", The Fourier Transform and Its Applications to Optics by PM Duffieux New York (1983).

[113] A. Ghatak, *Optics* (Tata McGraw-Hill Publishing Company Limited, 2009).

[114] J. Goodman, *Introduction to fourier optics*, McGraw-Hill physical and quantum electronics series (W. H. Freeman, 2005).

[115] P. Silvestrov and K. Efetov, "Quantum dots in graphene", Phys. Rev. Lett. **98**, 016802 (2007).

[116] D. Joung, L. Zhai, and S. I. Khondaker, "Coulomb blockade and hopping conduction in graphene quantum dots array", Phys. Rev. B **83**, 115323 (2011).

[117] H. V. Grushevskaya, G. G. Krylov, S. P. Kruchinin, et al., "Electronic properties and quasi-zero-energy states of graphene quantum dots", Phys. Rev. B **103**, 235102 (2021).

[118] J. Lee, D. Wong, J. Velasco Jr, et al., "Imaging electrostatically confined dirac fermions in graphene quantum dots", Nat. Phys. **12**, 1032–1036 (2016).

[119] S.-Y. Li and L. He, "Recent progresses of quantum confinement in graphene quantum dots", Front. Phys. **17**, 1–25 (2022).

[120] R. Zhao, P. Wan, L. Zhou, et al., "Electron metasurfaces in graphene", Phys. Rev. B **107**, 155404 (2023).

[121] K. S. Novoselov, A. K. Geim, S. V. Morozov, et al., "Electric field effect in atomically thin carbon films", Science **306**, 666–669 (2004).

[122] A. C. Neto, F. Guinea, N. M. Peres, et al., "The electronic properties of graphene", Rev. Mod. Phys. **81**, 109 (2009).

[123] S. Bhandari, G. H. Lee, K. Watanabe, et al., "Imaging electron flow from collimating contacts in graphene", 2D Materials **5**, 021003 (2018).

[124] C. Gutiérrez, L. Brown, C.-J. Kim, et al., "Klein tunnelling and electron trapping in nanometre-scale graphene quantum dots", Nature Physics **12**, 1069–1075 (2016).

[125] S. Bhandari, G.-H. Lee, A. Klales, et al., "Imaging cyclotron orbits of electrons in graphene", Nano Letters **16**, PMID: 26845290, 1690–1694 (2016).

[126] J. Berezovsky and R. M. Westervelt, "Imaging coherent transport in graphene (part ii): probing weak localization", Nanotechnology **21**, 274014 (2010).

[127] C. Dartora, F. Zanella, and G. Cabrera, "The theory for a 2d electron diffractometer using graphene", J. Appl. Phys. **132**, 124305 (2022).

[128] C. R. Dean, A. F. Young, I. Meric, et al., "Boron nitride substrates for high-quality graphene electronics", Nature Nanotechnology **5**, 722–726 (2010).

[129] S. Bhandari, G. H. Lee, K. Watanabe, et al., "Imaging electron flow from collimating contacts in graphene", 2D Materials **5**, 021003 (2018).

[130] G.-H. Lee, G.-H. Park, and H.-J. Lee, "Observation of negative refraction of dirac fermions in graphene", Nature Physics **11**, 925–929 (2015).

[131] J. Martin, N. Akerman, G. Ulbricht, et al., "Observation of electron–hole puddles in graphene using a scanning single-electron transistor", Nature Physics **4**, 144–148 (2008).

[132] C. H. Lewenkopf and E. R. Mucciolo, "The recursive green's function method for graphene", Journal of Computational Electronics **12**, 203–231 (2013).

[133] S. Datta, *Electronic transport in mesoscopic systems* (Cambridge University Press, 1997).

[134] F. Ghahari, D. Walkup, C. Gutiérrez, et al., "An on/off berry phase switch in circular graphene resonators", Science **356**, 845–849 (2017).

[135] C. Gutiérrez, D. Walkup, F. Ghahari, et al., "Interaction-driven quantum hall wedding cake like structures in graphene quantum dots", Science **361**, 789–794 (2018).

[136] T. Hensgens, T. Fujita, L. Janssen, et al., "Quantum simulation of a fermi–hubbard model using a semiconductor quantum dot array", Nature **548**, 70–73 (2017).

[137] J. Salfi, J. Mol, R. Rahman, et al., "Quantum simulation of the hubbard model with dopant atoms in silicon", Nat Commun **7**, 11342 (2016).

[138] P. G. Averbuch, "Zero energy divergence of scattering cross sections in two dimensions", J. Phys. A **19**, 2325 (1986).

[139] H. Zoubi and G. C. La Rocca, "Exciton-polariton kinematic interactions in organic microcavities", Phys. Rev. B **72**, 125306 (2005).

[140] V. Ngampruetikorn and J. A. Sauls, "Impurity-induced anomalous thermal hall effect in chiral superconductors", Phys. Rev. Lett. **124**, 157002 (2020).

[141] D. S. Petrov and G. V. Shlyapnikov, "Interatomic collisions in a tightly confined bose gas", Phys. Rev. A **64**, 012706 (2001).

[142] P. A. e. a. Murthy, "Observation of the berezinskii–kosterlitz–thouless phase transition in an ultracold fermi gas", Phys. Rev. Lett. **115**, 010401 (2015).

[143] J. Babinet, *Mémoires d'optique météorologique*, Vol. 4 (1837), pp. 638–648.

[144] J. R. Jiménez and E. Hita, "Babinet's principle in scalar theory of diffraction", Optical Review **8**, 495–497 (2001).

[145] A. Dunbrack and J. Cano, "Intrinsically multilayer moiré heterostructures", Phys. Rev. B **107**, 235425 (2023).

[146] O. Can, T. Tummuru, R. P. Day, et al., "High-temperature topological superconductivity in twisted double-layer copper oxides", Nature Physics **17**, 519–524 (2021).

[147] J. M. B. Lopes dos Santos, N. M. R. Peres, and A. H. Castro Neto, "Graphene bilayer with a twist: electronic structure", Phys. Rev. Lett. **99**, 256802 (2007).

[148] S. Carr, S. Fang, and E. Kaxiras, "Electronic-structure methods for twisted moiré layers", Nature Reviews Materials **5**, 748–763 (2020).

[149] R. Bracewell, *Two-dimensional imaging*, Prentice-Hall signal processing series (Prentice Hall, 1995).

[150] E. Bar-Ziv, "Effect of diffraction on the moiré image. i. theory", J. Opt. Soc. Am. A **2**, 371–379 (1985).

[151] A. A. Ushkov, I. Verrier, T. Kampfe, et al., "Subwavelength diffraction gratings with macroscopic moiré patterns generated via laser interference lithography", Opt. Express **28**, 16453–16468 (2020).

[152] R. Bistritzer and A. H. MacDonald, "Moiré bands in twisted double-layer graphene", Proceedings of the National Academy of Sciences **108**, 12233–12237 (2011).

[153] K. Kim, A. DaSilva, S. Huang, et al., "Tunable moiré bands and strong correlations in small-twist-angle bilayer graphene", Proceedings of the National Academy of Sciences **114**, 3364–3369 (2017).

[154] H. Yoo, R. Engelke, S. Carr, et al., "Atomic and electronic reconstruction at the van der waals interface in twisted bilayer graphene", Nature Materials **18**, 448–453 (2019).

[155] G. Tarnopolsky, A. J. Kruchkov, and A. Vishwanath, "Origin of magic angles in twisted bilayer graphene", Phys. Rev. Lett. **122**, 106405 (2019).

[156] D. Aggarwal, R. Narula, and S. Ghosh, "A primer on twistronics: a massless dirac fermion's journey to moiré patterns and flat bands in twisted bilayer graphene", Journal of Physics: Condensed Matter **35**, 143001 (2023).

[157] M. Saxena, G. Eluru, and S. S. Gorthi, "Structured illumination microscopy", Adv. Opt. Photon. **7**, 241–275 (2015).

[158] F. Ströhl and C. F. Kaminski, "Frontiers in structured illumination microscopy", Optica **3**, 667–677 (2016).

[159] A. Classen, J. von Zanthier, M. O. Scully, et al., "Superresolution via structured illumination quantum correlation microscopy", Optica **4**, 580–587 (2017).

[160] S. Zhou, Y. Fu, X. Tang, et al., "Fourier-based analysis of moiré fringe patterns of superposed gratings in alignment of nanolithography", Opt. Express **16**, 7869–7880 (2008).

[161] L. Kong, S. Cai, Z. Li, et al., "Interpretation of moiré phenomenon in the image domain", Opt. Express **19**, 18399–18409 (2011).

[162] O. Bryngdahl, "Moiré: formation and interpretation", J. Opt. Soc. Am. **64**, 1287–1294 (1974).

[163] J.-H. Chen, C. Jang, S. Xiao, et al., "Intrinsic and extrinsic performance limits of graphene devices on SiO_2", Nature Nanotech **3**, 206–209 (2008).

[164] O. Balci and C. Kocabas, "Rapid thermal annealing of graphene-metal contact", Applied Physics Letters **101**, 243105 (2012).

[165] F. Giubileo and A. Di Bartolomeo, "The role of contact resistance in graphene field-effect devices", Progress in Surface Science **92**, 143–175 (2017).

[166] X. Wang, E. Khatami, F. Fei, et al., "Experimental realization of an extended fermi-hubbard model using a 2d lattice of dopant-based quantum dots", Nat Commun **13**, 6824 (2022).

[167] D. Schröer, A. D. Greentree, L. Gaudreau, et al., "Electrostatically defined serial triple quantum dot charged with few electrons", Phys. Rev. B **76**, 075306 (2007).

[168] F. Arute, K. Arya, R. Babbush, et al., "Quantum supremacy using a programmable superconducting processor", Nature **574**, 505–510 (2019).

[169] A. Wallraff, D. I. Schuster, A. Blais, et al., "Strong coupling of a single photon to a superconducting qubit using circuit quantum electrodynamics", Nature **431**, 162–167 (2004).

[170] J. Q. You, J. S. Tsai, and F. Nori, "Scalable quantum computing with josephson charge qubits", Phys. Rev. Lett. **89**, 197902 (2002).

[171] A. Vettoliere, C. Granata, and R. Monaco, "Long josephson junction in ultralow-noise magnetometer configuration", IEEE Trans. Magn. **51**, 1–4 (2015).

[172] N. Frattini, U. Vool, S. Shankar, et al., "3-wave mixing josephson dipole element", Appl. Phys. Lett. **110** (2017).

[173] N. E. Frattini, V. V. Sivak, A. Lingenfelter, et al., "Optimizing the nonlinearity and dissipation of a snail parametric amplifier for dynamic range", Phys. Rev. Appl. **10**, 054020 (2018).

[174] E. D. Walsh, W. Jung, G.-H. Lee, et al., "Josephson junction infrared single-photon detector", Science **372**, 409–412 (2021).

[175] C. S. Lim, J. D. Leslie, H. J. T. Smith, et al., "Temperature variation of the dc josephson current in pb-pb tunnel junctions", Phys. Rev. B **2**, 1651–1656 (1970).

[176] J. Yoshida, H. Katsuno, K. Nakayama, et al., "Current transport and the fluctuation of critical current in high-temperature superconductor interface-engineered josephson junctions", Phys. Rev. B **70**, 054511 (2004).

[177] J. M. Kivioja, T. E. Nieminen, J. Claudon, et al., "Weak coupling josephson junction as a current probe: effect of dissipation on escape dynamics", New J. Phys. **7**, 179 (2005).

[178] M. Cyster, J. Smith, N. Vogt, et al., "Simulating the fabrication of aluminium oxide tunnel junctions", npj Quantum Inf. **7**, 12 (2021).

[179] Y. Makhlin, G. Schön, and A. Shnirman, "Quantum-state engineering with josephson-junction devices", Rev. Mod. Phys. **73**, 357–400 (2001).

[180] G. Wendin and V. S. Shumeiko, "Quantum bits with Josephson junctions (Review Article)", Low Temp. Phys. **33**, 724–744 (2007).

[181] O. Cakir and I. O. Kulik, "Josephson effect in superconductive sns heterostructures with barriers", Phys. Rev. B **67**, 174514 (2003).

[182] A. A. Golubov, M. Y. Kupriyanov, and E. Il'ichev, "The current-phase relation in josephson junctions", Rev. Mod. Phys. **76**, 411–469 (2004).

[183] I. O. Kulik, "Macroscopic quantization and the proximity effect in sns junctions", Sov. Phys. JETP **30**, 944 (1969).

[184] C. Nguyen, J. Werking, H. Kroemer, et al., "Inas-alsb quantum well as superconducting weak link with high critical current density", Appl. Phys. Lett. **57**, 87–89 (1990).

[185] J. Nitta, T. Akazaki, H. Takayanagi, et al., "Transport properties in an inas-inserted-channel $In_{0.52}Al_{0.48}As/In_{0.53}Ga_{0.47}As$ heterostructure coupled superconducting junction", Phys. Rev. B **46**, 14286–14289 (1992).

[186] M. Salehi, M. Alidoust, Y. Rahnavard, et al., "Thermal transport properties of graphene-based ferromagnetic/singlet superconductor/ferromagnetic junctions", J. Appl. Phys. **107**, 123916 (2010).

[187] J. Linder, T. Yokoyama, D. Huertas-Hernando, et al., "Supercurrent switch in graphene π junctions", Phys. Rev. Lett. **100**, 187004 (2008).

[188] L. Bretheau, J. I.-J. Wang, R. Pisoni, et al., "Tunnelling spectroscopy of andreev states in graphene", Nat. Phys. **13**, 756–760 (2017).

[189] S. Park, W. Lee, S. Jang, et al., "Steady floquet–andreev states in graphene josephson junctions", Nature **603**, 421–426 (2022).

[190] C.-S. Huang, "Phase dependence of thermal transport in graphene josephson junctions", Phys. Rev. B **108**, 195433 (2023).

[191] G.-H. Park, W. Lee, S. Park, et al., "Controllable andreev bound states in bilayer graphene josephson junctions from short to long junction limits", Phys. Rev. Lett. **132**, 226301 (2024).

[192] A. Andreev, "The thermal conductivity of the intermediate state in superconductors", Zh. Eksp. Teor. Fiz. **46**, 1823–1828 (1964).

[193] A. H. Castro Neto, F. Guinea, N. M. R. Peres, et al., "The electronic properties of graphene", Rev. Mod. Phys. **81**, 109–162 (2009).

[194] K. S. Novoselov, A. K. Geim, S. V. Morozov, et al., "Two-dimensional gas of massless dirac fermions in graphene", Nature **438**, 197–200 (2005).

[195] Y. Zhang, Y.-W. Tan, H. L. Stormer, et al., "Experimental observation of the quantum hall effect and berry's phase in graphene", Nature **438**, 201–204 (2005).

[196] E. McCann and M. Koshino, "The electronic properties of bilayer graphene", Rep. Prog. Phys. **76**, 056503 (2013).

[197] A. De Martino, L. Dell'Anna, and R. Egger, "Magnetic confinement of massless dirac fermions in graphene", Phys. Rev. Lett. **98**, 066802 (2007).

[198] M. R. Masir, P. Vasilopoulos, and F. M. Peeters, "Magnetic kronig–penney model for dirac electrons in single-layer graphene", New J. Phys. **11**, 095009 (2009).

[199] H. B. Heersche, P. Jarillo-Herrero, J. B. Oostinga, et al., "Bipolar supercurrent in graphene", Nature **446**, 56–59 (2007).

[200] X. Du, I. Skachko, and E. Y. Andrei, "Josephson current and multiple andreev reflections in graphene sns junctions", Phys. Rev. B **77**, 184507 (2008).

[201] F. Miao, W. Bao, H. Zhang, et al., "Premature switching in graphene josephson transistors", Solid State Commun. **149**, 1046–1049 (2009).

[202] C. Ojeda-Aristizabal, M. Ferrier, S. Guéron, et al., "Tuning the proximity effect in a superconductor-graphene-superconductor junction", Phys. Rev. B **79**, 165436 (2009).

[203] D. Jeong, J.-H. Choi, G.-H. Lee, et al., "Observation of supercurrent in pbin-graphene-pbin josephson junction", Phys. Rev. B **83**, 094503 (2011).

[204] J. Evetts and J. Wade, "Superconducting properties and the phase diagrams of the Pb Bi and Pb In alloy systems", J. Phys. Chem. Solids **31**, 973–982 (1970).

[205] N. M. R. Peres, "Colloquium: the transport properties of graphene: an introduction", Reviews of Modern Physics **82**, 2673–2700 (2010).

[206] S. Das Sarma, S. Adam, E. H. Hwang, et al., "Electronic transport in two-dimensional graphene", Reviews of Modern Physics **83**, 407–470 (2011).

[207] C. W. J. Beenakker, "Random-matrix theory of quantum transport", Reviews of Modern Physics **69**, 731–808 (1997).

[208] A. Matulis, F. M. Peeters, and P. Vasilopoulos, "Wave-vector-dependent tunneling through magnetic barriers", Phys. Rev. Lett. **72**, 1518–1521 (1994).

[209] A. Majumdar, "Effects of intrinsic spin on electronic transport through magnetic barriers", Phys. Rev. B **54**, 11911–11913 (1996).

[210] T. Fujita, M. B. A. Jalil, and S. G. Tan, "Valley filter in strain engineered graphene", Appl. Phys. Lett. **97**, 043508 (2010).

[211] A. K. Singh, A. K. Singh, and S. R. P. Sinha, "Fermi-level modulation of chemical vapor deposition-grown monolayer graphene via nanoparticles to macromolecular dopants", ACS Omega **7**, 744–751 (2022).

[212] S. Kim, I. Jo, D. C. Dillen, et al., "Direct measurement of the fermi energy in graphene using a double-layer heterostructure", Phys. Rev. Lett. **108**, 116404 (2012).

[213] A. F. Young and P. Kim, "Quantum interference and klein tunnelling in graphene heterojunctions", Nature Physics **5**, 222–226 (2009).

[214] A. F. Young and P. Kim, "Electronic transport in graphene heterostructures", Annual Review of Condensed Matter Physics **2**, 101–120 (2011).

[215] B. Huard, J. A. Sulpizio, N. Stander, et al., "Transport measurements across a tunable potential barrier in graphene", Physical Review Letters **98**, 236803 (2007).

[216] E. Paredes-Rocha, Y. Betancur-Ocampo, N. Szpak, et al., "Gradient-index electron optics in graphene p-n junctions", Physical Review B **103**, 045404 (2021).

[217] K. S. Novoselov, A. K. Geim, S. V. Morozov, et al., "Electric field effect in atomically thin carbon films", Science **306**, 666–669 (2004).

[218] M. Tinkham, *Introduction to superconductivity* (Courier Corporation, 2004).

[219] J. J. Sakurai and J. Napolitano, *Modern quantum mechanics* (Cambridge University Press, 2020).

[220] V. Lukose, R. Shankar, and G. Baskaran, "Novel electric field effects on landau levels in graphene", Phys. Rev. Lett. **98**, 116802 (2007).

[221] L. Z. Tan, C.-H. Park, and S. G. Louie, "Graphene dirac fermions in one-dimensional inhomogeneous field profiles: transforming magnetic to electric field", Phys. Rev. B **81**, 195426 (2010).

[222] S. Salim, R. Marathe, and S. Ghosh, "Revisiting andreev processes in superconductor-graphene-superconductor (sgs) josephson junctions: comparison with experimental results", Phys. Scr. **98**, 065935 (2023).

[223] A. Zagoskin, *Quantum theory of many-body systems: techniques and applications*, Graduate Texts in Contemporary Physics (Springer New York, 2012).

[224] W. C. Stewart, "Current-voltage characteristics of josephson junctions", Applied Physics Letters **12**, 277 (1968).

[225] D. E. McCumber, "Effect of ac impedance on dc voltage-current characteristics of superconductor weak-link junctions", Journal of Applied Physics **39**, 3113 (1968).

[226] A. Franz, Y. Koval, D. Vasyukov, et al., "Thermal fluctuations in ultrasmall intrinsic josephson junctions", Physical Review B **69**, 014506 (2004).

[227] P. T. Araujo, M. Terrones, and M. S. Dresselhaus, "Defects and impurities in graphene-like materials", Materials Today **15**, 98–109 (2012).

[228] J.-Y. Hwang, C.-C. Kuo, L.-C. Chen, et al., "Correlating defect density with carrier mobility in large-scaled graphene films: raman spectral signatures for the estimation of defect density", Nanotechnology **21**, 465705 (2010).

[229] Y. Ma, J. Ma, Y. Lv, et al., "Effect of mono vacancy defect on the charge carrier mobility of carbon nanotubes: a case study on (10,0) tube from first-principles", Superlattices and Microstructures **99**, 140–147 (2016).

[230] I. V. Borzenets, F. Amet, C. T. Ke, et al., "Ballistic graphene josephson junctions from the short to the long junction regimes", Phys. Rev. Lett. **117**, 237002 (2016).

[231] N. Mizuno, B. Nielsen, and X. Du, "Ballistic-like supercurrent in suspended graphene josephson weak links", Nat Comm. **4**, 2716 (2013).

[232] V. E. Calado, S. Goswami, G. Nanda, et al., "Ballistic josephson junctions in edge-contacted graphene", Nature Nanotechnology **10**, 761–764 (2015).

[233] M. Popinciuc, V. E. Calado, X. L. Liu, et al., "Zero-bias conductance peak and josephson effect in graphene-nbtin junctions", Phys. Rev. B **85**, 205404 (2012).

[234] P. Mondal, A. Nogaret, and S. Ghosh, "Quantum transport through pairs of edge states of opposite chirality at electric and magnetic boundaries", Physical Review B **98**, 125303 (2018).

[235] M. Hatefipour, J. J. Cuozzo, J. Kanter, et al., "Induced superconducting pairing in integer quantum hall edge states", Nano Letters **22**, 6173–6178 (2022).

[236] T. Akiho, H. Irie, Y. Nakazawa, et al., "Andreev reflection in the quantum hall regime at an al/inas junction on a cleaved edge", Nano Letters **24**, 14790–14796 (2024).

[237] T. D. Moore and D. A. Williams, "Andreev reflection at high magnetic fields", Phys. Rev. B **59**, 7308–7311 (1999).

[238] D. Uhlisch, S. G. Lachenmann, T. Schäpers, et al., "Splitting of the subgap resistance peak in superconductor/two-dimensional electron gas contacts at high magnetic fields", Phys. Rev. B **61**, 12463–12466 (2000).

[239] U. Zülicke, H. Hoppe, and G. Schön, "Andreev reflection at superconductor–semiconductor interfaces in high magnetic fields", Physica B: Condensed Matter **298**, 453–456 (2001).

[240] J. Eroms, D. Weiss, J. D. Boeck, et al., "Andreev reflection at high magnetic fields: evidence for electron and hole transport in edge states", Phys. Rev. Lett. **95**, 107001 (2005).

[241] D. Wang, E. J. Telford, A. Benyamini, et al., "Andreev reflections in nbn/graphene junctions under large magnetic fields", Nano Letters **21**, PMID: 34569787, 8229–8235 (2021).

[242] Y. Takagaki, "Magnetotransport in graphene nanoribbons sandwiched by superconductors at side edges", Journal of Physics: Condensed Matter **34**, 305303 (2022).

[243] R. P. Tiwari, U. Zülicke, and C. Bruder, "Majorana fermions from landau quantization in a superconductor and topological-insulator hybrid structure", Phys. Rev. Lett. **110**, 186805 (2013).

[244] J. Barrier, M. Kim, R. K. Kumar, et al., "One-dimensional proximity superconductivity in the quantum hall regime", Nature **628**, 741–745 (2024).

[245] L. Zhao, E. G. Arnault, A. Bondarev, et al., "Interference of chiral andreev edge states", Nature Physics **16**, 862–867 (2020).

[246] F. Amet, C. T. Ke, I. V. Borzenets, et al., "Supercurrent in the quantum hall regime", Science **352**, 966–969 (2016).

[247] G.-H. Lee, K.-F. Huang, D. K. Efetov, et al., "Inducing superconducting correlation in quantum hall edge states", Nature Physics **13**, 693–698 (2017).

[248] R. Huber, M.-N. Steffen, M. Drienovsky, et al., "Band conductivity oscillations in a gate-tunable graphene superlattice", Nature Communications **13**, 2856 (2022).

[249] A. Mreńca-Kolasińska, S.-C. Chen, and M.-H. Liu, "Probing miniband structure and hofstadter butterfly in gated graphene superlattices via magnetotransport", npj 2D Materials and Applications **7**, 64 (2023).

[250] K. P. Nuckolls, M. G. Scheer, D. Wong, et al., "Spectroscopy of the fractal hofstadter energy spectrum", Nature **639**, 60–66 (2025).

[251] J. M. Ferreyra and C. R. Proetto, "Landau levels in the presence of a potential barrier", Journal of Physics: Condensed Matter **6**, 6623 (1994).

[252] Y. Hatsugai, "Chern number and edge states in the integer quantum hall effect", Phys. Rev. Lett. **71**, 3697–3700 (1993).

List of Publications

1. "*Electronic analogue of Fourier optics with massless Dirac fermions scattered by quantum dot lattice*", Partha Sarathi Banerjee, Rahul Marathe and Sankalpa Ghosh, *J. Opt.*, **26**, 095602.

2. "*Magnetically modulated superconductor-graphene-superconductor (SGS) Josephson junctions and their tunability*", Partha Sarathi Banerjee, Rahul Marathe and Sankalpa Ghosh, *Phys. Scr.*, **100**, 015965.

3. "*Intermediate chiral edge states in quantum Hall Josephson junctions*", Partha Sarathi Banerjee, Rahul Marathe and Sankalpa Ghosh, arXiv: 2510.11432.

Partha Sarathi Banerjee

partha.ae1@gmail.com +91 8240634012 Howrah, India
LinkedIn Personal Website GitHub arXiv

Education

2019 – 2026 **Ph.D.** Physics
Indian Institute of Technology Delhi, India
Specialization: Quantum Condensed Matter Physics
Thesis title: *Scattering of massless Dirac fermions in modulated graphene junctions and its effect on electron transport*

2017 – 2019 **M.Sc.** Physics
Indian Institute of Technology Delhi, India
Thesis title: *Parametric resonance in presence of noise and dissipation memory kernel.*
CGPA Obtained: 8.512

2014 – 2017 **B.Sc.** Hons. in Physics
Bangabasi College, University of Calcutta, India

Experience

Jan 2025 – July 2025 Associate (intern) at **Morgan Stanley**
Worked on Tier 1 Risk and Capitals models related to RWA and Prudent Valuation. Performed model diagnostic tests, benchmark tests and sensitivity analysis

Worked on the initial validation of AI/ML based identity verification models.

Skills

Programming Languages: Python 3+ (Numpy, Pandas, SciPy, Matplotlib, Seaborn), FORTRAN, C, R, Julia

Numerical Techniques: Monte Carlo, Discrete Fourier Transform, Linear regression, Polynomial regression, Ridge regression, Lasso regression, Elastic Net, PCA regression.

Tools: Mathematica, MATLAB, MS Excel.

Operating Systems: Linux, Windows

Language: English - proficient, Bengali - Native, Hindi - proficient

Academic Visit

Nov, 2025 - Jan, 2026 **Stort term visiting student:** As a part of SPARC project under the supervision of Prof. Efrat Shimshoni at **Bar-Ilan University**, Ramat Gan, Israel.

Awards and Achievements

2019 Qualified **JEST** and **GATE** for PhD.

2018 Qualified **Joint CSIR-UGC NET(LS).**

Qualified **JEST** for PhD (Rank 125).

2017 **State Topper (West Bengal)** of National Graduate Physics Examination of IAPT.

College Topper in BSc(Hons.) Examination at Bangabasi College, Kolkata, India.

Awards and Achievements (continued)

- Qualified **JEST** for Integrated PhD (Rank 210).
- Qualified **IIT-JAM** for M.Sc (Rank 109).

Project / Internship

July, 2018 - July, 2019 — **MSc Project:** "Studying Parametric Resonance in the presence of Noise and Dissipation Memory Kernel" under the supervision of Dr Rahul Suresh Marathe at **Indian Institute of Technology, Delhi**, India.

May 2018 - July 2018 — **Summer Research Internship:** "Aubry Transition in Colloidal Monolayers" under supervision of Dr. A. V. Anil Kumar at the National Institute of Science Education and Research **(NISER)**, Bhubaneshwar, India

Research Publications

1. P. S. Banerjee, R. Marathe, and S. Ghosh, *Intermediate chiral edge states in quantum hall josephson junctions (submitted)*, 2025. arXiv: 2510.11432. URL: https://arxiv.org/abs/2510.11432.
2. P. S. Banerjee, R. Marathe, and S. Ghosh, "Electronic analogue of fourier optics with massless dirac fermions scattered by quantum dot lattice," *Journal of Optics*, vol. 26, no. 9, p. 095 602, Jul. 2024. DOI: 10.1088/2040-8986/ad645b.
3. P. S. Banerjee, R. Marathe, and S. Ghosh, "Magnetically modulated superconductor-graphene-superconductor (sgs) josephson junctions and their tunability," *Phys. Scr.*, vol. 100, no. 1, p. 015 965, Dec. 2024. DOI: 10.1088/1402-4896/ad9c23.

Teaching Assistantship at IIT Delhi

Courses: Numerical and Computational Methods in Research, Statistical Physics, Quantum Mechanics

Conferences Attended

- **Quantum Materials in the Quantum Information Era** from 25 - 29 September 2023 at the Max Planck Institute for the Physics of Complex Systems (**MPIPKS**), Dresden, Germany.
- **Emergent phenomena in van der Waals heterostructures 2023** from 9-12 Jan 2023 at **TIFR**, Mumbai, India.

References

Prof Rahul Marathe
Associate Professor
Indian Institute of Technology, Delhi
Hauz Khas 110016, Delhi, INDIA.
marather-ahul@physics.iitd.ac.in

Prof Sankalpa Ghosh
Professor
Indian Institute of Technology, Delhi
Hauz Khas 110016, Delhi, INDIA.
sankalpa@physics.iitd.ac.in

Prof Efrat Shimshoni
Chair
Department of Physics
Bar-Ilan University
Ramat Gan, Israel
Efrat.Shimshoni@biu.ac.il